# THERMAL CONTACT RESISTANCE MODELING IN AA7075 HOT STAMPING

# THERMAL CONTACT RESISTANCE MODELING IN AA7075 HOT STAMPING

By

MOHAMAD FARID MOHAMAD SHARIF, B.Eng., M.Eng.

A Thesis

Submitted to the School of Graduate Studies

in Partial Fulfilment of the Requirements for

the Degree Doctor of Philosophy

McMaster University

McMaster University DOCTOR OF PHILOSOPHY (2022) Hamilton, Ontario
(Mechanical Engineering)

| | |
|---|---|
| TITLE: | **Thermal Contact Resistance Modeling in AA7075 Hot Stamping** |
| AUTHOR: | Mohamad Farid Mohamad Sharif |
| | B.Eng. (Toyohashi University of Technology, Japan) |
| | M.Eng. (Toyohashi University of Technology, Japan) |
| SUPERVISOR: | Professor Mukesh K. Jain |
| SUPERVISOR: | Professor Mohamed S. Hamed |
| NUMBER OF PAGES: | xv, 188 |

# Abstract

Hot stamping and die quenching (HS/DQ) process of AA7075 aluminum alloy is one of attractive forming techniques for producing high strength automotive structural components to encounter their poor formability at room temperature. In this technique, quenching rate of this alloy is very crucial as it affects precipitation kinetics after artificial ageing of part formed, which in turn determines the final in-service mechanical properties and corrosion performance of part. Thermal contact resistance (TCR) between two solid surfaces is the main parameter that controls heat transfer between hot AA7075 sheet and cold steel dies, and thus affects quenching rate of part formed. Therefore, the final properties of automotive parts produced by hot stamping is indirectly influenced by TCR.

The common methods of determining TCR in HS/DQ are often impracticable as they require thermocouples to be inserted into complex-shaped stamping dies, punches and thin aluminum sheet (blank) to be formed. A potential mechanistic approach for determining TCR could be an attractive alternative due to its avoidance of embedded thermocouples into the tooling and blank. The mechanistic method emphasizes on physical mechanisms (roughness etc.) governing interfacial heat transfer between cold forming tools and hot blank.

The proposed work focuses on utilizing the mechanistic method to predict TCR between multiple cylindrical asperities on a nominally flat (and heated) AA7075 blank surface and a rigid, flat, asperity-free (and cold) steel die surface. The asperities were considered to deform elastoplastically, increasing contact area. Subsequently, TCR correlation as a function of temperature, contact load, and contact area was formulated. To validate the mechanistic model, a series of surface asperity flattening experiments using thermocouple-embedded AA7075 blank and polished stainless steel planar dies were carried out. Good agreement between mechanistic model predictions and experimental results in term of contact area and TCR as a function of contact load were observed.

# Acknowledgements

Alhamdulillah, I praise and thank Almighty God for giving me the strength, health and courage to complete this thesis.

I would like to express my deepest gratitude and appreciation to my supervisors Professors Mukesh K. Jain and Mohamed S. Hamed for their invaluable expertise, guidance, support and encouragement throughout my studies. Special thanks to my supervisory committee members, Professor Sumanth Shankar and Professor Chan Ching, for their critical comments and suggestions that helped in clarifying some of the concepts in this thesis. I also wish to thank Dr. Matthew Brake of Rice University, USA, for clarifying his recent theoretical spherical asperity flattening work.

My sincere gratitude goes to Ministry of Higher Education Malaysia and Universiti Malaysia Pahang for the financial support during my study and Novelis Aluminum Company to fund this research project.

Thank are also due to staff members of CAMC as well as MMRI for their help and technical support, and especially Dr. Mike Bruhis, who supported me with experimental work. I am also thankful to the technical staff members in the Mechanical Engineering Department, and especially Ron Lodewyks, Michael Lee, John Colenbrander and late Dan Wright who provided valuable help at many points during this study.

I am grateful to Dr. Anantheshwara Kommunje and Dr. Zhutian Xu, who helped me learn to use many of the lab tools and machines properly during my experimental work. Additionally, I would like to thank all of my colleagues at the Metal Forming Lab (MFL) and the Thermal Processing Lab (TPL) for their friendship and support.

Without continuous pray, support, and inspiration of my family, this endeavor would not have possible. Last, but not least, neither appreciation nor gratitude could ever pay back to my wife Zainab, and my daughters Maryam, Yasmin, Zahra and Husna for their love, patience and understanding during the hard times of this work.

# Table of Contents

# List of Figures

# List of Tables

# Nomenclature

| | | | |
|---|---|---|---|
| $A$ | nominal area ($mm^2$) | $Bi$ | Biot number |
| $A_r$ | real contact area ($mm^2$) | $C_p$ | specific heat at constant pressure |
| $a$ | radius of contact area (mm) | $C_v$ | specific heat at constant volume |
| $L$ | length of cylindrical asperity (mm) | $b$ | heat flow channel width, half contact width (mm) |
| $c$ | flux tube radius, constriction width (mm) | $b_e$ | elastic half contact width (mm) |
| $E$ | Young's elastic modulus (MPa) | $b_y$ | half contact width at yield (mm) |
| $E'$ | equivalent elastic modulus (MPa) | $b_{fp}$ | half contact width at fully plastic (mm) |
| $dz$ | indentation depth (mm) | $b_p$ | plastic half contact width (mm) |
| $dz_y$ | indentation depth at yield (mm) | $k_1, k_2$ | thermal conductivity for material 1 and 2 (W/mmK) |
| $dz_{fp}$ | indentation depth at fully plastic (mm) | $k$ | harmonic mean thermal conductivity (W/mK) |
| $q$ | heat flow (W) | $q''$ | heat flux ($W/m^2$) |
| $h$ | total thermal contact conductance ($W/m^2K$) | $R$ | total thermal contact resistance (K/W) |
| $h_{sol}$ | Solid to solid thermal conductance ($W/m^2K$) | $R_c$ | solid to solid contact thermal resistance (K/W) |
| $h_{air}$ | air gaps thermal conductance ($W/m^2K$) | $R_{air}$ | air gaps thermal resistance (K/W) |
| $h_{rad}$ | radiation thermal conductance ($W/m^2K$) | $R_{rad}$ | radiation thermal resistance (K/W) |

| | | | |
|---|---|---|---|
| $H$ | microhardness (MPa) | TS | future time step |
| $T_b$ | blank temperature (ºC) | $T(t)$ | time dependent temperature (ºC) |
| $T_d$ | die temperature (ºC) | $T_0$ | initial temperature (ºC) |
| $V$ | blank volume ($mm^3$) | $Ø$ | sensitivity coefficient ($m^2K/W$) |
| $m_1$, $m_2$ | absolute surface slope for material 1 and 2 | $R_{q1}$, $R_{q2}$ | r.m.s. surface roughness for material 1 and 2 (µm) |
| $m$ | effective mean absolute surface slope | $R_q$ | mean r.m.s. surface roughness (µm) |
| $n_T$ | total number of asperities | α | thermal accommodation coefficient |
| $P$ | applied pressure (MPa) | λ | air mean free path |
| $R_a$ | average surface roughness (µm) | g | temperature jump distance |
| $J$ | number of thermocouple | TS | number of future time step |

# Chapter 1

## Introduction

### 1.1 Hot Stamping and Die Quenching (HS/DQ) of AA7075 Aluminum Alloy

Utilization of aluminum alloys as an alternative material to steel has long been considered due to its attractive characteristics such as lighter weight, corrosion resistance, and recyclability. Recently, there has been much interest from the automotive industry in AA7xxx series for sheet forming applications due to its higher post-formed strength under aged condition compared to aluminum alloys from other series. However, AA7xxx series alloys have poor formability at room temperature. One attractive possibility is to form them by employing hot stamping and die quenching process (HS/DQ) at elevated temperatures followed by artificial ageing to increase the part's strength.

HS/DQ is a process where hot forming and subsequent quenching are combined in a single operation. Through this process, it is feasible to produce complex high strength parts with less spring back. As illustrated in Fig. 1.1, HS/DQ of AA7075 aluminum alloy is envisioned as follows (Harrison & Luckey, 2014); a blank is heated to its solvus temperature of 480°C in a separate furnace, then rapidly transferred to the press (and water-cooled dies) for forming the desired part. (In this thesis, as in sheet forming industry, ‘blank’ is the name given to a cut piece of sheet metal prior to forming and ‘part’ is referred to a formed blank). Forming is followed immediately by rapid quenching of the part while clamped in the die. This rapid quenching is necessary to avoid formation of coarse

precipitates which are detrimental to the subsequent ageing response of the material. The formed part is subsequently artificially aged or overaged to achieve a high strength T6 or T7 temper in the formed part.

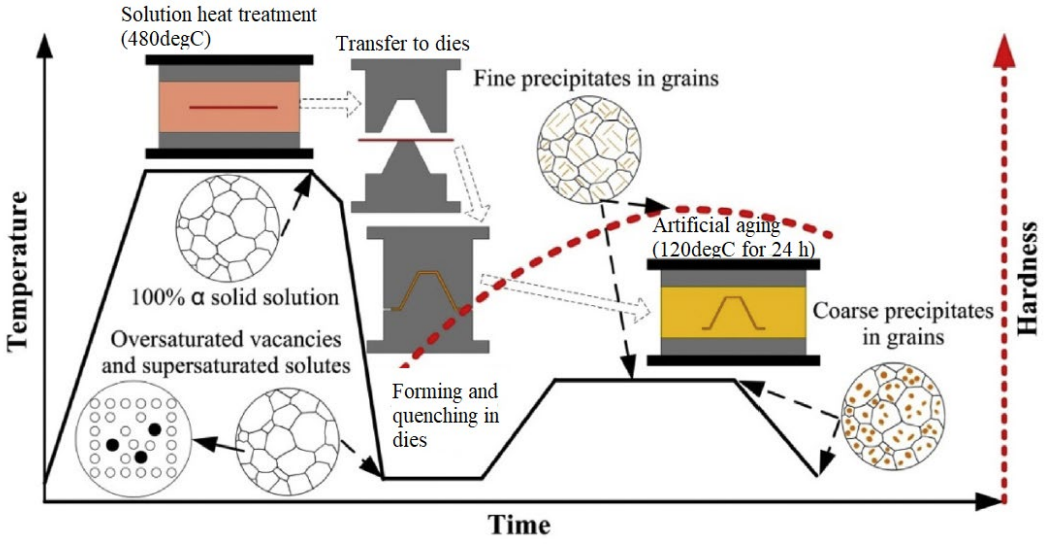


Figure 1. 1 HS/DQ process for aluminum alloy AA7075 (Liu et al., 2020).

One challenging aspect of the HS/DQ process for AA7075 alloy is that the time window for transferring the blank from the furnace to the cold die, and subsequent forming and quenching is considerably short due to the shape of the continuous cooling transformation (CCT) curve for AA7075 (see Fig. 1.2). In other words, the quenching rate must be higher than 100 °C/s to avoid the nose of the CCT curve (Totten & MacKenzie, 2003). Proper quenching of the formed part will preserve the supersaturated solid solution state of the alloy and avoid the formation of non-hardening precipitates, which are deleterious to post-quench artificial ageing strength improvement response of AA7075 alloy part (Keci et al., 2014).

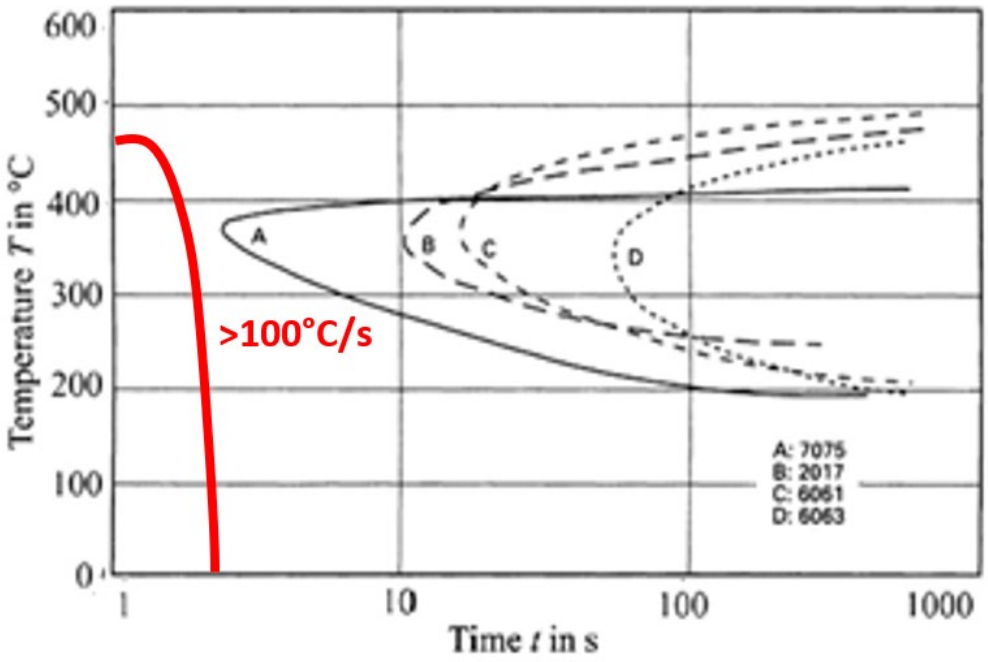


Figure 1. 2 CCT curve for AA7075 blank: experimental result (U.S. Def. Dept., 1991).

Perfect quenching is unlikely unless an ideal die design is developed that incorporates a realistic heat transfer model for simulating and optimizing the hot stamping process. In the heat transfer model development, thermal contact resistance (TCR) is the primary parameter that governs the heat transfer between hot blank and cold dies. It thus determines the quenching rate, and consequently, the local temperature field distribution in the stamped formed part and its precipitation hardening (i.e., strengthening) response after quenching and subsequent ageing. To sum up, the strength of the final formed part is directly influenced by the thermal contact resistance (E. Caron et al., 2013; Hung et al., 2014).

## 1.2 TCR Prediction Methods in HS/DQ

Generally, there are three approaches to determining the TCR in HS/DQ process; heat balance method, finite element (FE) based optimization method, and inverse heat conduction method. The heat balance method is the simplest but highly approximate due to the assumption of constant die temperature. The most used method for hot stamping is FE based optimization method in which TCR is determined by matching the measured blank and die temperatures with FE simulation (Hu et al., 2013; Ji et al., 2016; Liu et al., 2017; Omer et al., 2020; Tondini et al., 2011; Wang et al., 2016; Zhang et al., 2015). However, this method only predicts a single constant TCR value, an unreasonable result considering the transient nature of hot stamping.

The inverse heat conduction method is the most reliable method for hot stamping due to its simple implementation (Abdulhay et al., 2011; Caron et al., 2013; Lu et al., 2017; Malkin & Guo, 2007; Wang et al., 2016; Ying et al., 2017; Zhao et al., 2015). In this category, the Beck's sequential function specification scheme (Beck et al., 1985) is considered one of the most efficient inverse heat conduction methods to predict the TCR between hot blank and cold die. This method determines the TCR using inverse heat conduction calculation from temperature measurements inside the die and the blank.

However, this method has some severe limitations as it requires thermocouples to be inserted in complex-shaped stamping dies, punches, and even in the thin blank. There are regions where stretching and bending occur, especially in the curved areas (Fig. 1.3(a, b)). It is challenging to embed thermocouples inside such curved areas and within the thin deforming blank typically less than 2 mm in thickness. The damage to the thermocouple is

often inevitable during the test. Therefore, it is crucial to find other alternative approaches to predict the TCR in HS/DQ.

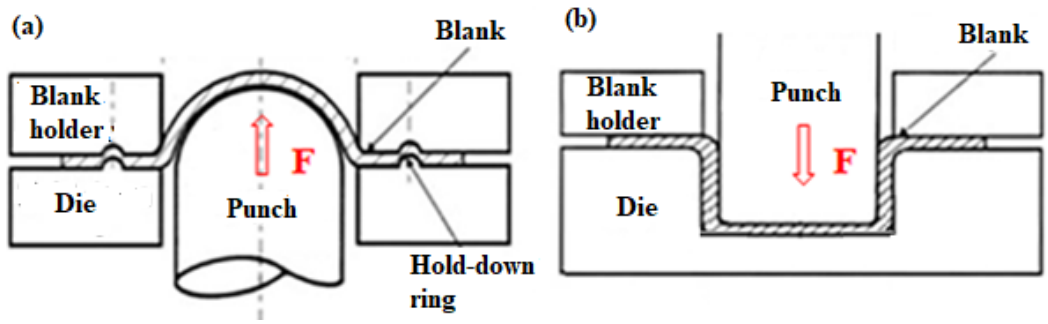


Figure 1. 3 Two common blank forming processes and associated die configurations: (a) hemispherical dome stretching and (b) U-shaped channel forming (Bruschi et al., 2014).

A mechanistic method, already available in the literature, avoids embedded thermocouples, and appears to be feasible for TCR prediction during the HS/DQ process. However, the mechanistic method has not been thoroughly investigated for determining TCR in the complex hot stamping of sheet materials. In contrast to the inverse heat conduction method, the mechanistic method focuses on physical mechanisms governing thermal contact resistance of two contacting, and typically loaded solid surfaces at different temperatures. It considers waviness (macroscopic) and roughness (microscopic) and temperature-dependent strength and ductility of the above irregularities at the interface between two bodies in contact and under large contact pressures. This study will explore the physical and mechanical characteristics of both contacting and normally loaded surfaces and develop several new mechanistic models to predict TCR in hot stamping of AA7075 sheet.

## 1.3 Research Objectives

This research focuses on utilizing the mechanistic method to predict TCR between hot AA7075 aluminum blank and cold stainless steel dies. In order to achieve this objective, three specific sub-objectives are proposed as follows:

i. Development of geometrical analysis and mechanics of asperity flattening by considering a contact between a multi-asperity cylinder surface segment on a nominally flat (and heated) AA7075 aluminum sheet surface undergoing elastoplastic deformation, and a normally loaded contact with rigid, asperity-free, flat (and cold) stainless steel surface representing the die (or punch) surface. Towards this objective, a model of single cylinder-flat (SCF) surface contact which considers elastic and strain hardening plastic effect at elevated temperature is formulated. Based on variants of this model, a multi cylinders-flat (MCF) surface contact model representing a wavy and rough aluminium AA7075 blank and a smooth stainless steel die contact is also developed.

ii. Determination of thermal contact resistance (TCR) from the above SCF and MCF surface contact models and other existing model in the literature. The TCR model represents TCR as a function of temperature and normal contact load.

iii. Comparison of performance of several mechanistic models with well-controlled hot pressing experiments on AA7075 aluminum blank with a cold planar stainless steel die at several different temperatures and normal loading conditions. To validate these models, a series of pressing experiments at

elevated temperatures need to be conducted under conditions representative of hot stamping of AA7075. Thermocouples need to be inserted in the AA7075 blank and stainless steel die to record the temperatures and enable the commonly used Beck's method to calculate the TCR. Different contact forces need to be applied to the hot AA7075 blank which located between the cold stainless steel dies. Asperity flattening characteristics under the above test conditions such as contact area at different indentation depths need to be measured. The experimental results should be compared with the experimental results.

## 1.4 Thesis Outline

This thesis consists of six chapters, including the current one. In Chapter 2, a more detailed review of the literature related to the above methods of TCR prediction is presented. In addition, several existing contact mechanics models which are relevant to the above objectives are also reviewed. The experimental methodologies associated with elevated temperature asperity flattening under planar contact and normal loading conditions are described in Chapter 3. Chapter 4 presents the specific formulations of SCF and MCF models developed to accomplish the objectives. The results from several mechanistic models and experiments are presented, compared, and discussed in Chapter 5. Chapter 6 concludes the research finding about suitability of various mechanistic models as well as offers recommendations for future study.

# Chapter 2

## Literature Review

---

This chapter presents a review of literature related to TCR prediction in one-dimensional solid-to-solid conduction heat transfer conditions existing during hot stamping/die quenching (HS/DQ) sheet metal forming process used in the automotive industry. TCR prediction models based on traditional 1-D heat transfer methods using embedded thermocouples in the two solid bodies in nominal physical contact as well as those based on surface asperity contact analysis are reviewed. The latter models are relatively recent especially for determining TCR under HS/DQ conditions. These latter models are the primary focus of the present research due to their intrinsic advantages over the traditional heat transfer methods for HS/DQ applications.

### 2.1 TCR/IHTC determination Methods for HS/DQ Process

The TCR can be defined as a thermal resistance to heat flow at the blank and die interface. In other words, it demonstrates the level of heat transfer across solid to solid interfaces. Generally, the TCR parameter can be expressed as:

$$R = \frac{T_b - T_d}{q} \tag{2.1a}$$

where $T_b$, $T_d$ and $q$ are the temperatures of blank and die surfaces, and the total heat flow across the interfacial contact respectively. This parameter can also be represented by TCR times nominal area (later be simplified as 'TCR area' or '*RA*') which is defined as:

$$RA = \frac{(T_b - T_d)}{q"} \tag{2.1b}$$

where $q"$ is the heat flux across the interfacial contact. The reciprocal of TCR area is referred to as interfacial heat transfer coefficient (IHTC) in the literature, which is a thermal conductance at a contact interface. It is defined as:

$$h = \frac{q"}{(T_b - T_d)} \tag{2.2}$$

The units for TCR and IHTC are K/W and W/m$^2$K respectively. However, it should be noted that TCR area and IHTC will be used interchangeably throughout this chapter since both of these quantities are extensively utilized in the literature.

### 2.1.1 Conventional Heat Transfer Methods

HS/DQ process involves taking a hot and nominally flat ductile sheet material and rapidly forming (or shaping) it into a useful 3D automotive component using a high-speed automotive press and cold steel tools and dies. During the forming process, the sheet permanently deforms largely plastically under transient heat transfer conditions in the contact region of the sheet and die. Accurate TCR area (or IHTC) determination at the contact surface is critical to the development and optimization of the HS/DQ process using the well-known finite element (FE) simulation of HS/DQ processes. Although TCR prediction methods have been extensively studied in the literature in the past six decades, their adaptation to HS/DQ process conditions is only about a decade or so old. Research is

still ongoing due to the fact that the TCR area predictions under HS/DQ process conditions are more difficult and results often vary between the different methods and the specific thermophysical and thermomechanical characteristics and properties of the two solids in contact.

It is often not possible and quite complex to locate multiple thermocouples at or near the surfaces of the thin formable blank and the large bulky automotive steel dies of complex 3-D geometry. Also, there are high temperature and large contacting pressures at the interface as well as changing shape of the blank that can cause damage to the thermocouple embedded in the sheet even after a single stamping operation. Three conventional approaches to determine TCR area (or IHTC) in HS/DQ process have been developed. These are heat balance, finite element (FE) based optimization, and inverse heat conduction methods.

#### 2.1.1.1 Heat Balance Method

The heat balance method is based on Newton's law of cooling with the assumptions of constant die temperature. Merklein et al. (2009) carried out heat transfer experiments utilizing a 1.75-mm-thick 22MnB5 Boron steel blank and heatable flat dies (see Figure 2.1(a)). Prior to the clamping, loading and quenching experiments, the blank was heated to the austenization temperature of 950 ºC. The dies temperature was adjusted and maintained at different temperatures (20 ºC, 100 ºC and 300 ºC) using embedded heating cartridges. Additionally, the above researchers conducted 1-D heat conduction experiments with different normal contact pressures from 0 to 30 MPa to obtain IHTC values and other heat

transfer characteristics while assuming the blank as a lumped body (no internal temperature gradient).

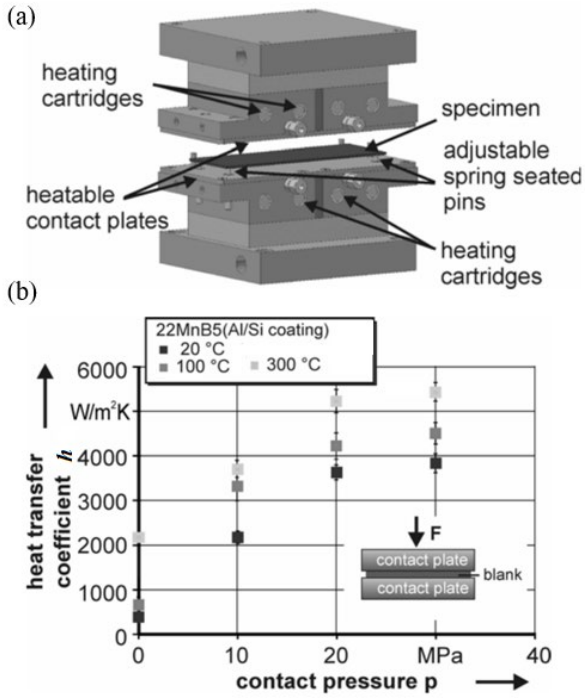


Figure 2. 1 (a) Planar die quenching experimental setup, (b) IHTC as a function of pressure for different die temperatures after clamping for 5 min (Merklein et al., 2009).

The following well-known equation has been used by Merklein et al. (2009) and other researchers (Geiger et al., 2008; Hung et al., 2014; Omer et al., 2020) to analyze the blank cooling process:

$$T_b(t) = (T_0 - T_d)exp\left(-\frac{hA}{mc_p}t\right) + T_d \tag{2.3}$$

where $T_b(t)$, $T_0$, $T_d$, $h$, $A$, $m$, $c_p$ and $t$ refer to measured blank temperature, initial temperature of blank, die temperature, IHTC, nominal contact surface area, mass of blank,

specific heat at constant pressure of blank, and time respectively. It is clear from Eq. (2.3) that in order to predict IHTC at a specific time, one must assume that die temperature remains constant throughout the experiment. The results of Merklein et al. (2009) showed that IHTC between the blank and the die increases non-linearly with the increment of die temperature and the contact pressure (see Figure 2.1(b)).

Omer et al. (2020) also experimentally obtained IHTC values for different materials: a high strength steel alloy, seven different aluminum alloys and two magnesium alloys with contact pressure ranging from 2 to 80 MPa. The results showed remarkable variation IHTC but inclined to correlate predominantly with contact pressure and blank material strength (see Figure 2.2 and Table 1). Material with the highest strength, i.e., Usibor 1500 steel corresponds to the highest IHTC at low pressure. On the other hand, low-

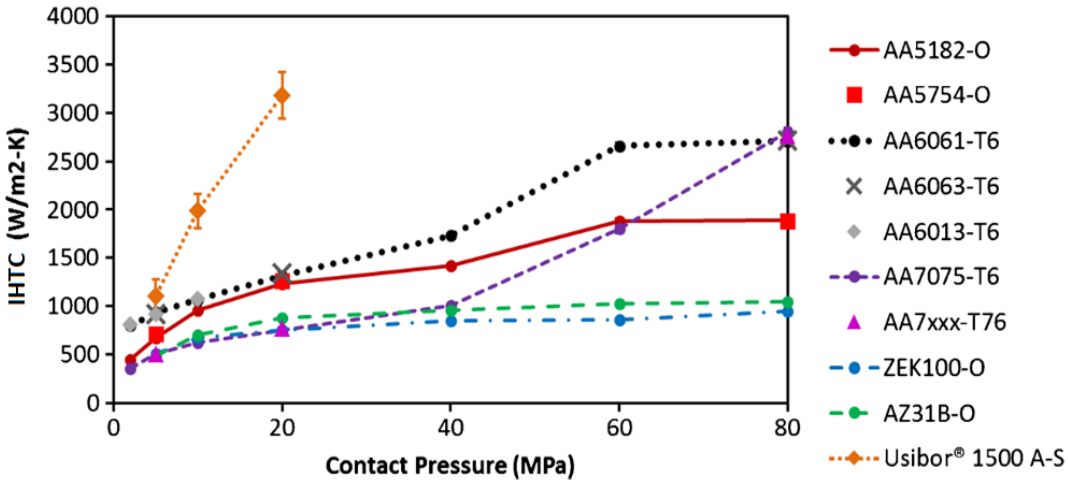


Figure 2. 2 IHTC as a function of pressure for different blank materials (Omer et al., 2020).

Table 2. 1 Yield and ultimate strength of materials shown in Figure 2.2 (MatWeb).

| Material | Yield Strength [MPa] | Ultimate Tensile Strength [MPa] |
|---|---|---|
| AA5182-O | 130 | 275 |
| AA5754-O | 90 | 210 |
| AA6061-T6 | 276 | 310 |
| AA6063-T6 | 214 | 241 |
| AA6013-T6 | 315 | 360 |
| AA7075-T6 | 503 | 572 |
| ZEK100-O | 211 | 254 |
| AZ31B-O | 150 | 255 |
| Usibor 1500 | 450 | 600 |

strength materials such as ZEK100 and AZ31 magnesium alloy sheets have a slight increment on IHTC with pressure. The major weakness of this method is the assumption of constant die temperature, $T_d$ in Equation (2.3). The die temperature is supposed to increase due to heat transfer from the hot blank. In heat transfer theory, this equation is known as 'lumped capacitance method' and actually developed for a contact between small hot and a large cold material bodies. After the contact, the temperature of hot material decreases instantly and the time required for it to reach specific temperature could be determined. Throughout the process, IHTC is kept constant. This method is not suitable in the hot stamping process scenario where IHTC changes over time. The method offers only a highly approximate IHTC value and would fail to predict the cooling rates in different regions of the formed part during the forming process.

#### 2.1.1.2 FEM-based Optimization Method

The second approach using the finite element method (FEM) for IHTC prediction involves thermo-mechanical modeling of the experimental set-up and temperature field with the solid bodies in contact. This temperature field data is then compared with the experimental discrete temperature field data from thermocouples embedded in the blank and die. The input IHTC data in the FE model is then varied and iterated upon until the two temperature fields, model predicted and thermocouple measurements, are within some tolerance limit. The corresponding IHTC is then taken as the prevailing IHTC value in the HS/DQ process. This method has been used by many researchers such as Tondini et al. (2011), Hu et al. (2013), and Liu et al. (2017) due to its simplicity.

Liu et al. (2017) developed a custom experimental laboratory-scale apparatus as shown in Fig. 2.3(a) utilizing a 2 mm thick AA7075 aluminum blank and steel as two solid bodies at different temperatures in contact. The blank was screwed onto the blank holders before being heated by direct resistance heating from top and bottom holders. One major advantage of the method is that there is negligible heat loss from blank transfer from furnace to die. As mentioned earlier, the experimental temperature field data was matched with FE simulation data using PAM-STAMP general purpose software to back calculate the IHTC. The results of this experiment and the model prediction for two different die steels are shown in Fig. 2.3(b) where the IHTC is shown to increase with contact pressure and achieve saturation at a contact pressure of about 10 MPa. It was concluded that the saturation in IHTC value is related to the evolution of real contact area towards the nominal contact area. Ironically, they did not measure real contact area in their experiments. They

also suggested that the different IHTC values between H13 and cast iron steels is due to different thermal conductivities of the two materials (H13 steel with 24.4 W/K and cast iron with 44 W/mK) instead of heat capacity which is almost same for the two materials

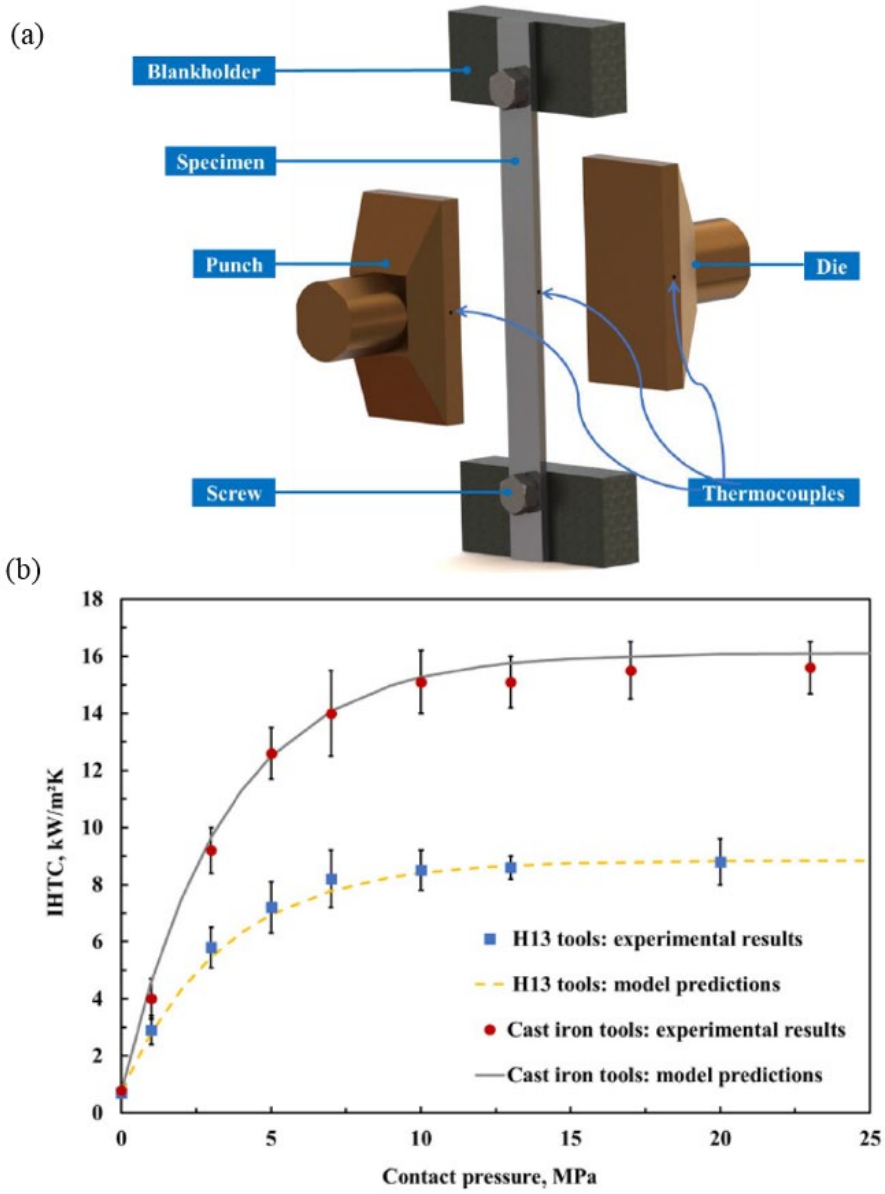


Figure 2. 3 (a) Experimental IHTC determination test jig, and (b) IHTC prediction from PAM-STAMP FE program for two different blank materials (Liu et al., 2017).

(H13 steel with 460 J/kgK and cast iron with 465 J/kgK). Note that the solid and dashed curves in Fig. 2.3(b) are model predictions based on iterations during FE modeling of a hemispherical dome and B pillar components. The sets of values are reasonably close to one another.

The FE based approach to IHTC prediction is essentially a curve fitting procedure that assumes that all other elements of the FE model such as constitutive material behavior, element type and number of elements, friction coefficient at the interface, and chosen thermophysical properties of contacting solids in the model are indeed correct and the only variable affecting the temperature field is the IHTC value. Additionally, as demonstrated by Wendelstorf et al. (2008), the FE approach only provides a single equivalent IHTC value at a given contact pressure, which does not reflect the transient nature of IHTC during the HS/DQ process.

#### 2.1.1.3 Inverse Heat Conduction Method

The last traditional approach to predicting the TCR area is the inverse heat conduction method where Beck's sequential method (Beck et al., 1985), perhaps the most commonly used method for TCR area prediction, is used in hot stamping application (see, for example, Abdulhay et al., 2011, and Figure 2.4).

This method inversely solves the heat flux and temperature at the interface from measured temperature fields within the die. The optimal TCR area values are obtained by first minimizing the difference between the calculated and measured die temperatures during the whole quenching time to predict the heat flux at the die surface, $q"$.

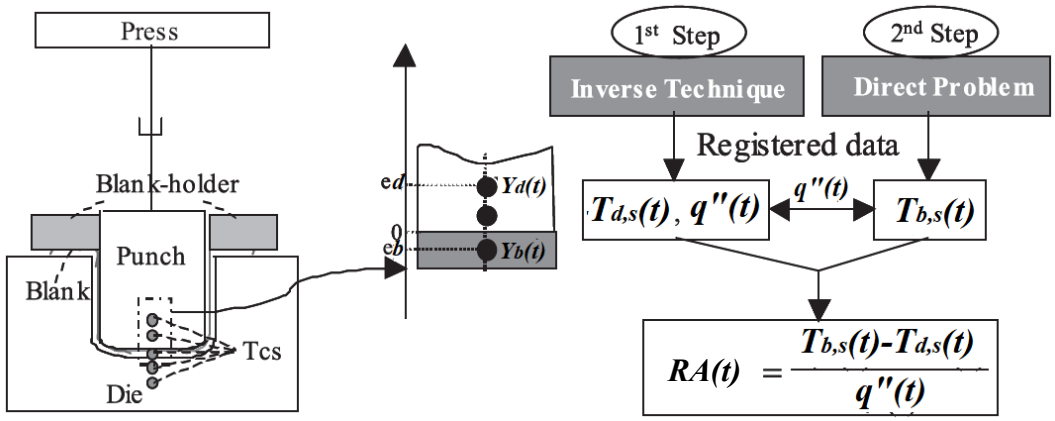


Figure 2. 4 Principle of Beck's method (Abdulhay et al., 2011).

This quantity at a time *t* is expressed as:

$$q"(t) = \frac{\sum_{i=1}^{TS}\sum_{j=1}^{J}\left(Y_{d,j}(t+i-1)-T_{d,j}(t+i-1)|q"(t)=\cdots 0\right)\phi_{ji}}{\sum_{i=1}^{TS}\sum_{j=1}^{J}{\phi_{ji}}^{2}} \tag{2.4}$$

where *J*, *TS*, $Y_d$ and $T_d$ are number of thermocouples in the die, number of future time steps, measured and calculated die temperatures, respectively. The sensitivity coefficient $\phi_{ji}$ is defined as,

$$\phi_{ji} = \frac{\partial T_{ji}}{\partial {q"}_{ji}} \tag{2.5}$$

Knowing the interfacial heat flux $q"(t)$, the die surface temperature ($T_{d,s}(t)$) can also be predicted as follow:

$$T_{d,s}(t) = T_{d,s}(0) + \sum_{l=1}^{t} {q"}_{l}\Delta\phi_{t-l} \tag{2.6}$$

where $T_{d,s}(0)$ is the initial temperature of die surface. Subsequently, using the same interfacial heat flux $q"(t)$ and measured blank temperature $Y_b(t)$, the blank surface temperature ($T_{b,s}(t)$) can be calculated by using direct 1-D heat conduction solver. Finally, TCR area can be determined from the reciprocal of Eq. 2.2b earlier.

Abdulhay et al. (2011) developed an experimental test rig with embedded thermocouples in tool steel die and punch and 1.55 mm thick Boron steel blank to analyze TCR area using the Beck's method. Four thermocouples were located in the middle of blank, and 18 themocouples were fixed at six points in the die and three points in the punch close to the surface. This was designed with such complexity to observe the TCR area evolution at different locations during hot stamping process (see Figure 2.5(a)). The corresponding temperature-load-time curve during experiment can be seen in Fig. 2.5(b). Thermocouples 1-2 data seem to follow each other during transfer and approach due to the direct contact with die while thermocouples 3-4, cooled by convection and radiation, seem to diverge considerably.

It was found that TCR area value between bottom of the punch and the 22MnB5 steel blank was the lowest while the highest was at the side wall (Fig. 2.6). Further, they had examined the TCR area at the sliding contact at the curvature of the die and found the minimum TCR area was at 45º location. These findings showed that pressure distribution through blank/die contact was not uniform.

Abdulhay et al., (2011) also conducted a numerical analysis by using two general purposes finite element analysis (FEA) software packages, Pam-Stamp 2G and ABAQUS,

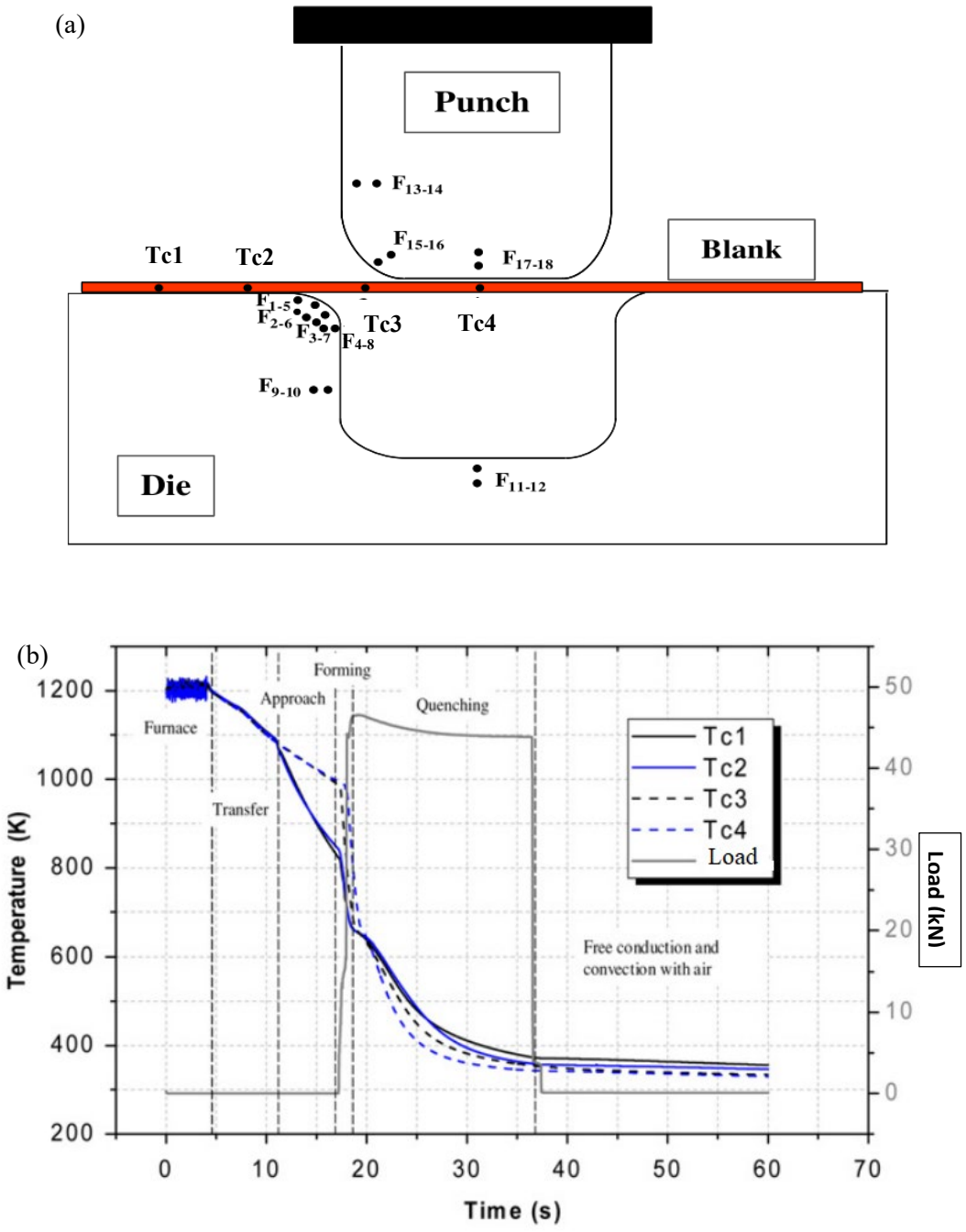


Figure 2. 5 Experimental setup for TCR area determination: (a) stamping tooling geometry with thermocouples placement in the blank and die, (b) typical measured blank temperature during hot stamping experiment (Abdulhay et al., 2011).

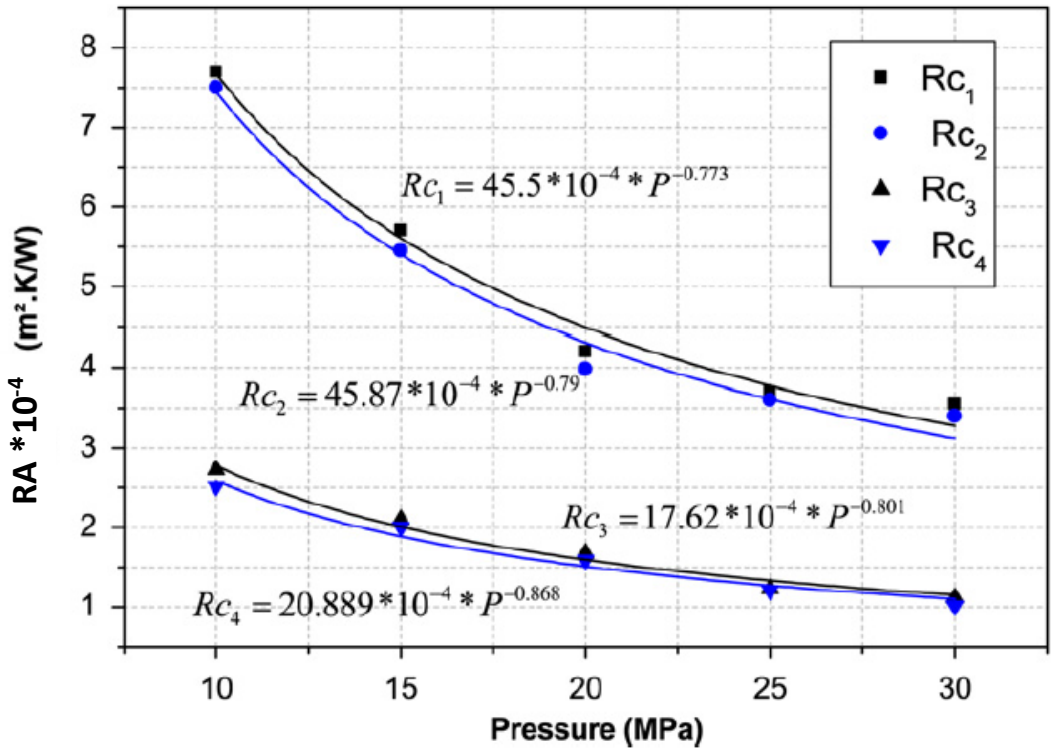


Figure 2. 6 TCR area values as a function of pressure at each of the four thermocouple locations in 2.5(a) (Abdulhay et al., 2011).

to simulate the lab-based experiments using a die to produce a U-shaped hot stamped part.

The work was subsequently continued in another paper by Blaise et al. (2013) that included some of the work of previous authors, where TCR area was estimated during austenite to martensite phase transformation of steel blank using Comsol thermal analysis software. Good agreement between experimental and simulation results was reported.

Another investigation using Beck's method was carried out by Zhao et al. (2015) where IHTC predictions were compared with those from heat balance method for a hot circular steel blank clamped between two disk-shaped steel dies. In addition, FE simulation

of the experiment was performed by varying the IHTC values to obtain a match between the experimental and FE predicted blank temperature-time history. They found that Beck's method provides a more accurate prediction of IHTC compared to the heat balance method, and especially when phase transformation from austenite phase to martensite phase in steel occurs at some intermediate temperature. Temperature-time history of the blank cooling process, however, could not be satisfactorily predicted since the FE model utilized an equivalent IHTC value throughout the clamping process.

Table 2.2 shows a summary of TCR area predictions using the above traditional methods and experimental data in the context of HS/DQ process in the last decade. In general, TCR area values range from 66 to 10000 $mm^2K/W$. These values are not unique as they depend on the contacting materials and the TCR area prediction method. The highest value such as 10000 $mm^2K/W$ corresponds to a lower contact pressure (or perhaps without any pressure) and is not quite relevant for analysis. The variation of TCR area also has a correlation with thermal diffusivity ($\kappa$) of die material. For example, thermal diffusivity of steels; H13, AISI 4140, SS316, and AISI 1045 are 6.86, 11.4, 4.14, and 13.3 $mm^2/s$, respectively. It is to be noted that AA7075 aluminum blank with a thermal diffusivity of 55.4 $mm^2/s$ diffuses heat much faster than boron steel blank with a thermal diffusivity 5.95 $mm^2/s$. Comparison of TCR area between heat balance, FE based optimization and Beck's methods are presented in Fig. 2.7. It can be seen that heat balance method tends to overpredicts TCR area at very low pressures compared to the other two methods.

Table 2. 2 Range of TCR area predictions from various HS/DQ studies.

| Reference | Blank Material | Die Material | Clamping Pressure [MPa] | TCR Area Pred. Method | TCR Area Range [$mm^2K/W$] |
|---|---|---|---|---|---|
| Geiger et al. (2008) | 22MnB5 steel | NA | 10, 20, 30, 40 | Heat balance | 292-787 |
| Merklein et al. (2009) | 22MnB5 steel | NA | 0, 10, 20, 30 | Heat balance | 256-2500 |
| Tondini et al. (2011) | 22MnB5 steel | AISI H11 steel | 5, 10, 20, 30, 40 | FE | 248-315 |
| Abdulhay et al. (2011) | 22MnB5 steel | Z160 steel | 10, 15, 20, 25, 30 | Beck | 109-283 |
| Hu et al. (2013) | 22MnB5 steel | AISI H11 steel | 8, 16, 25, 34, 42 | FE | 190-400 |
| Caron et al. (2014) | 22MnB5 steel | AISI4140 steel | 4, 8, 16, 24 | Beck | 132-227 |
| Hung et al. (2014) | 22MnB5 steel | SKD61 steel | 0, 10, 20, 30 | Heat balance | 264-567 |
| Zhang et al. (2015) | 22MnB5 steel | AISI H13 steel | 2, 6, 10, 15, 18 | FE | 667-3333 |
| Ji et al. (2016) | AA7075 aluminum | mild steel | 0, 10, 20, 30, 40, 50 | FE | 81-10000 |
| Chang et al. (2016) | 22MnB5 steel | AISI1045 steel | 0.006, 0.04, 1, 5, 15, 25 | Beck | 122-3333 |
| Wang et al. (2016) | 22MnB5 steel | AISI H13 steel | 5, 10, 20, 30, 40 | FE | 182-769 |
| Ying et al. (2017) | AA7075 aluminum | AISI H13 steel | 10, 20, 30, 40, 50, 60, 80, 100, 133 | Beck | 194-313 |
| Liu et al. (2017) | AA7075 aluminum | cast iron | 0, 1, 3, 5, 7, 10, 13, 17, 23 | FE | 66-1250 |
| Liu et al. (2017) | AA7075 aluminum | AISI H13 steel | 0, 1, 3, 5, 7, 10, 13, 20 | FE | 116-1429 |
| Omer et al. (2020) | AA7075 aluminum | AISI4140 steel | 2, 5, 10, 20, 40, 60, 80 | Heat balance | 356-2817 |

NA: Not Available

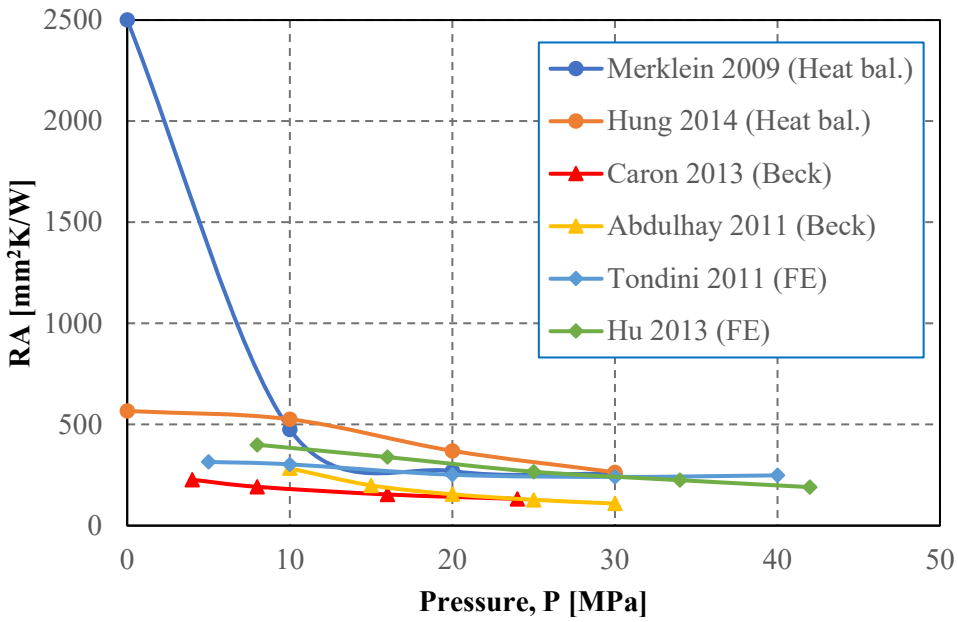


Figure 2. 7 Comparison of TCR area predicted by three different methods.

It is found that most researchers preferred FEM-based optimization method which provides an average IHTC value. Based on the previous review, Beck's method seems to be the most reliable and common among researchers involved in studies related to HS/DQ process. However, one issue with Beck's method, as noted earlier, is the difficulty to embed thermocouples inside the die and the blank for a more complex die design. Thus, a more practical approach needs to be developed. One such approach is a mechanistic method, which does not require complex thermocouple-based measurements for TCR area determination in the HS/DQ process and thus appears quite appealing from a practical perspective. Also, it takes into account geometrical aspects of asperity which are invariably present on a rolled sheet surface such as asperity deformation of the blank as well as changes to the real contact area as discussed below.

## 2.2 Mechanistic Methods

In contrast to the inverse heat conduction method, the mechanistic method considers the evolving geometric surface features of surfaces in contact and subjected to normal load or pressure. Most industrially produced metallic surfaces have quantifiable characteristic features arising from diverse manufacturing processes such as metal rolling, machining, grinding etc. When load is transmitted across the two such surfaces, the initial contact occurs locally at the tip of the surface asperities that lie on the two surfaces. Mechanistic models consider the nature of waviness (macroscopic) and roughness (microscopic) and temperature-dependent strength and ductility of the above irregularities at the interface between two bodies in contact and under large normal contact pressures. As shown by a schematic in Figure 2.8, contact between two solids with rough surfaces mainly consists of air gaps and solid-to-solid contact areas at the tip of of the asperities.

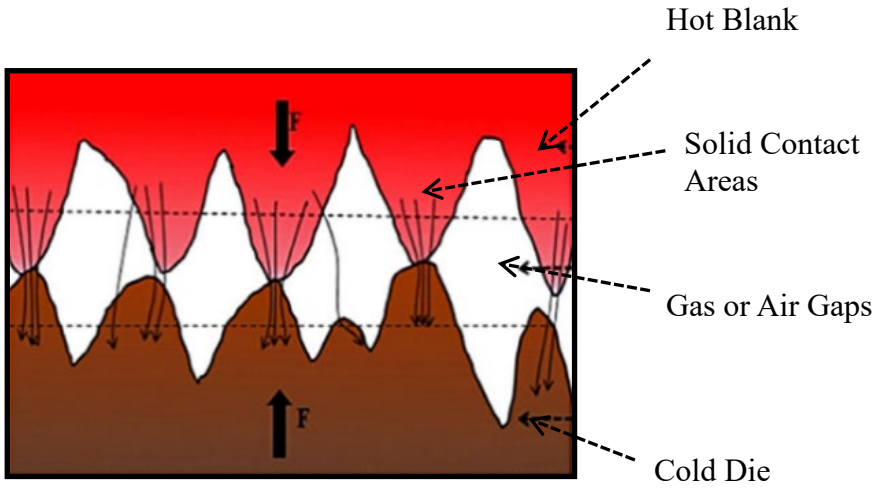


Figure 2. 8 Heat transfer between two solid surfaces in contact (Ying et al., 2017).

The interfacial heat transfer across two contacting rough surfaces at different temperatures is primarily governed by three mechanisms as explained in Madhusudana (2014). These are; (1) conduction heat transfer through the solid-to-solid contact areas, (2) conduction heat transfer through the air gaps between the contacting solid areas, and (3) radiation heat transfer through the air gaps.

In the mechanistic approach, the total TCR (or *R* value) is calculated by accounting for all three thermal resistances through solid-to-solid contact resistance ($R_c$), air gaps thermal resistance ($R_{air}$), and radiation thermal resistance ($R_r$) as follows (Fletcher & Gyorog, 1971):

$$R = \left(\frac{1}{R_c} + \frac{1}{R_{air}} + \frac{1}{R_r}\right)^{-1} \tag{2.7}$$

As presented towards the end of this sub-section, the $R_c$ value is significantly lower than $R_{air}$ and $R_r$ values thus, solid-to-solid heat conduction from blank to die in HS/DQ process occurs predominantly from the lowest $R_c$ value.

### 2.2.1 Geometry, Mechanics and Thermal Interface Relationships

In Eq. (2.7) above, the calculation of $R_c$ requires careful and detailed consideration of asperity geometry, temperature-dependent elastic and plastic contact mechanics at the asperity level, and thermal interface characteristics of solid-to-solid contact. However, before proceeding further, it is perhaps useful to understand from a mechanistic perspective the inter-relationships between variables from the three areas that affect the value of TCR.

According to Yovanovich (2005), the TCR determinants can be divided into geometry, mechanics and thermal interface, as shown in Figure 2.9(a). The combination of geometry and mechanics generates the contact mechanics problem. The combination of geometry and thermal interface creates the constriction (or spreading) resistance problem, and the combination of mechanics and thermal creates the thermo-elastoplasticity problem. Finally, the combination of geometry, mechanics, and thermal interface determines the TCR value obtained from the mechanistic analysis.

The contact mechanics component can be described as a phenomenon of asperities deformation when two solid surfaces are in contact and subjected to normal and/or shear forces across and/or along the contacting surface (the so-called pressed contact condition). This component can be classified into three types: elastic, plastic, and elastoplastic contacts. Asperity shape, size, distribution, and large wavelength curvature of the two contacting surfaces constitute the geometrical component of the problem. Figure 2.9(b), also taken from Yavanovich (2005), shows three common types of geometrical contacts that can be formed under axial compressive loading of the two surfaces in the sheet stamping process.

The contact surfaces can be smooth and non-conforming (Fig. 2.9(b)(i)), rough and non-conforming (Fig. 2.9(b)(ii)), and rough and conforming (Fig. 2.9(b)(iii)). Considering the surfaces that are rough and conforming in sheet stamping process (Fig. 2.9(b)(iii)), micro-gaps exist between the two surfaces that are occupied with air and/or lubricating oil or grease to reduce friction during stamping. A micro-gap resistance model is required in this case for the calculation of TCR. Also, radiation resistance model has to be considered

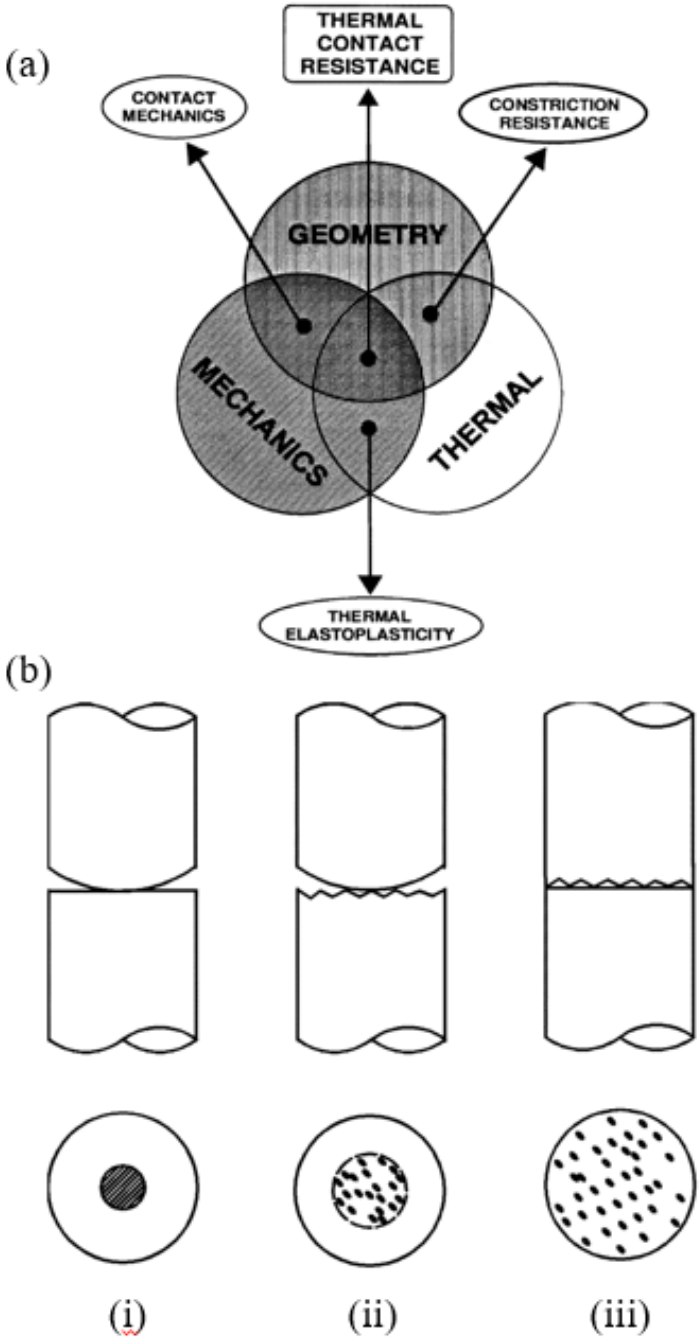


Figure 2. 9 (a) Major components of the TCR problem as per the mechanistic method and (b) schematic illustrations of three general types of geometrical contacts between two solids (M. M. Yovanovich, 2005).

since high temperatures are involved in hot stamping process and radiation through the gaseous medium (i.e., ambient air) is expected.

Finally, the heat transfer and temperature changes across the contact surface are also present, leading to thermal stresses and thermal expansions, thus further affecting the surface characteristics and the stress field. However, these influences are considered minor and have been disregarded in this study.

### 2.2.2 Geometrical Analysis: Surface Topography of Rolled Sheet Metal

An important fundamental basis of the mechanistic models for TCR determination is the evolving nature of contact between two curved surfaces under normal load. As Hertz (1881) originally postulated for elastic contact, the contact patch area is a complex function of the local geometry of contact, material properties of the contacting materials, and the applied normal force. When deformation of many different sized asperities are included in the Hertzian type analysis as initially carried out by Greenwood & Williamson (1966), the real contact area continuously increases with application of load until it approaches the nominal area of contact. This real contact area effectively determines the terminal TCR value in the mechanistic methods.

In contrast, the conventional TCR models are based on a constant nominal contact area, and do not account for the presence of microscopic asperities on nominally flat or nominally curved contact surfaces. The temperature manifests in the mechanistic methods indirectly by affecting the largely plastic deformation of the asperity and consequently the real contact area. For instance, increasing the temperature of the formable sheet increases

the plasticity contribution from the asperity flattening process, resulting in an increase in real contact area and a decrease in the TCR value.

In the following, real surface topography of a rolled sheet metal surface is analyzed first to see how the initial shape of surface asperity will determine the real contact area. Fig. 2.10 presents the rolling lines in the form of peak and valleys along the rolling direction (RD) on the surface of nominally flat AA5182 aluminum sheet. This 'peak-and-valley' topography is imparted from large ground steel rolls during the rolling process. This surface topography manifests itself in the direction transverse to rolling (TD) but remains constant mainly along the rolling direction.

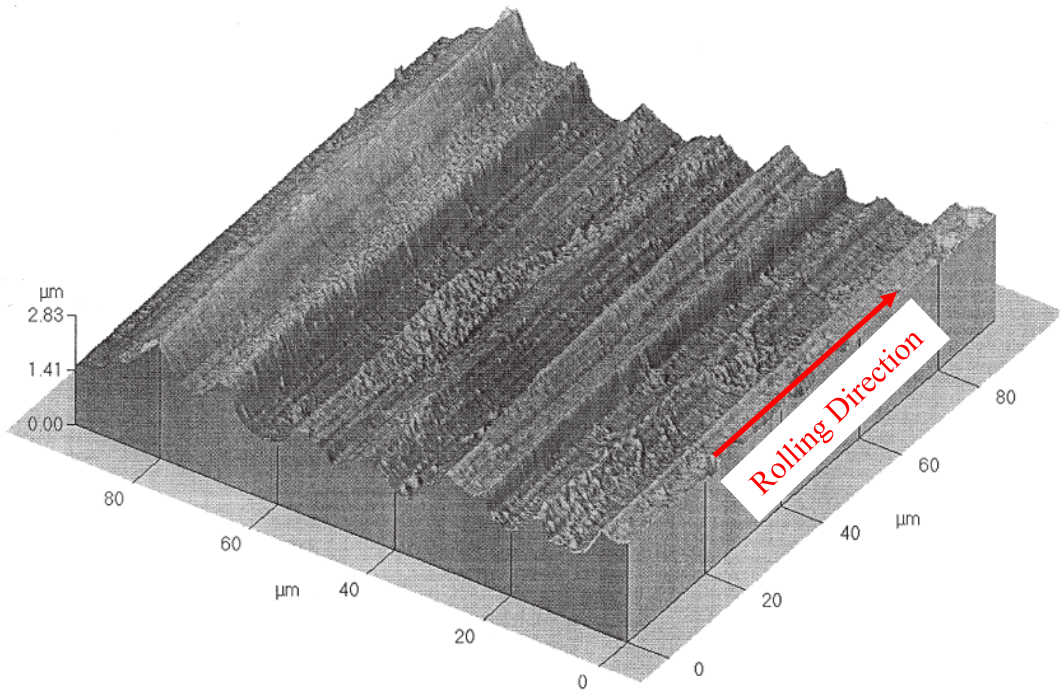


Figure 2. 10 AFM image of aluminum AA5182 sheet surface for 100 x 100 µm$^2$ area. Note that the dimension perpendicular to surface of the sheet are only in the range 0 µm – 2.83 µm (Plouraboué & Boehm, 1999).

Root mean square (RMS) roughness in TD is five times greater than in the RD (Plouraboué & Boehm (1999)). Interestingly, transverse roughness reveals different peaks and valleys that result from plastic deformation during the rolling process. The asperity peaks in the TD direction appear like segments of cylinders of various radii.

### 2.2.3 Analysis of Mechanics of Asperity Deformation: Single-Asperity Contact Model

#### 2.2.3.1 Elastic Regime

When a small load is applied across two contacting rough surfaces, the initial contact area comes from a cluster of single asperity contacts. Therefore, it is essential to understand the relationship between the applied load and indentation depth or contact area for a single asperity contact. The well-known classical elastic case of a single asperity-to-asperity contact comes from the well-known analysis of Hertz (1881) on frictionless contact between two two cylinders. A spherical contact model is also presented (see Fig. 2.11) in this review as very few researchers have focused on post-yield cylindrical contact analysis in the past (Jackson, 2018).

For the case of two spheres in contact (Fig. 2.11(a)), the contact radius ($a$) and the indentation depth ($dz$) as a function of applied load ($F_e$) can be expressed as:

$$a = \left(\frac{3F_e r}{4E}\right)^{1/3} \tag{2.8}$$

$$dz = \frac{a^2}{r} = \left(\frac{9{F_e}^2}{16rE^2}\right)^{1/3} \tag{2.9}$$

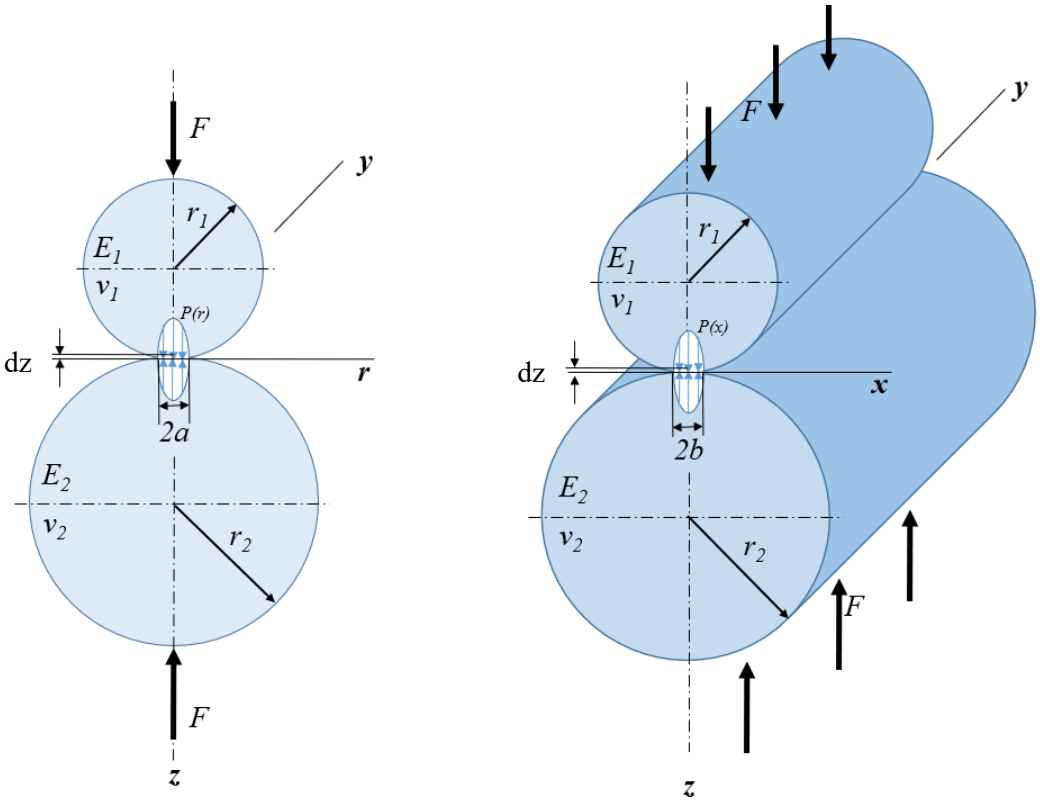


Figure 2. 11 Hertz elastic model (a) spherical contact, (b) cylindrical contact.

respectively, in which symbol $E$ is the effective elastic modulus and $r$ is the effective radius of two bodies in contact. By definition, $E$ and $r$ can be written as:

$$\frac{1}{E} = \frac{1-\nu_1^2}{E_1} + \frac{1-\nu_2^2}{E_2} \tag{2.10}$$

$$\frac{1}{r} = \frac{1}{r_1} + \frac{1}{r_2} \tag{2.11}$$

where $E_1$ and $E_2$, $\nu_1$ and $\nu_2$ are elastic moduli and Poisson's ratios of materials 1 and 2 respectively.

Rearranging Eq. 2.9, the elastic load for spherical contact can be expressed as a function of indentation depth $dz$ as:

$$F_e = \frac{4}{3} E r^{1/2} dz^{3/2} \tag{2.12}$$

The pressure distribution across the contact area can be expressed as:

$$P(r) = P_{max} \left\{ 1 - \left( \frac{r}{a} \right)^2 \right\}^{1/2} \tag{2.13}$$

where maximum pressure $P_{max}$ at *r=0* is defined as:

$$P_{max} = \frac{3}{2} P_m = \frac{3F}{2\pi a^2} \tag{2.14}$$

where $P_m$ is the mean pressure. For the case of two cylinders in contact (Fig. 2.11(b)), the half-contact width ($b$) can be expressed as:

$$b = \left( \frac{4 F_e r}{E \pi L} \right)^{1/2} \tag{2.15}$$

and the pressure distribution actross the contact area can be expressed as:

$$P(x) = P_{max} \left\{ 1 - \left( \frac{r}{a} \right)^2 \right\}^{1/2} \tag{2.16}$$

where maximum pressure is defined as:

$$P_{max} = \frac{4}{\pi} P_m = \frac{2F}{\pi b L} \tag{2.17}$$

Based on Hertz work, Johnson (1985) defined the indentation depth ($dz$) for the case of elastic cylinder-rigid flat contact and rigid cylinder-elastic flat contact as:

$$dz = \frac{2F_e}{E \pi L} \left( \ln \left( \frac{4r}{b} \right) - \frac{1}{2} \right) \tag{2.18}$$

and

$$dz = \frac{2F_e}{E\pi L}\left(\ln\left(\frac{2d}{b}\right) - \frac{\nu}{2(1-\nu)}\right) \tag{2.19}$$

respectively, where $L$ , $d$ and $\nu$ are the contact length along the cylinder's axis, characteristic depth and Poisson's ratio of the material of cylinder, respectively. In addition to Johnson's work, other authors have proposed analytical models (to name a few; Eugene, 1953; Lankarani & Nikravesh, 1994), but the most noteworthy for engineering application is the Johnson's model (Pereira et al., 2011).

#### 2.2.3.2 Yield Limit

As normal load increases, the spherical and cylindrical asperities continue to deform elastically until they reach their yield limit. Assuming that yielding is governed by Mises yield criterion, the maximum shear stress ($\tau_1$) at yield for both spherical and cylindrical contact, with $\nu$ = 0.3, are respectively (Johnson, 1985; Merwin & Johnson, 1963):

$$(\tau_1)_{max} = 0.31P_{max} \text{ at z=0.48b} \tag{2.20}$$

$$(\tau_1)_{max} = 0.30P_{max} \text{ at z=0.78b} \tag{2.21}$$

Equations (2.20 and 2.21) reveal that cylindrical contact requires deeper indentation to yield compared to spherical contact. According to Tabor (1951), the initial yielding occurs when the maximum pressure reaches $P_{max} = 0.6H$ or mean pressure reaches $P_m = 0.4H$ where $H$ refers to the hardness of the softer material. More general solution is to assume the coefficient as $K$ where the maximum pressure at yield was taken as $P_{max} = KH$ (Chang et al., 1987). Kogut & Etsion (2003), based on a finite element analysis, have identified

$K$=0.577 from their work. The yield point ($dz_y$) for spherical contact can be determined from substitution of Eqs. 2.9 and 2.12 into Eq. 2.14, (Chang et al., 1987):

$$dz_y = \left(\frac{\pi P_{max}}{2E}\right)^2 r = \left(\frac{\pi KH}{2E}\right)^2 r \tag{2.22}$$

where a value of 0.6 was chosen for $K$. Subsequently, Zhao et al. (2000) based on their analysis of spherical-flat contact defined the yield point as:

$$dz_y = \left(\frac{3\pi P_m}{4E}\right)^2 r = \left(\frac{3\pi KH}{4E}\right)^2 r \tag{2.23}$$

where $K$ was taken as 0.4. In short, when $dz \leq dz_y$ the deformation was taken as elastic while beyond this critical point ($dz > dz_y$) the contact was taken as either elastoplastic or fully plastic.

#### 2.2.3.3 Fully Plastic Regime

As further load is increased beyond the yield limit, the material will reach another critical state; the fully plastic state. Tabor (1948) proposed a connection between this critical state ($dz_{fp}$) with hardness by stating that fully plastic state is reached when the maximum pressure becomes constant and equal to the material hardness, $P_{max} = H$. On further analysis in a later work, Tabor (1970) mentioned that full plasticity is reached when the load is about 300 times the load for yielding. Based on experimental work, Johnson (1985) stated that fully plastic load $F_{fp}$ is about 400 times the load at initial yielding load, $F_y$ (Fig. 2.12).

#### 2.2.3.4 Plastic Regime: CEB Model

Chang et al. (1987) developed a model (later known as CEB model) based on volume conservation of a segment of spherical asperity during plastic deformation, as illustrated in Fig. 2.13.

Chang et al. (1987) assumed that after yielding the asperity deforms according to volume conservation, an assumption of classical theory of plasticity. The initial volume $V_{CV}$ for a frustum of a sphere can be expressed as:

$$V_{CV} = \frac{\pi l_i}{6}\left(\frac{3}{4}{a_i}^2 + \frac{3}{4}b^2 + {l_i}^2\right) \tag{2.24}$$

where $a_i$, $b$ and $l_i$ are the contact diameter of upper circular region of frustum, the diameter of lower circular region of base of frustum and height between the two circular regions of frustum, respectively.

The upper region of the frustum is located at a vertical distance $\omega_c$ below the undeformed pole of the spherical asperity. If on subsequent application of load the upper region of the frustum displaces vertically downward by $\omega_p$, equating the volumes of the material before and after the new displacement, one obtains the following relationship between current height $l$ and dimensional variables $l_i$, $\omega$ and $\omega_c$:

$$l = l_i - \omega_p = l_i - (\omega - \omega_c) \tag{2.25}$$

Note that $\omega, \omega_c$ and $\omega_p$ are referring to $dz$, $dz_y$, and $dz_p$ in the earlier notation. The new volume can be now expressed as (see Figure 2.13):

$$V_i = \frac{\pi l}{6}\left(\frac{3}{4}a^2 + \frac{3}{4}b^2 + l^2\right) \tag{2.26}$$

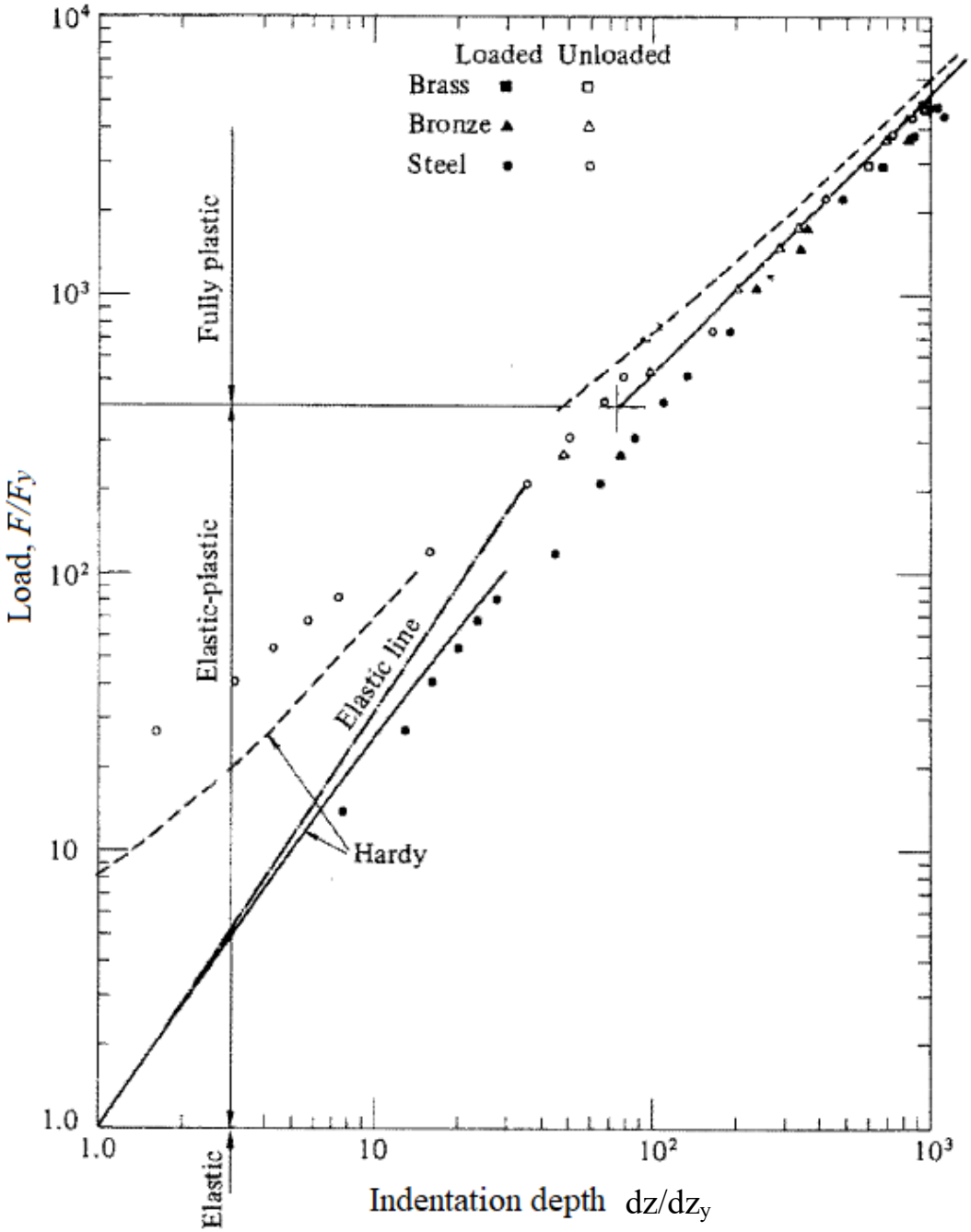


Figure 2. 12 Normalized load versus normalized indentation depth of a spherical indenter into an elastic-plastic half-space. Solid line: loading, broken line: unloading (Johnson, 1985).

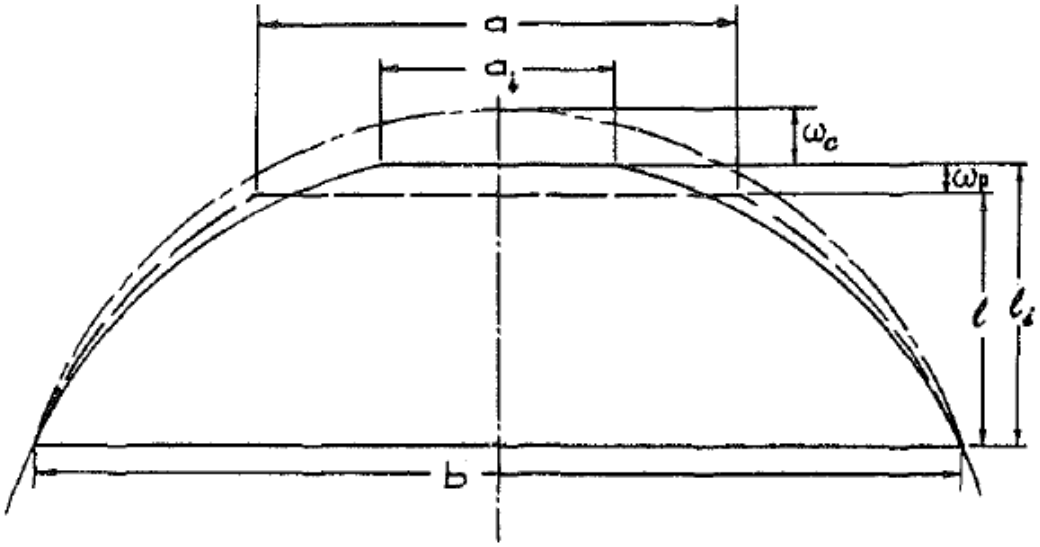


Figure 2. 13 CEB volume conservation model for a segment of spherical asperity (Chang et al., 1987).

where $a$ is the new contact diameter below the upper circular region of frustum. Equating $V_{CV} = V_i$, the parameter $a$ can be calculated. Thus, the new contact area could be determined. Chang et al. (1987) applied this theory to the GW model for the case of multiple asperities in contact. However, this CEB model suffered with a discontinuity at elastic-plastic transition. A later paper by Zhao et al. (2000), widely known as ZMC model, was able to successfully eliminate this discontinuity.

#### 2.2.3.5 Fully Plastic Regime: ZMC Model

Based on the work of Johnson (1985), the ZMC model of Y. Zhao, Maietta, et al. (2000) assumed that the contact load at fully plastic state ($F_{fp}$), was 400 times the load at yield ($F_y$) (or $F_{fp}/F_y = 400$). The methodology used to obtain the relationship between $dz_{fp}$

and $dz_y$ was described as follows: By replacing $F_e$ and $dz$ in the earlier Eqn. (2.12) with $F_y$ and $dz_y$ respectively, one obtains:

$$F_y = \frac{4}{3} E r^{1/2} {dz_y}^{3/2} \tag{2.27}$$

As fully plastic load is lower than the projected elastic load, the following expression is obtained for an upper limit for fully plastic load:

$$F_{fp} \leq \frac{4}{3} E r^{1/2} {dz_{fp}}^{3/2} \tag{2.28}$$

Also, the following expression for ratio of fully plastic load and load at yield is obtained:

$$\frac{\frac{4}{3} E r^{1/2} {dz_{fp}}^{3/2}}{\frac{4}{3} E r^{1/2} {dz_y}^{3/2}} \geq \frac{F_{fp}}{F_y} = 400 \tag{2.29}$$

Eq. (2.29) can be written as:

$$\frac{{dz_{fp}}^{3/2}}{{dz_y}^{3/2}} \geq 400 \tag{2.30}$$

and subsequently the following expression relating the displacements at fully plastic state and at yield can be written as:

$$dz_{fp} \geq 54 dz_y \tag{2.31}$$

Eqn. (2.31) indicates that the sphere in contact with a flat surface needs to be indented at least 54 times deeper than the indentation at yield to achieve a fully plastic state.

#### 2.2.3.5 Elasto-Plastic Regime: ZMC Model

To bridge elastic and plastic regimes, ZMC model also includes an elastoplastic model. Based on conditions at yield where $P_m = KH$ and at fully plastic where $P_m = H$, mean contact pressure in the elastoplastic regime was expressed as:

$$P_m = H - H(1-K)\frac{\ln dz_{fp} - \ln dz}{\ln dz_{fp} - \ln dz_y} \tag{2.32}$$

Note that ZMC model utilized a mean pressure-hardness relationship instead of the maximum pressure-hardness as defined by Tabor. Similarly, the contact area in the elastoplastic regime ($A_{ep}$) connecting the contact areas at yield ($A_y = \pi a^2 = \pi r dz_y$) and at fully plastic ($A_{fp} = \pi a^2 = 2\pi r dz_{fp}$) was expressed in the form:

$$A_{ep} = \pi r dz \left[1 - 2\left(\frac{dz - dz_y}{dz_{fp} - dz_y}\right)^3 + 3\left(\frac{dz - dz_y}{dz_{fp} - dz_y}\right)^2\right] \tag{2.33}$$

Multiplying Eqs. 2.32 and 2.33, the following expression for load in elastoplastic regime was obtained:

$$F_{ep} = \left(H - H(1-K)\frac{\ln dz_{fp} - \ln dz}{\ln dz_{fp} - \ln dz_y}\right) * \left(\pi r dz \left[1 - 2\left(\frac{dz - dz_y}{dz_{fp} - dz_y}\right)^3 + 3\left(\frac{dz - dz_y}{dz_{fp} - dz_y}\right)^2\right]\right) \tag{2.34}$$

#### 2.2.3.6 Fully Plastic Regime: Brake Model

Brake (2015) introduced an analytical spherical contact model for elastoplastic and fully plastic contact analyses. The powerful aspect of this model compared to ZMC model was the consideration of strain hardening in the plastic regime. Brake's contact model expresses contact load in the plastic regime as a function of indentation depth $dz$ as:

$$F_p = P_{max,pl}\pi \frac{(2rdz)^m}{a_p^{m-2}} \tag{2.35}$$

where the contact radius at fully plastic state ($a_p$) is expressed as:

$$a_{fp} = \left(\frac{3P_{max,pl}}{4E} 2^{m/2}\pi r^{(m-1)/2} dz_y^{(m-3)/2}\right)^{1/(m-2)} \tag{2.36}$$

In Eqs. (2.35) and (2.36), $P_{max,pl}$ is the maximum pressure at fully plastic which is equal to $\left(\frac{2}{H_1}+\frac{2}{H_2}\right)^{-1}$ and $m$ is the Meyer hardness coefficient. Here, $H_1$ and $H_2$ are defined as the hardness of the two materials in contact. According to Tabor (1951), the maximum normal pressure for the elastic regime is $P_{max,el} \approx 1.1S_y$ while the maximum normal pressure for plastic regime is $P_{max,pl} \approx 2.8S_y \approx H$ where $H$ is the effective hardness of both materials in contact. The exponent $m$ is related to the strain hardening exponent, $n_{sh}$ by $n_{sh} = m - 2$. For two dissimilar materials in contact, $m$ is chosen for the softer material. Typically, the following values are assigned to $m$; $m$=2 for elastic-perfectly plastic material, 2<m<2.5 for work hardening material, and m=3 for pure elastic material (Brake, 2015). However, it is unclear how 2.5<m<3 was addressed as the author focused exclusively on 2<m<2.5.

#### 2.2.3.7 Elastoplastic Regime: Brake Model

Brake (2015) developed a correlation for the elastoplastic regime based on a trigonometric function and by correlating Eqs. (2.12) and (2.35) as follows:

$$F_{ep} = sech(dz)\frac{4}{3}Er^{1/2}dz^{3/2} + (1 - sech(dz))P_{max,pl}\pi\frac{(2rdz)^m}{a_p^{m-2}} \tag{2.37}$$

where the first term on the right side of Eq. (2.37) refers to the elastic part and diminishes through indentation depth, while the second term refers to the plastic part and increases through indentation depth.

The disadvantage of Brake and ZMC analyses is that they did not consider the conservation of volume in their model. Also, to the best of this author's knowledge, there is no extension of elastic-work hardening plastic solid models of Brake and ZMC to multi-cylindrical asperity case.

### 2.2.4 Analysis of Mechanics of Asperity Deformation: Multi-Asperity Contact Models

As shown earlier in Figure 2.7, there is a distribution of asperities of nominally cylindrical shape but of different sizes in the TD direction. In the last five decades, many multi-asperity contact models have been developed. These models have been reviewed extensively in several papers over the years (Adams & Nosonovsky, 2000; Barber & Ciavarella, 2000; Bhushan, 1998; Müser et al., 2017; Vakis et al., 2018, to name a few). In this sub-section, multi-asperity contact models that are related to sheet metal surface are briefly reviewed along with their assumptions. These models may provide some insights

on the deformation of the surface asperities that lead to the prediction of real contact area and TCR in hot stamping process.

#### 2.2.4.1 Statistical Models

One of the most widely referred multiple asperity contact model was proposed by Greenwood & Williamson (1966), also known as GW model. This model considers a conforming contact between an elastic nominally flat rough surface and a rigid flat smooth surface. The rough surface was assumed to be covered with a large number of asperities having a Gaussian distribution of peak heights and the summits were assumed spherical with an identical tip radius. In this model, no bulk deformation was considered, and the asperities were assumed to deform independently of one another and in accordance with Hertzian elastic contact theory.

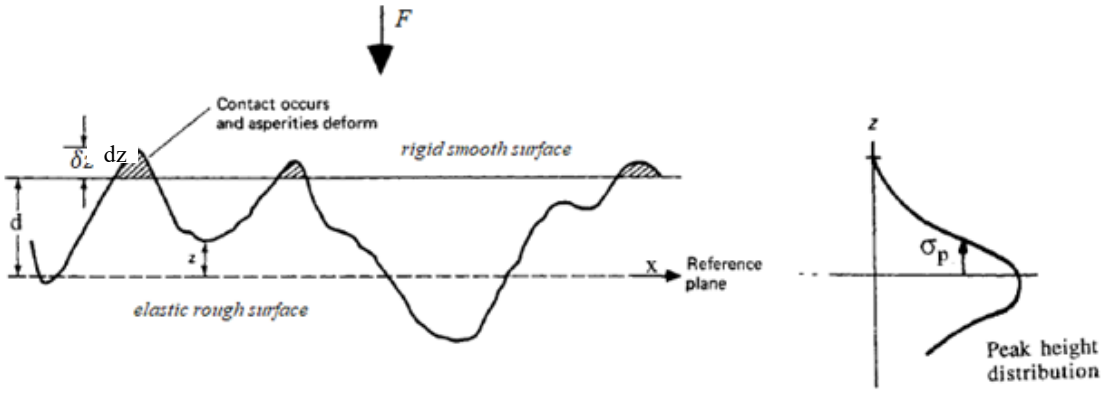


Figure 2. 14 A schematic representation of surface asperity distribution in Greenwood and Williamson model (Bhushan, 1998).

Referring to Fig. 2.14, this statistical model is based on the following probability of contact between the two surfaces:

$$\wp(z > d) = \int_d^{\infty} \frac{1}{\sqrt{2\pi}\sigma_p} exp\left\{-\frac{z^2}{2{\sigma_p}^2}\right\} dz \tag{2.38}$$

In Eqn. (2.38), $z$, $d$ and $\sigma_p$ represent the asperity height of the rough surface, the separation distance between two surfaces, and the standard deviation of asperity height, respectively. As per GW model, when the number of contacting asperities ($N$) increases and the average size of each contacting asperity is constant, then the real area of contact $A_r$ is proportional to $F^{2/3}$. Total contact area ($A$) and total contact force ($F$) of GW model can be expressed as a distribution as follows:

$$A = \pi N r \int_d^{\infty} \frac{dz}{\sqrt{2\pi}\sigma_p} exp\left\{-\frac{z^2}{2{\sigma_p}^2}\right\} dz \tag{2.39}$$

$$F = \frac{4}{3} E r^{1/2} N \int_d^{\infty} \frac{dz^{3/2}}{\sqrt{2\pi}\sigma_p} exp\left\{-\frac{z^2}{2{\sigma_p}^2}\right\} dz \tag{2.40}$$

Greenwood & Williamson (1966) concluded that the contact area depends on the contact load rather than the overall pressure. In addition, they developed a plasticity index $\Psi$ which is given by:

$$\Psi = \left(\frac{E}{H}\right)\left(\frac{\sigma}{r}\right)^{1/2} \tag{2.41}$$

The plasticity index $\Psi$ is responsible for the transition from elastic to plastic deformation; $\Psi < 0.6$ corresponds to elastic deformation, whereas $\Psi > 1$ values are associated with

plastic deformation. It is to be noted that the deformation mode within $0.6 \leq \Psi \leq 1$ remains undefined (Greenwood & Williamson, 1966).

Later, Greenwood and Tripp extended the GW model, see Greenwood & Tripp (1970), where it was shown that the contact between two nominally flat rough surfaces was not significantly different from the contact between a nominally flat rough surface and a flat smooth surface. The above works were further developed by Nayak (1973) with inspiration from the work of Longuet-Higgins (1957), who was the first to apply a random process model for analysis of random surfaces in the ocean. Nayak established a relationship between the spectral moments of the surface and the distribution of asperities, their density, curvature, and ellipticity, among others, on the assumption that a rough surface can be represented as a two-dimensional isotropic Gaussian surface.

By numerical comparisons of the GW model with other more general isotropic and anisotropic models, McCool (1986) suggested that the GW model, despite its simplicity, can give good results. However, the model has its limitation in that it can only be used in the contact problems of rough surfaces with a low plasticity index, in which the majority of contacting asperities deform elastically. For example, Powierza et al. (1992) attempted to perform an experimental verification of the GW model and found that the model is surprisingly good at predicting elastic contact phenomena. However, when the applied load exceeded about half of the yield point load, the results predicted by the GW model severely deviated from the experimental results (Fig. 2.15).

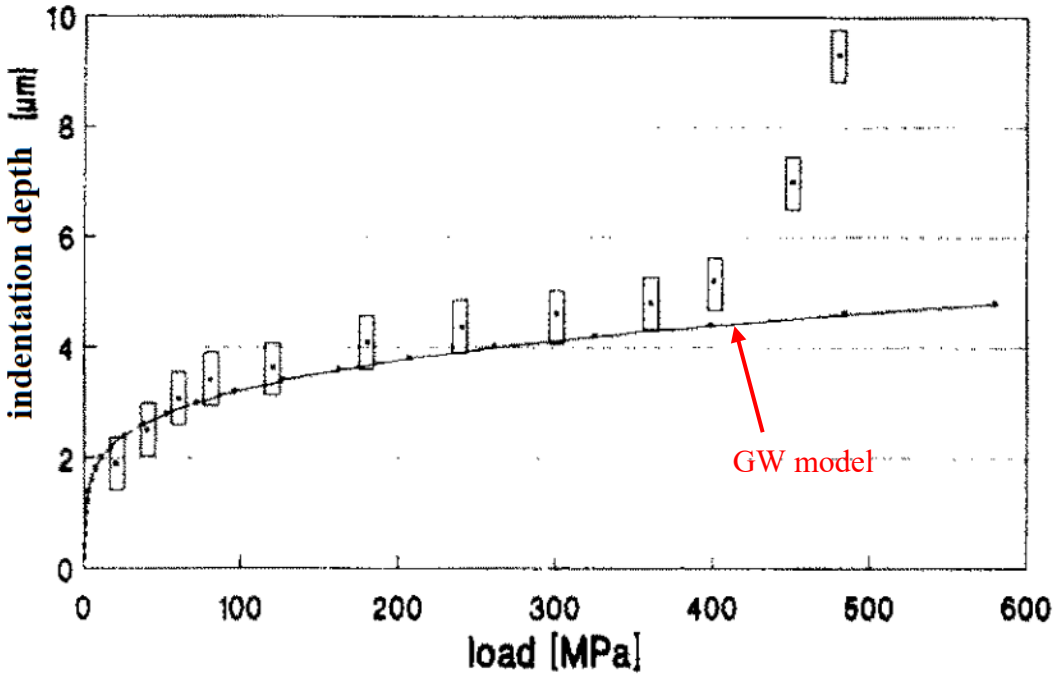


Figure 2. 15 Comparison between GW model (solid line) and experiments (data points with rectangular boundaries) with bead-blasted surface (Handzel-Powierza et al., 1992).

The results of single asperity were used by other researchers to develop a multi-asperity model for elastic– plastic deformation using assumptions similar to those of GW model. Horng (1998) proposed an elastic-plastic contact model that generalizes the CEB model by considering the directional nature of surface roughness and the elliptical shape of the contact patch. They found that the elliptical and spherical contact models deviate remarkably in regard to total real contact area and plasticity index. In addition, as mentioned previously, ZMC model also was developed as a multi-asperity model that integrates the transition from elastic deformation to fully plastic flow. For brevity, the present review of statistical models is limited to multi-spherical contact. The statistical multi-cylindrical

contact model was also developed much later by Greenwood et al. (2011). It was found that the mean real pressure for 3-D multi-cylindrical contact model is two to three times higher than for the 2-D multi-cylindrical contact model.

The weakness of statistical multi-contact models is the assumption that radius of asperities are uniform, and the asperity heights are represented by a Gaussian distribution. This may be good for ideal condition but not applicable for the real surfaces. On the other hand, the analytical work on cylindrical contact model is more complex because, (i) indentation depth ($\delta z$) is expressed as a function of load and half contact width, thus a numerical iterative technique is needed, (ii) logarithmic functions cause mathematical and physical limitations (refer to Eq. 2.18) (Pereira et al., 2011), and (iii) difficulty in experimental validation with finite length cylinder experience 'end effects' or 'crown effect'. The end effect is due to a drop in pressure at the ends due to lack of material support (Johnson, 1982).

### 2.2.5 Thermal Analysis: Constriction/Spreading Resistance

The final step in TCR determination from mechanistic method involves solving the constriction/spreading resistance problem. Referring to Fig. 2.16 below, the constriction refers to heat flow into a narrower region, whilst the spreading refers to heat flow out from the narrower region (Sharp, 2009). This important thermal parameter governs the heat flow between two contacting bodies, and depends on several factors including geometry, domain, boundary condition and time (Rohsenow et al., 1998).

### 2.2.5.1 Spherical Contact

The constriction and spreading resistance problem can be better understood by referring to Figure 2.17 below from the work of Cooper et al. (1969), hereafter referred to as CMY model. When the two surfaces are in contact, the total resistance is the sum of the constriction resistances of two asperities in contact. In the CMY model, the resistance of a single contact was idealized as 'two flux tubes' as shown in Fig. 2.17(a) where $b$ is the contact radius and $c$ is the flux tube radius.

If $k_1$ and $k_2$ are thermal conductivities of the two asperities, then the resistance associated with an individual contact pair is given by Carslaw & Jaeger (1959) with the consideration that there exists an isothermal plane between bodies in contact (Cetinkale and Fishenden, 1951):

$$R_{two\ flux\ tubes} = \frac{\psi}{4bk_1} + \frac{\psi}{4bk_2} = \frac{\psi}{2bk} \tag{2.42}$$

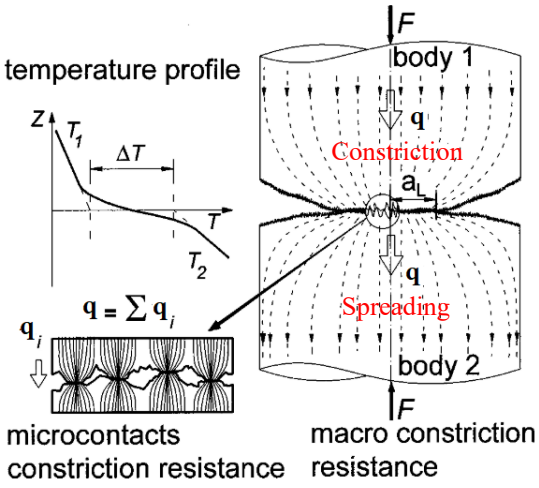


Figure 2. 16 Constriction and spreading resistance in the micro- and macro-contact regions (Bahrami et al., 2006).

where $\psi$ is thermal constriction parameter. This parameter describes the heat flow paths between real contact areas. In Equation (2.42), $k$ is the mean thermal conductivity, expressed as:

$$k = \frac{2k_1k_2}{k_1+k_2} \tag{2.43}$$

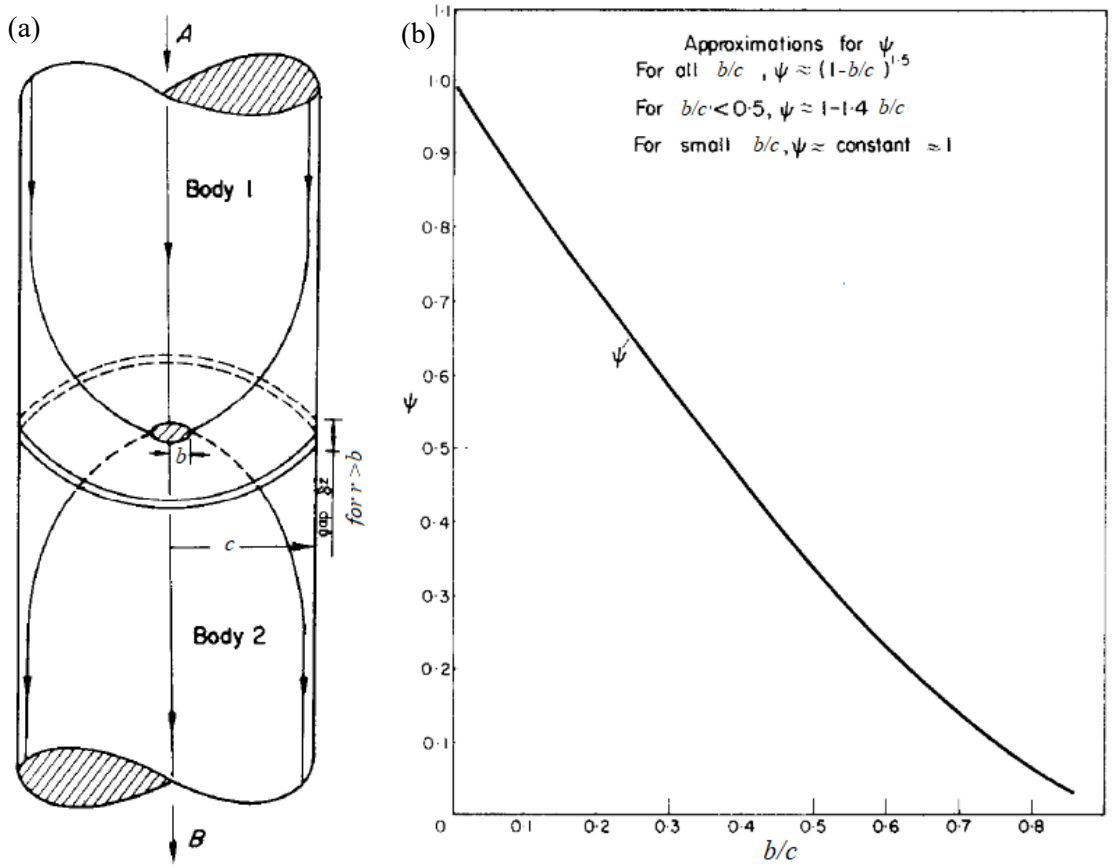


Figure 2. 17 (a) Two flux tubes (b) Thermal constriction parameter (CMY model).

where $k_1$ and $k_2$ are individual thermal conductivities of two solids in contact. Parameter $\psi$ is a function of ratio $b/c$ as per CMY model. The relationship is shown graphically in Figure 2.17(b). Numerous correlations of the thermal constriction parameter have been developed

(e.g. Cooper et al., 1969; Mikic & Rohsenow, 1966; Negus et al., 1988). The simplest and commonly used correlation was proposed by Cooper et al. (1969) as:

$$\psi = \left(1 - \frac{b}{c}\right)^{1.5} \tag{2.44}$$

Note that this is the equation that is plotted in Figure 2.17(b). For simplicity, it is typically assumed that all contact surfaces experience the same $\psi$ value and all asperities contact in the same manner, as shown in Fig. 2.17(a). However, this is an ideal case. Solid-to-solid contact resistance can be expressed as:

$$R_c = \frac{\psi}{2nbk} \tag{2.45}$$

where *n* is the number of contacting asperities and can be determined from surface profile analysis.

In another study, Yovanovich & Kitscha (1973) developed a simplified thermal resistance for spherical-flat contact, in which there was no thermal constriction parameter involved. The correlation was expressed as:

$$R_c = \frac{1}{k\left({}^{6Fr}/_{E}\right)^{1/3}} \tag{2.46}$$

Cooper et al. (1969) developed their multi-spherical contact model assuming that all contacting asperities deform plastically and the asperity heights have a Gaussian distribution. Also, asperities deform and their slopes evolve independently.

Based on Fig. 2.18, M. M. Yovanovich (2005) modelled the asperities as cone-like peaks where $R_{q1}$, $R_{q2}$, and $m_1$, $m_2$ were the root mean square (or RMS) surface roughness and slopes of the asperities of the two contacting surfaces, respectively.

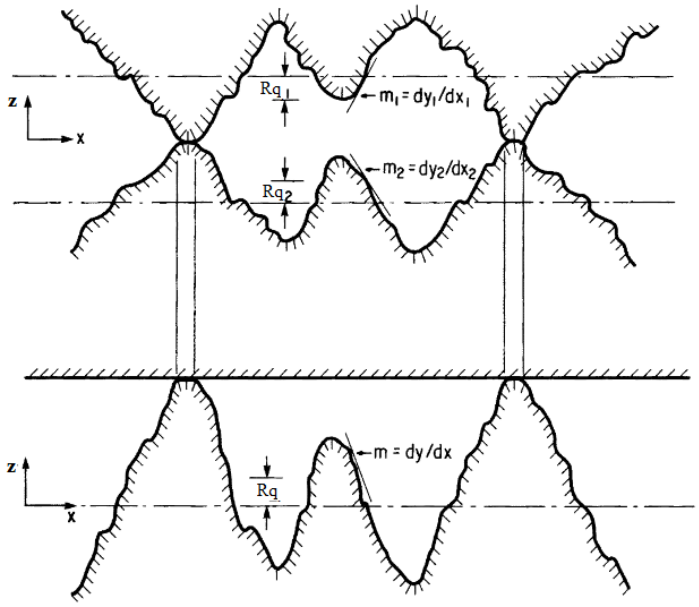


Figure 2. 18 Joint formed by two conforming rough surfaces (M. M. Yovanovich, 2005).

The effective surface roughness and asperity slope were defined as follows:

$$R_q = \sqrt{{R_{q1}}^2 + {R_{q2}}^2} \tag{2.47}$$

$$m = \sqrt{{m_1}^2 + {m_2}^2} \tag{2.48}$$

In addition, a correlation between real contact area ($A_r$) and the hardness was expressed as:

$$\frac{A_r}{A} = \frac{P}{H} \tag{2.49}$$

where *P, H* and *A* are nominal pressure, effective micro-hardness of the softer surface and nominal contact area respectively. Finally, CMY suggested the following expression between $R_c$ and quantities *(k.m/$R_q$),* and *(P/H)* in their solid-to-solid resistance model:

$$R_c = 0.6897 \left(\frac{R_q}{k.m}\right)\left(\frac{P}{H}\right)^{-0.985} \tag{2.50}$$

This correlation was shown to agree well with experimental work (Cooper et al., 1969).

The weakness of CMY model is the assumption of a uniform distribution of contact areas. In reality, all the asperities are distributed randomly and contact in different ways with the other asperities (Cooper et al., 1969). Neglecting the variation of $\psi$ will result in under-prediction of the resistance through the contact (Das & Sadhal, 1999; Laraqi & Bairi, 2002).

#### 2.2.5.2 Cylindrical Contact

Since this research work deals with cylinder-flat contact, it would be useful to review the work of McGee and co-workers (McGee, 1982 and McGee et al., 1985). They developed thermal constriction resistance model for a line contact that has been more recently used to analyze nanowire and nanotube interfaces (Bahadur et al., 2005; Cola et al., 2009; Yu et al., 2006). This constriction resistance model is a hybrid of cylindrical constriction by Yovanovich & Coutanceau (1969) and line constriction by Veziroglu & Chandra (1969). Similar to the spherical contact, the constriction was developed on the premise that two bodies in contact have an isothermal point (Cetinkale & Fishenden, 1951).

Veziroglu & Chandra (1969) showed the steady-state isotherms and heat flow lines for a 2-D symmetrical line constriction (see Fig. 2.21). The heat flow channel width, the constriction width and the geometric parameters are 2b, 2c and $L$, respectively. Note that the length of the constriction is normal to the page. The governing equation and boundary conditions are as follows:

$$\frac{\partial^2 T}{\partial x^2} + \frac{\partial^2 T}{\partial z^2} = 0 \tag{2.51}$$

$$\left(\frac{\partial T}{\partial x}\right)_{x=0} = 0 \qquad 0 < z < \infty \tag{2.52a}$$

$$\left(\frac{\partial T}{\partial x}\right)_{x=c} = 0 \qquad 0 < z < \infty \tag{2.52b}$$

$$\left(\frac{\partial T}{\partial z}\right)_{z=0} = 0 \qquad b < x < c \tag{2.52c}$$

$$(T)_{z=0} = const. \qquad 0 < x < b \tag{2.52d}$$

Solving the governing equation (2.51) with the associated boundary conditions (2.52), Veziroglu & Chandra derived an expression for the constriction resistance of a line contact as:

$$R_F = \frac{1}{\pi L k_F} ln\left(\frac{2r}{\pi b}\right) \tag{2.53}$$

where $k_F$ is the thermal conductivity of the flat.

Subsequently, the constriction resistance for a full cylinder solution was developed by Yovanovich & Coutanceau in which they used a conformal transformation to map the

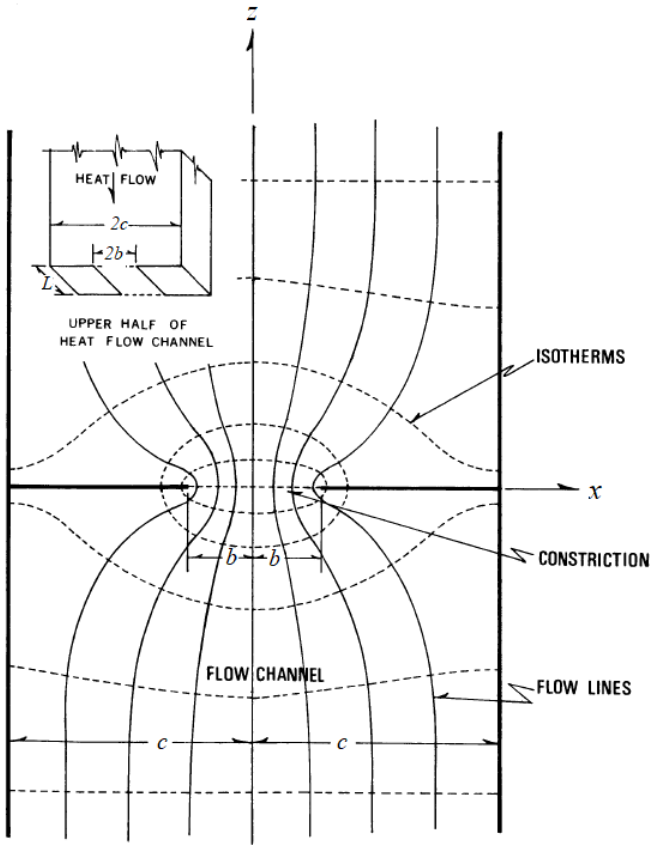


Figure 2. 19 Heat flow lines and isotherms in 2-D symmetrical constriction (Veziroglu & Chandra, 1969).

geometry of Fig. 2.20(a) onto the complex plane as shown in Fig. 2.20(b). Provided the angle θ << 1 or θ << 57°, the shape factor of Yovanovich may be used to estimate the thermal resistance of this geometry. This result is then transformed back to the Cartesian plane, yielding:

$$R_c = \frac{1}{\pi L k_C} ln\left(\frac{4r}{b}\right) \tag{2.54}$$

where $k_c$ is the thermal conductivity of the cylinder.

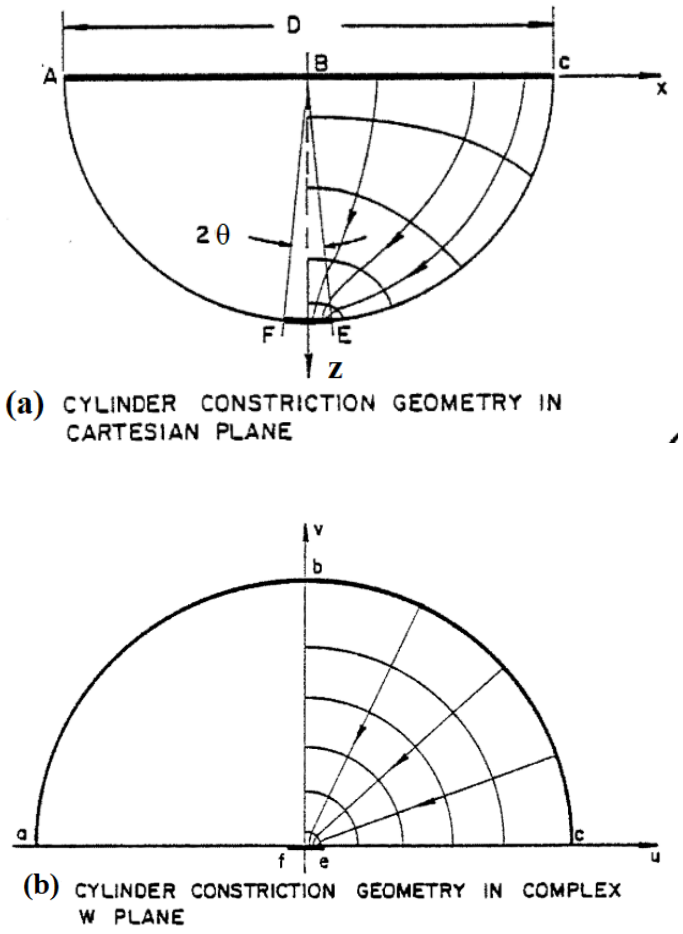


Figure 2. 20 Geometry and potential fields for cylinder constriction solution (Yovanovich & Coutanceau, 1969).

It is to be noted that this expression includes the conducting material resistance:

$$R_{mat} = \frac{1}{2Lk_C} \tag{2.55}$$

which occupies the half cylinder. Thus, the net constriction resistance of a full cylinder is:

$$R_c = \frac{1}{\pi Lk_C} ln\left(\frac{4r}{b}\right) - \frac{1}{2Lk_C} \tag{2.56}$$

Combining Eqs. 2.53 and 2.56, the constriction resistance for an isothermal strip in cylinder-flat contact is:

$$R_c = \frac{1}{\pi L k_C} ln\left(\frac{4r}{b}\right) - \frac{1}{2Lk_C} + \frac{1}{\pi L k_F} ln\left(\frac{2r}{\pi b}\right) \tag{2.57}$$

In comparison to spherical contact (Eq. (2.42), cylindrical resistance appears to have a simpler constriction resistance expression that does not require a constriction parameter.

### 2.2.6 Thermal Analysis: Air Gap Resistance

This sub-section briefly summarizes a well-established procedure in the literature for estimating the air gap.

#### 2.2.6.1 Flat, Smooth, Parallel Contact

If the air gap in the asperity region between the solids is considered as a uniform continuum, the well-known Fourier's law of heat conduction applies, and the air gap resistance, $R_{air}$, may need to be considered in the overall determination of TCR. Yovanovich (1981) defined $R_{air}$ as follows:

$$R_{air} = \frac{\delta + g_1 + g_2}{k_{air}} \tag{2.58}$$

where $k_{air}$, $\delta$ and the two $g$ values are thermal conductivity of the air, mean separation distance of the air gap and temperature jump distances, respectively (see Figure 2.21).

According to Madhusudana (2014) the temperature jump arises from inefficiency in the energy transfer between the gas molecules and the solid surfaces during a single collision. Thus, when heat is conducted across two parallel plates separated by a distance

$\delta$, the temperature distribution within the air boundary layer is shown in Fig. 2.21. Kennard (1938) gives the following equation for the temperature jump distance:

$$g = \left(\frac{2-\alpha}{\alpha}\right)\left(\frac{2}{\gamma+1}\right)\left(\frac{k_{air}}{\mu C_v}\right)\lambda \tag{2.59}$$

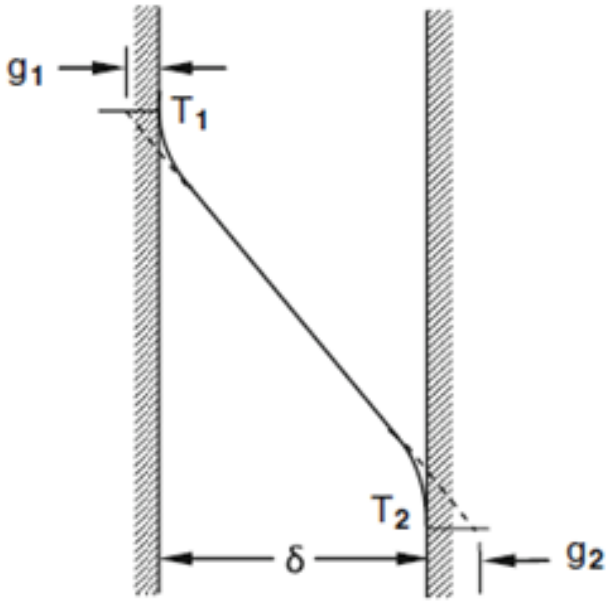


Figure 2. 21 Mean separation distance of air gap and temperature jump distance (Madhusudana, 2014).

where $\alpha$, $\gamma$, $\mu$ and $\lambda$ are thermal accommodation coefficient, ratio of specific heats for the air at constant pressure to constant volume ($C_p/C_v$), viscosity of the air, and air mean free path respectively. The thermal accommodation coefficient represents the level of kinetic energy exchange of an air molecule when it collides with a solid wall.

### 2.2.6.2 Cylindrical Contact

McGee et al. (1985) model describes a method to determine air gap resistance for cylinder-flat contact. From Fig. 2.22, due to symmetrical geometry, the cylinder-flat contact could be represented as a quarter cylinder. Unlike parallel contact, the projected area between cylinder and flat along x direction is not consistent, this complicates the determination of air gap resistance. McGee et al. (1985) proposed three models: decoupled model (DM), half-space model (HSM), and parallel flux-tube model (PFTM).

In this review, however, only DM and PFTM will be presented. DM is oversimplified model in which the surface temperature at the solid-gas interface is independent of the temperature field within the solid while PFTM is the more accurate model in which the temperature distribution at the solid-gas interface is induced by linear heat flow through the narrow, parallel heat flux channels in both the solid and gaseous regions. The equations for DM and PFTM models respectively are:

$$R_{air,DM} = \frac{1}{2Lk_{air}\int_b^r \frac{dx}{\delta(x)+\alpha\beta\lambda}} \tag{2.60}$$

$$R_{air,PFTM} = \frac{\Delta T_c}{2L\Delta T_o \int_b^r \frac{dx}{\frac{2r}{k_s}+\frac{\delta(x)+\alpha\beta\lambda}{k_{air}}+\frac{\delta(x)}{k_c}}} \tag{2.61}$$

where $k_C$ and $k_s$ are thermal conductivity of cylinder at contact and effective thermal conductivity respectively. The symbols $\Delta T_c$ and $\Delta T_o$ represent temperature difference at contact and temperature difference between cylinder and flat from thermocouple reading respectively.

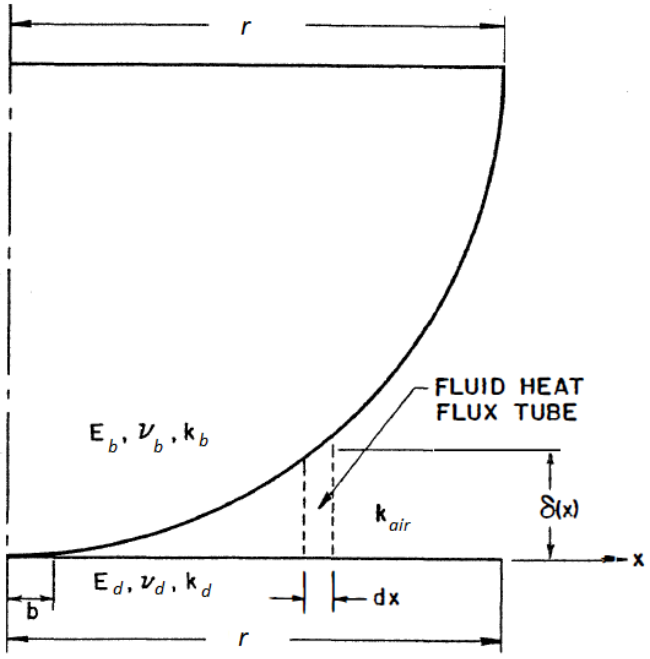


Figure 2. 22 McGee's cylinder-flat model (McGee, 1982).

Parameters $\alpha$, $\beta$ and $\delta(x)$ are defined as:

$$\alpha = \frac{2-\alpha_{C,air}}{\alpha_{C,air}} + \frac{2-\alpha_{F,air}}{\alpha_{F,air}} \tag{2.62}$$

$$\beta = \frac{2\gamma}{Pr(1+\gamma)} \tag{2.63}$$

$$\delta(x) = \sqrt{r^2 - b^2} - \sqrt{r^2 - x^2} + \frac{4F}{\pi EL}\left[\left(\frac{x}{b}\right)\sqrt{\left(\frac{x}{b}\right)^2 - 1} - \cosh^{-1}\left(\frac{x}{b}\right) - \left(\frac{x}{b}\right)^2 + 1\right] \tag{2.64}$$

where $\alpha_{C,air}$, and $\alpha_{F,air}$ are thermal accommodation coefficient of cylinder-air and flat-air, respectively. Bahrami et al. (2004) conducted series of experiment to observe the effect of contact load on solid-solid ($R_c$) and (nitrogen) gas gap ($R_g$) resistances. As expected, they found that solid-solid resistance decreases while gas gap resistance is unchanged at higher

loads (see Fig. 2.23 below). This result indicates that the influence of air gap will diminish at higher loads in HS/DQ application, and thus it may be disregarded.

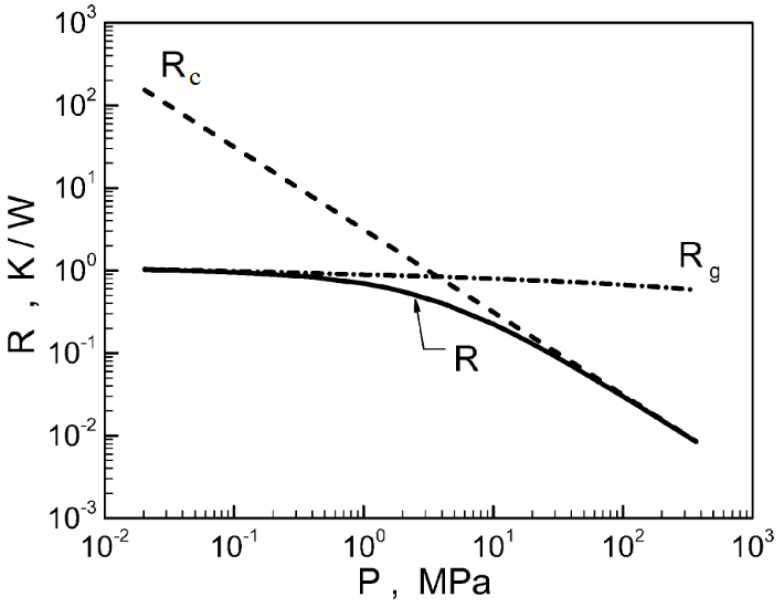


Figure 2. 23 Effect of pressure P on solid-solid and gas gap resistances (Bahrami et al., 2004).

where $\sigma$, $\varepsilon_1, \varepsilon_2$, $T_m$ and $A$ are Stefan-Boltzmann constant ($4.57*10^{-8}$ [$W/m^2K^4$]), emissivity values for two solid bodies 1 and 2, average temperature between two solids, and nominal contact area, respectively.

### 2.2.7 Thermal Analysis: Radiation Resistance

#### 2.2.7.1 Spherical Contact

According to Yovanovich & Kitscha (1973), the radiation resistance across the spherical contact surfaces is expressed as:

$$R_r = \frac{\left(\frac{1-\varepsilon_1}{\varepsilon_1}+\frac{1-\varepsilon_2}{2\varepsilon_2}+0.5766\right)}{4A_n\sigma {T_m}^3} \tag{2.65}$$

#### 2.2.7.2 Cylindrical Contact

McGee (1982) further developed radiation resistance for cylinder-flat contact based on an enclosure with three sides (Fig. 2.24). It was assumed that the cylinder and flat surface temperatures $T_C$ and $T_F$ respectively are isothermal and vertical side of the enclosure is adiabatic re-radiating surface. The fluid (air) filling the enclosure was further assumed to be transparent and did not participate in radiant heat exchange. The radiation resistance across the cylinder and flat surfaces was given by:

$$R_r = \frac{\left[\frac{1-\varepsilon_F}{\varepsilon_F}+\frac{\pi+2-4F_{fc}}{\pi-2{F_{fc}}^2}+\frac{2(1-\varepsilon_C)}{\pi\varepsilon_C}\right]}{8\sigma rL{T_m}^3} \tag{2.66}$$

where $\varepsilon_F$, $\varepsilon_C$ and $T_m$ are emissivity for flat and cylinder, and average temperature of flat and cylinder respectively. Shape factor $F_{fc}$ is defined as:

$$F_{fc} = \frac{\pi}{4} - \left(1 - \frac{\pi}{4}\right)\frac{r}{L} \tag{2.67}$$

It is to be noted that there are very few experimental studies related to gas radiation resistance. Olsen et al. (2002) conducted an experimental study of gas radiation across

contacting surfaces and reported that radiation could be disregarded below 500 K (Fig. 2.25).

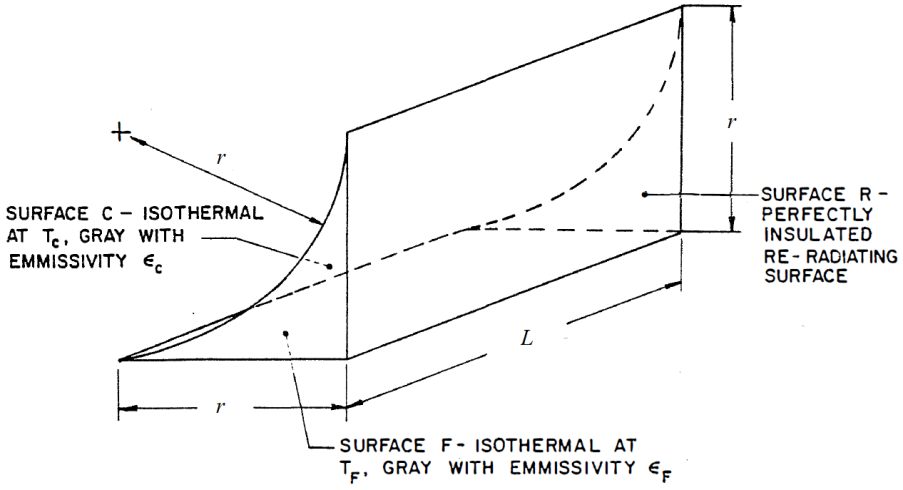


Figure 2. 24 Radiation enclosure with three different sides (McGee, 1982).

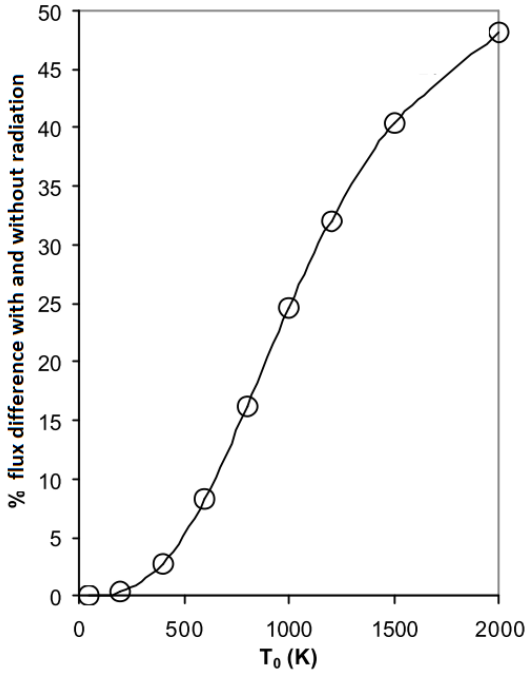


Figure 2. 25 Effect of radiation at different temperature (Olsen et al., 2002).

## 2.3 Prediction of IHTC using Mechanistic Models Versus Experimental Results

Very few studies have utilized the mechanistic approach towards prediction of IHTC (or TCR area) in the context of HS/SQ process. An attempt was made by Caron et al. (2013) to compare the IHTC value predicted from mechanistic model with one determined from solid-to-solid heat conduction from experimental thermal data and inverse heat conduction method. As noted earlier, they used CMY model for the mechanistic method and also compared their results with those obtained by Abdulhay et al. (2011), Merklein et al. (2009) and Bosetti et al. (2010), see Figure 2.26. It is to be noted that Abdulhay et al. utilized Beck's inverse method while Merklein and Bosetti used heat balance method to calculate the IHTC values.

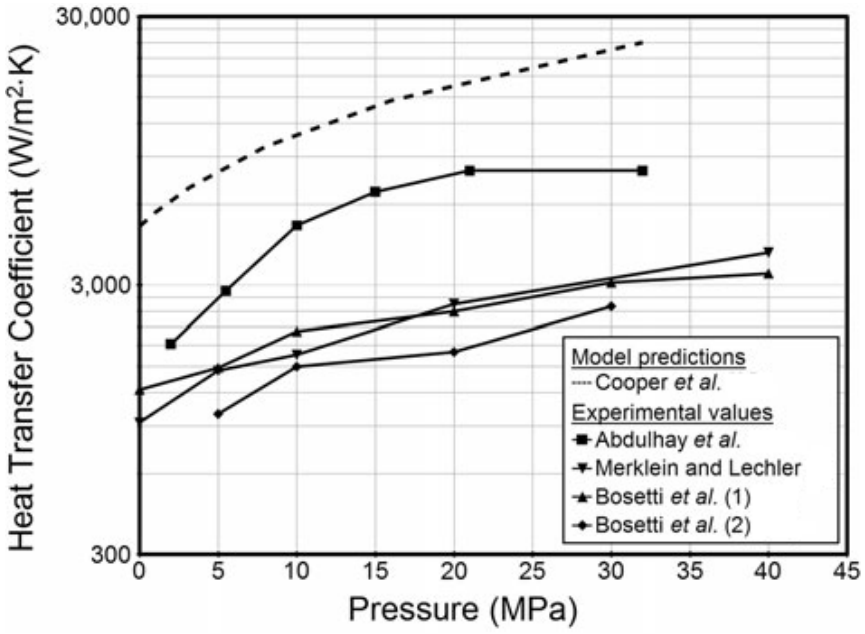


Figure 2. 26 Mechanistic (dashed) vs. experimental IHTC (Caron et al., 2013).

From Fig. 2.26 it is to be noted that the mechanistic model curve (shown as a dashed line) overpredicted the IHTC values in contrast to the other experiments. Caron et al. (2014) further analyzed the discrepancy between these values and concluded that it could be attributed to the transient nature of the stamping process.

According to McWaid & Marschall (1992) the available theoretical equations (including CMY model) have been developed for steady-state experiments involving long cylindrical bodies with flat ends in contact. It should be noted that hot stamping experiments involve large flat but quite thin sheet as one of the bodies, and predominantly transient temperature conditions. Therefore, a new mechanistic method for TCR area prediction applicable to transient HS/DQ process and elastoplastic deformation of rolled sheet multi-asperity asperity geometry is needed.

## 2.4 Effect of Lubrication

It is common to use lubricating oil or grease between the tool and blank in HS/DQ process. This additional material between the contacting solid surfaces will likely affect the value of IHTC. High thermal conductivity lubricant such as graphite, for example, can enhance the IHTC between the two contacting bodies (Burte et al., 1990; X. Liu et al., 2017). Figures 2.3(a) and 2.27 show the test jig and results of X. Liu et al. (2017) under dry and graphite lubricant coating conditions for different thickness of AA6082 aluminum blanks. A saturation in IHTC value is demonstrated under both dry and lubricated contact conditions and the IHTC versus contact pressure curve for lubricated contact conditions is situated above the dry contact conditions.

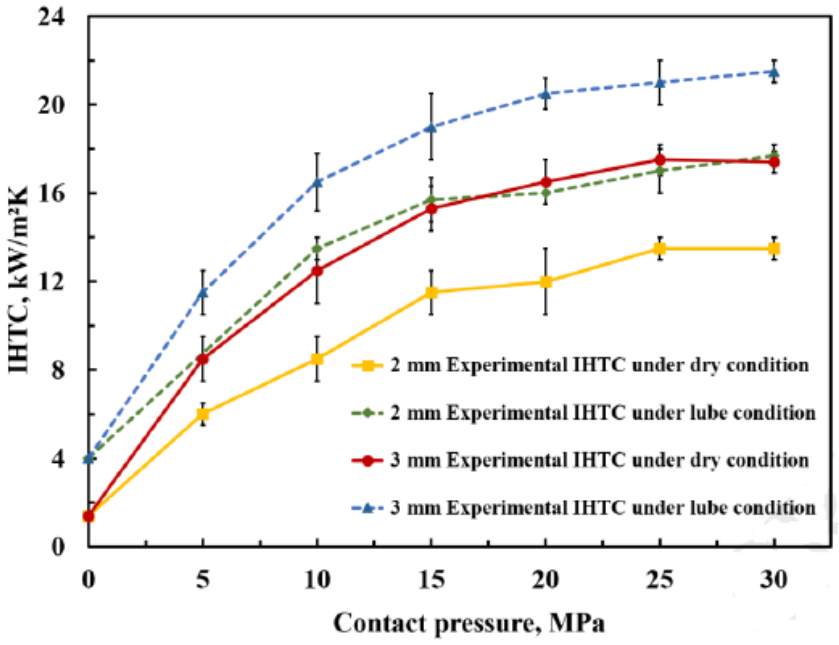


Figure 2. 27 IHTC measurement under dry and lubricated contact conditions, IHTC versus contact pressure curves with and without graphite lubricant (X. Liu et al., 2017).

Wilson et al. (2004) developed a correlation between IHTC (of lubricated surfaces) as a function of thermal conductivity of lubricant, die and blank as follows:

$$h_l = \frac{1-A}{l_f} \frac{2k_f k_t k_w}{2k_t k_w - k_w k_f - k_f k_t} \tag{2.68}$$

where $A$ is the lubricated apparent contact area, $l_f$ is the lubricant layer thickness, and $k_f$, $k_t$ and $k_w$ are the thermal conductivities of the lubricant, die and blank, respectively.

It is to be noted that most researchers have assumed that the lubricant was uniformly applied to the blank and dies and remained constant throughout the study. However, in the real situation, the thickness of lubricant layer is expected to change due to the sliding of the blank/dies contact and from variability in applied pressure during forming. In fact, Wilson

(1978) found that the thickness of lubricant layer was lower in the higher contact pressure region and the farther sliding distances. The works of Wilson and Liu et al. suggest that IHTC determination using the mechanistic approach should consider the lubrication effect.

## 2.5 Summary

Although Beck's method has been used by many researchers for TCR area prediction in hot stamping application, and has shown generally good reliability for simple two sided planar contacts, this method is difficult to apply to hot stamping of blanks to form real parts which involves not only planar but also tool-blank contact along curved surfaces. The estimation of IHTC depends critically on experimental temperature measurement using thermocouples embedded within moving forming tools many of which are inaccessible and often quite difficult to incorporate in complex shaped tools.

Additionally, the physical characteristics of the contacting surfaces such as air gaps and asperity contact mechanics are not considered in the Beck's method, and the IHTC results of the embedded thermocouple based temperature measurements in this approach may not be easily transferable to other surfaces and contact conditions. Thus, IHTC measurement from the mechanistic method, requiring no such temperature measurements within the tools, may offer a promising alternative to the Beck's method provided aspects of rolled sheet asperity geometry and elastoplastic deformation of multi-asperities at elevated temperatures are considered.

The recent work of Caron et al. (2013) on prediction of IHTC in HS/DQ process based on mechanistic CMY model appears insufficient and needs a re-examination in the

context of the rolled surface topography of the blank materials. In fact, the three major weaknesses of the current mechanistic models for IHTC prediction for hot stamping application are;

(i) assumption of cone-shaped or hemispherical asperity peaks which are distinctly different from linear asperity pattern of the rolled blank,

(ii) Gaussian distribution of asperities heights which may not applicable to the real surface, and

(iii) lack of consideration of changing blank and die surface temperatures and their effect on asperity deformation and other physical characteristics of the mechanistic model.

The current study is an attempt to address the above limitations of the mechanistic model for hot stamping applications.

# Chapter 3

## Experimental Study

This chapter is made up of three parts. The first and second parts deal with experimental setup and details for conducting conduction heat transfer experiments under planar contact and normal loading of elevated temperature AA7075 blank and room temperature stainless steel dies as well as characterisation of deformed blank surface topography after loading. The third part involves analysis of experimental data where Beck's inverse calculation procedure is implemented in a computer program to obtain thermal contact resistance (TCR area) under transient AA7075 blank cooling and stainless steel die heating conditions after contact and loading. The last part also deals briefly with comparing the Beck's method, typically used for TCR area determination during hot stamping conditions, with the proposed mechanistic method of TCR area determination that will be presented in the next chapter.

### 3.1 Preparation of Die Surfaces

Both the upper and lower die contacting surfaces with AA7075 blank were polished to a mirror surface while the original rolled AA7075 blank surface was retained. It is to be noted that the model assumes the contact and loading to be between flat, smooth, rigid surface (stainless steel die), and flat, rougher (from the rolling process) and deformable AA7075 blank. Each die surface was first machined on a lathe and then subjected to manual (hand-held specimen) polishing using an experimental protocol. The image of polished die surface

and its polishing holder can be seen in Fig. 3.1. Subsequently, the die surface was examined for its surface topography prior to its use in asperity flattening experiments on the AA7075 blank to ensure that its surface is considerably smoother compared to the AA7075 blank.

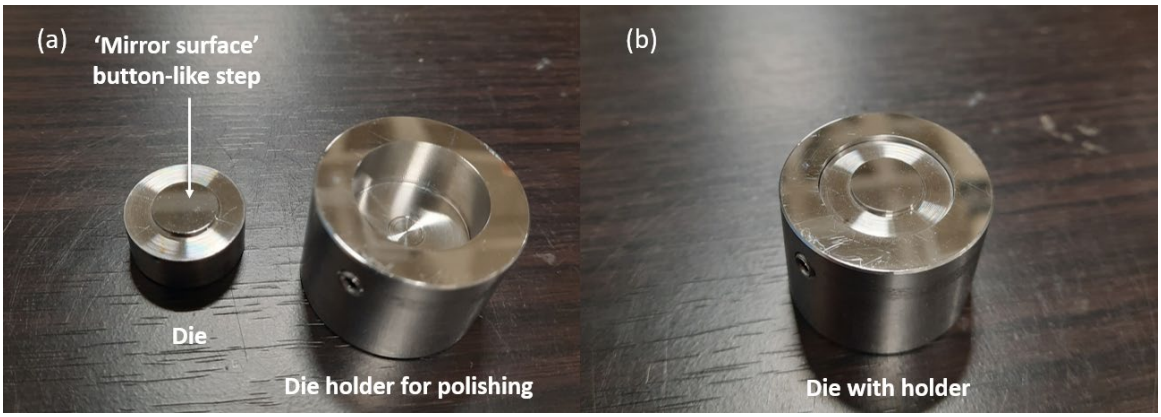


Figure 3. 1 Die and its polishing holder (a) before and (b) after assembled.

## 3.2 Characteristics of Die Surface

Figure 3.2 presents the 2D profile of the stainless steel die surface as measured from Alicona InfiniteFocus G5 optical profilometer. The magnification of the objective lens used in the measurement is 50x. It is to be noted that the sides of peaks and valleys appear to be steeper than actual as the vertical scale is magnified by 500 times compared to the

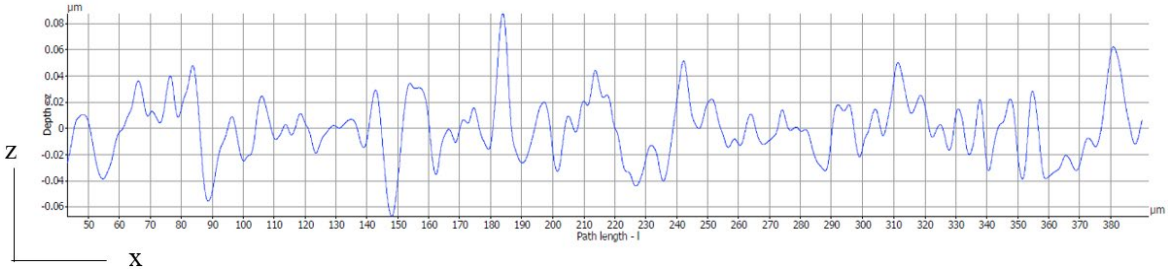


Figure 3. 2 Initial stainless steel die 2D surface roughness profile from Alicona system.

horizontal scale. The die surface has root-mean-square (RMS) roughness values of 0.023 μm. These values are 30 times smaller in magnitude than for the initial AA7075 blank surface of average surface roughness of 0.677 μm, as discussed in the next sub-section.

In addition, the die surface also was scanned by Tosca 400 atomic force microscope (AFM) to obtain 3D profiles. AFM is considered one of the most effective surface measuring instruments (Poon & Bhushan, 1995) but has limited scanning length up to 100 μm. This effectively means the roughness measurement from AFM could not represent the overall roughness of a surface. Thus, the roughness data from Alicona profilometer was preferred in this study. Figure 3.3 shows the 3D topography of the die surface where the stainless steel die has an isotropic and smooth surface. It is to be noted that some anomalies appear in the image such a sharp high amplitude peaks which are not a part of the surface but merely artefacts due to experimental equipment disturbances, typically, acoustical and mechanical vibrations (Eaton & West, 2010).

One may question if the roughness of the die surface would change throughout the experiment, thus affecting one of the model assumptions that deals with the smoothness of stainless steel surface. The die surface was re-analyzed after it had been utilized to press hot AA7075 blank for 40 times to various compressive loads up to a maximum of 15.6 kN. It was revealed that the new RMS roughness parameter had become 0.039 μm higher than the initial value. This roughness change is not significant and still a magnitude smaller than the initial blank surface.

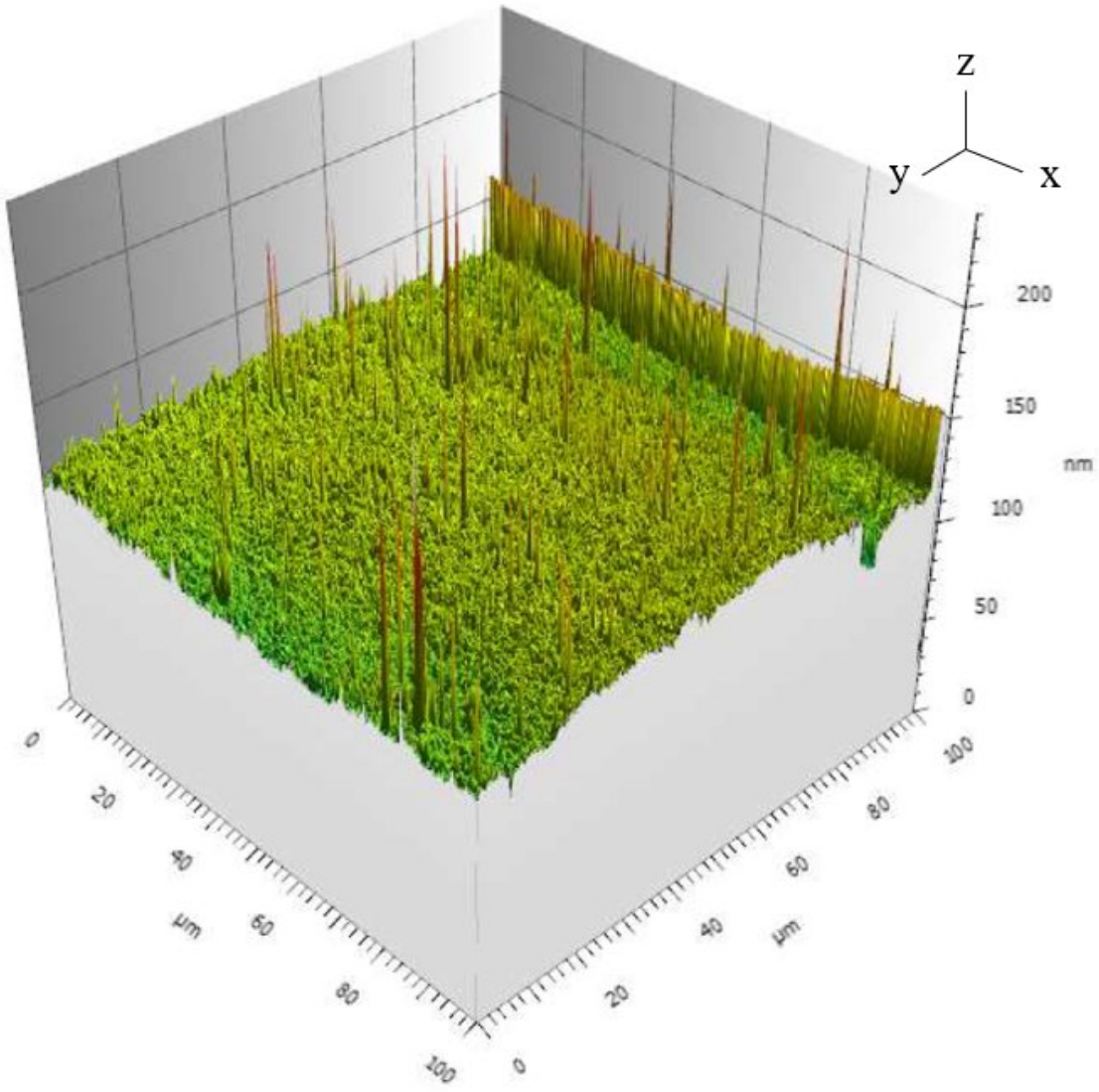


Figure 3. 3 Initial stainless steel 3D die surface topography from AFM.

## 3.3 Characteristics of Blank Surface

Figure 3.4 illustrates the initial AA7075 blank surface profile from Alicona profilometer over a horizontal distance (i.e., length) of about 1.4 mm. The peaks and valleys are plotted on a vertical scale of ±0.8 µm. Due to such a large difference in the horizontal and vertical

scales, the slopes of the peaks and valleys appear rather steep. If one compares the range of asperities height between the die (±0.04 μm, refer to Figure 3.2) and the initial blank surface (average RMS roughness value of 0.677 μm from three independent measurements), it is clear that the die surface is quite smooth in comparison.

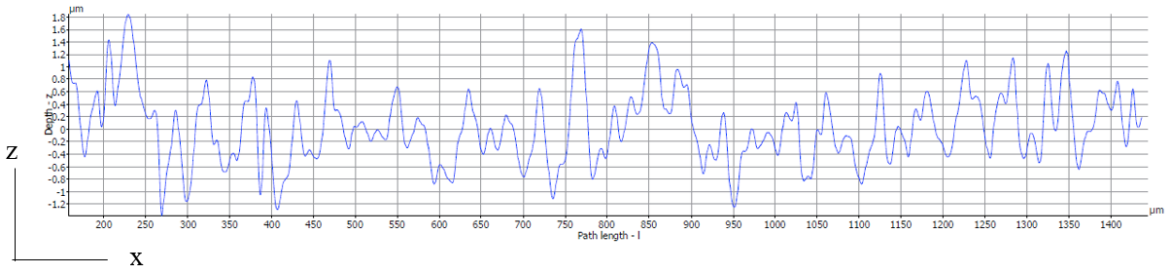


Figure 3. 4 Initial AA7075 blank surface roughness profile.

The 3-D topography of the AA7075 blank surface can be seen in Fig. 3.5(a). It is obvious that the AA7075 blank has a typical anisotropic topography of a rolled surface. A mill-finish surface of a rolled sheet manifests itself as roll lines to the unaided eye on a smooth sheet surface. However, this surface at higher magnifications exhibits asperities peaks and valleys transverse to the rolling direction (i.e., along y-axis). The initial blank surface is further analyzed by using JOEL 6610LV scanning electron microscope (SEM). Figure 3.5(b) shows SEM image of blank surface under 500 times magnification and accelerating voltage of 10 kV. The asperity peaks and valleys are clearly distinguished and the change of width of peaks lines during loading will be used for real contact area calculation. Based on the above figures, the asperities peaks could be assumed and modeled as a cylindrical segment with different radii and heights.

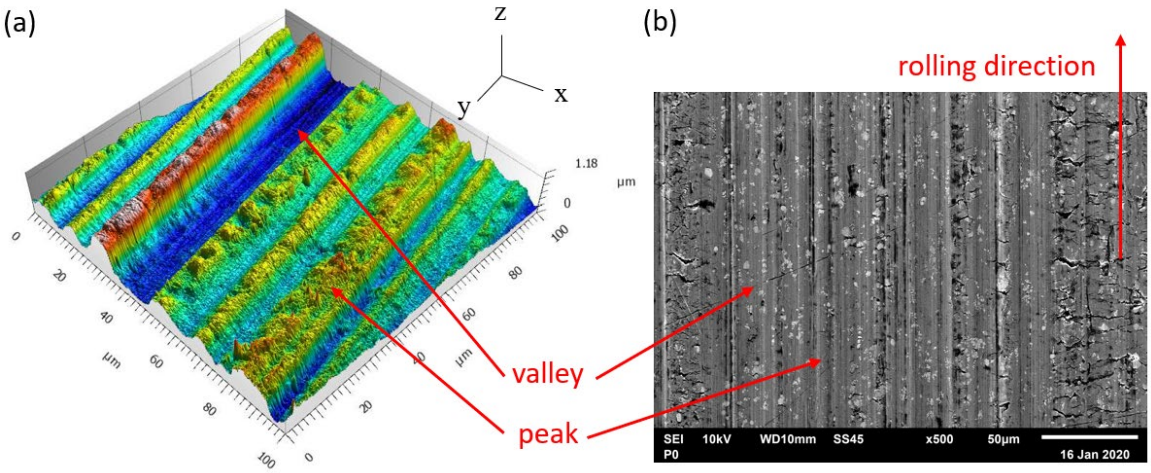


Figure 3. 5 (a) Initial AA7075 blank surface, and (b) 3D topography and SEM image.

## 3.4 Model Input Material Properties

For the modeling work, material properties for both contacting surfaces, such as elastic modulus ($E$), Poisson's ratio (ν), hardness ($H$), yield stress of AA7075 blank ($S_y$), thermal conductivities of two contacting bodies ($k_1$ and $k_2$), and Meyer's hardness coefficient ($m$) were extracted from literature and also from experiments, if unavailable or unreliable.

Since the applied loading between hot AA7075 blank and cold (room temperature) stainless steel punch in hot stamping occurs at elevated temperature, the temperature-dependent elastic modulus, Poisson's ratio and thermal conductivity of AA7075 and stainless steel as a function of temperature in Kelvin were obtained by empirical polynomial fit to the data from the literature. The various empirical equations for AA7075 extracted from Mitchell (2004) are shown below:

$$E_1 = 8.25\text{E}04 - 39.08\text{T}\ [MPa] \tag{3.1}$$

$$v_1 = 3.25E\text{-}01 + 1.35E\text{-}05T + 3.89E\text{-}08T^2 \quad (3.2)$$

$$k_1 = 1000*(8.52E\text{-}02 + 1.37e\text{-}04T - 5.15E\text{-}08T^2)\ [W/mmK] \quad (3.3)$$

where T is the average temperature of blank and die. Similarly, other data for temperature-dependent properties such as hardness, yield strength and Meyer's exponent *m* was also obtained by polynomial fitting from the researcher's lab material data, as follows:

$$H_1 = 1.21E03 / (1 + \exp(-8.90 + 1.99E\text{-}02T))^{(1 / 1.85)}\ [MPa] \quad (3.4)$$

$$S_y = 2.65E02 - 3.57T + 1.50E\text{-}04T^2\ [MPa] \quad (3.5)$$

$$m_1 = 2 + (2.64E01 / (1 + \exp(-8.67 + 1.84E\text{-}02T))^{(1 / 1.46))} \quad (3.6)$$

The various empirical equations for stainless steel extracted from INCO (1963) are shown below:

$$E_2 = 2.00E05 + 11.78T - 8.72E\text{-}02T^2\ [MPa] \quad (3.7)$$

$$v_2 = 3.31E\text{-}01 - 5.17E\text{-}04T + 8.26E\text{-}07T^2 \quad (3.8)$$

$$k_2 = 6.31 + 2.72E\text{-}02T - 7.00E06T^2\ [W/mmK] \quad (3.9)$$

### 3.5 Experimental Set-up for Heat Transfer Experiments

Experimental setup used to measure TCR area is illustrated in Figure 3.6. The apparatus comprised of a 115 kN load capacity MTS 810 computer-controlled servo-hydraulic mechanical test system with two axially aligned actuators. This system was interfaced with Interlaken control and data acquisition system to continuously record applied and actuator displacement values. Two cylinder-shaped flat stainless steel dies were mounted on the two actuators for AA7075 blank clamping and loading. Also, a portable temperature-controlled

environmental chamber (Nabertherm model LT15/11) was placed in close proximity to the mechanical test system.

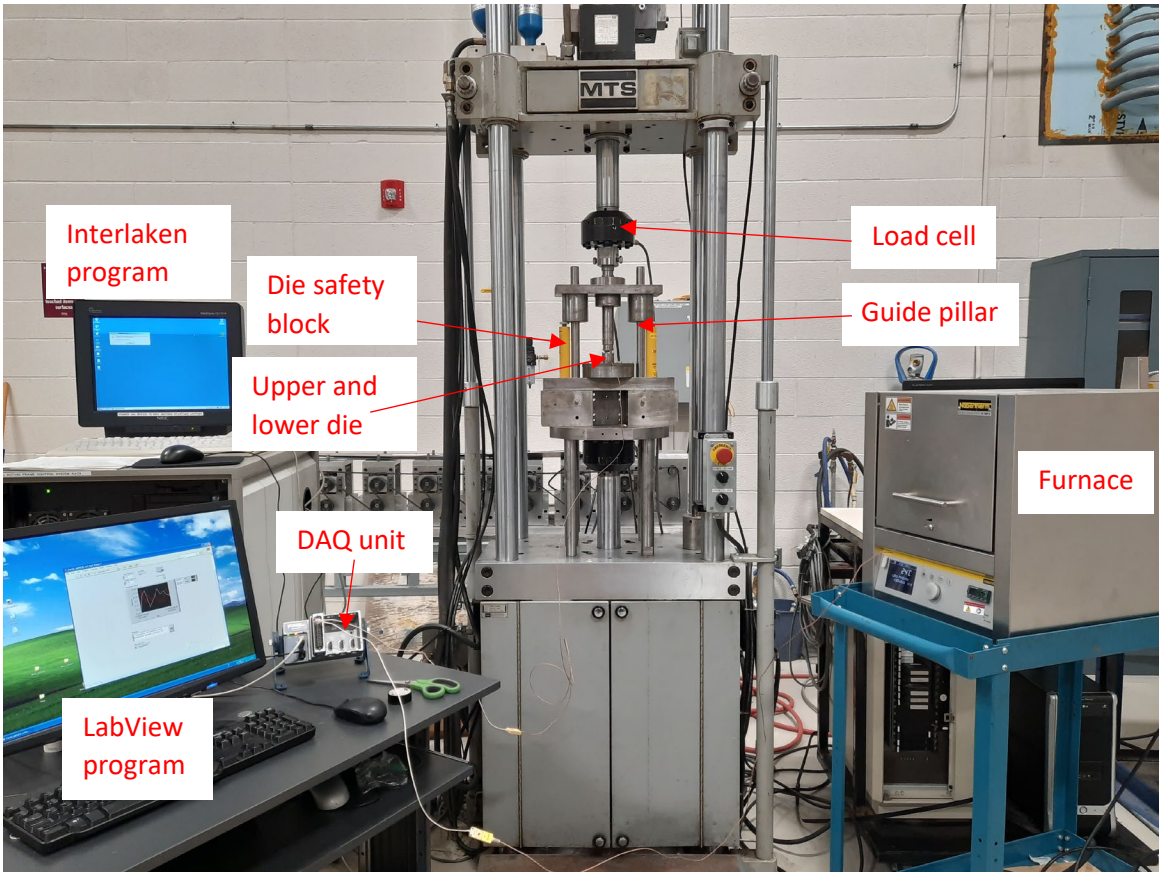


Figure 3. 6 General view of mechanical test system for specimen loading experiments.

Additionally, a portable data acquisition device for temperature (National Instrument NI-9213) and associated software (LabView) were used. The former was connected to a set of thermocouples embedded in the die and AA7075 blank, while the latter was connected to a portable laptop computer that was used to store data during the test.

A schematic sketch of planar die quenching tool is shown in Figure 3.7. The upper and lower dies were made of stainless steel 316SS with a diameter of 19 mm and a height of 9.36 mm. A 10 mm diameter button-like step on each die worked as a punch to indent the center of the AA7075 blank.

These dies were fitted into an extended steel holder mounted on the mechanical testing system. AA7075-F aluminum disk of 24 mm diameter and 2 mm original thickness (referred to as blank) were laser cut from a large AA7075-F aluminum sheet of 2 mm thickness. Overall, the test system was capable of applying a maximum normal load of 115 kN corresponding to a maximum pressure of 1464 MPa over a circular patch of diameter 10 mm.

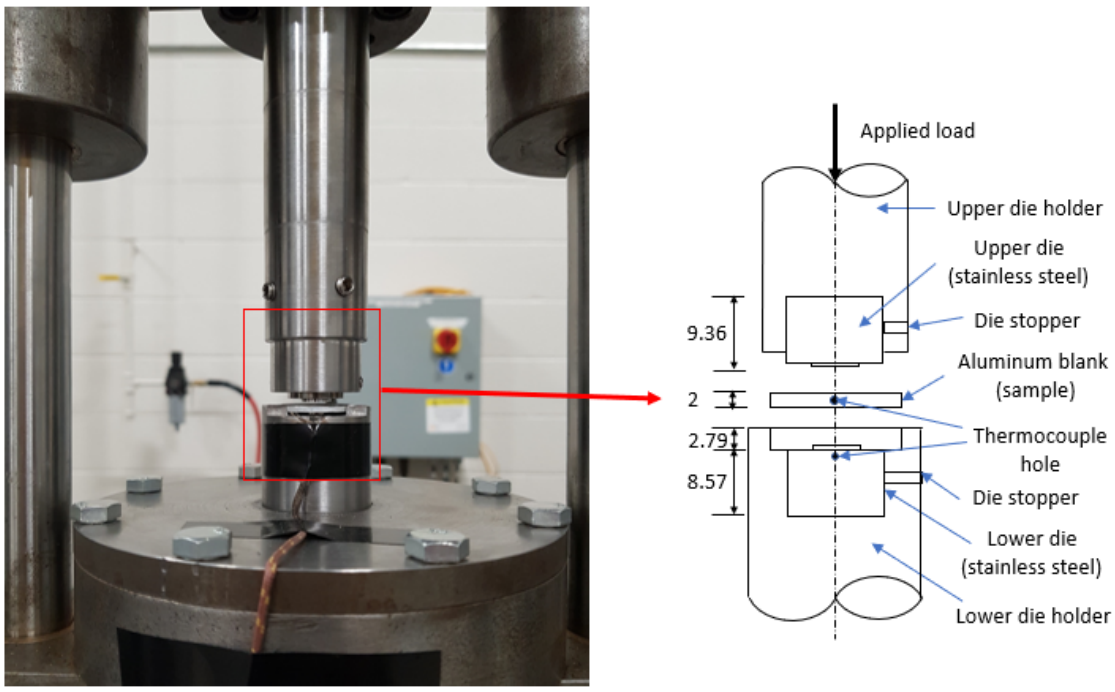


Figure 3. 7 Planar die pressing and quenching tool.

The details of upper and lower dies, and blank are illustrated in Fig. 3.8. Only lower die had a thermocouple hole through its center, and the hole was cut by using EDM. For each AA7075 blank, 1.19 mm in diameter thermocouple hole was precisely drilled from the edge to its center with the centre of the hole at mid-thickness. In Figure 3.9, the details of upper and lower die holders are shown. They were designed to ensure that upper and lower dies could be easily removed for polishing.

The planar dies were designed to perform careful measurements of temperature within the lower die using an embedded contact thermocouple (Fig. 3.10(a)). A 0.5 mm diameter glass sheathed thermocouple type K was placed 2 mm below the die surface to record the temperature of the die and calculate the heat flux. Similarly, a hole was drilled at the edge of the blank to its center to locate the thermocouple (Fig. 3.10(b)).

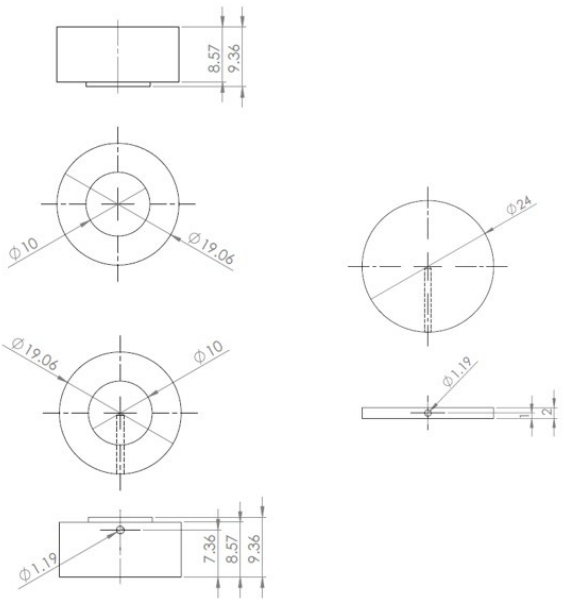


Figure 3. 8 Schemetic view of (left) upper and lower dies and (right) blank (all dimensions are in mm).

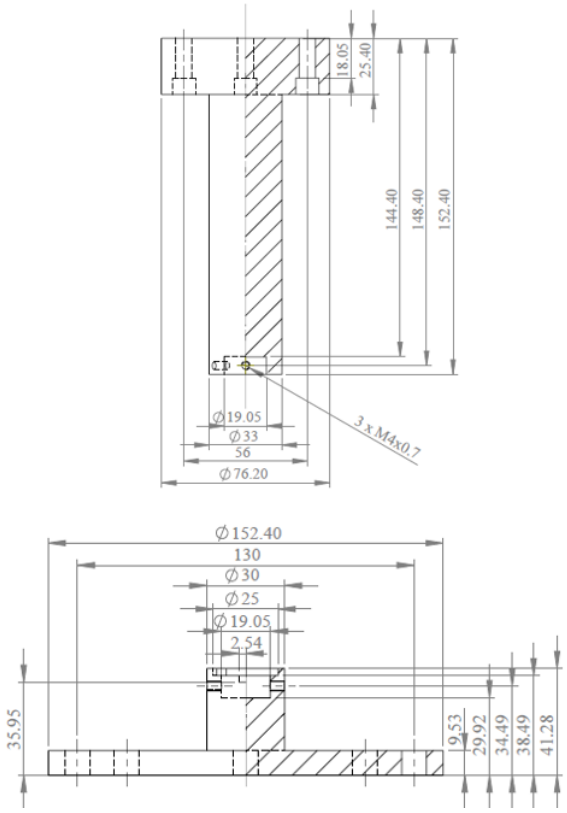


Figure 3. 9 Schemetic view of upper and lower die holders (all dimensions are in mm).

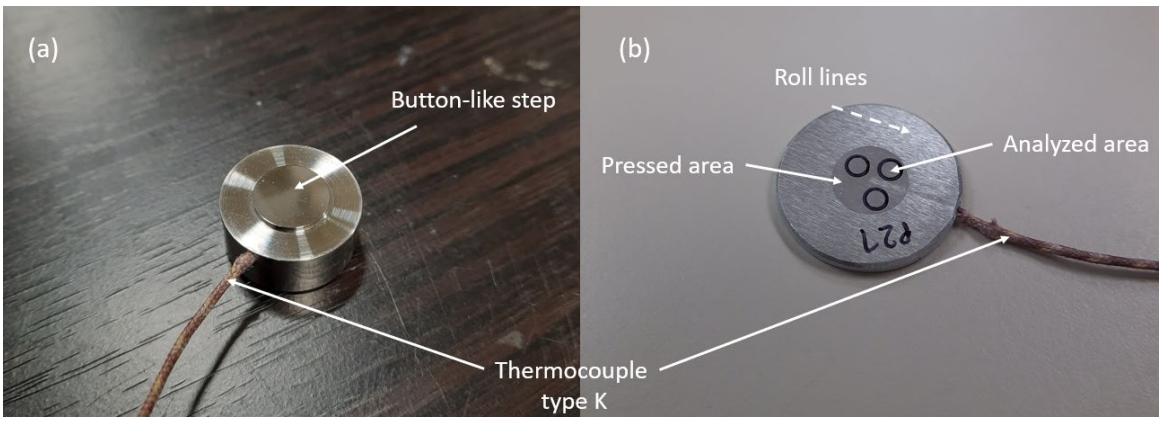


Figure 3. 10 Thermocouple embedded at (a) 2 mm below the lower die surface, and (b) at the center of the AA7075 blank.

## 3.6 Experimental Methodology

### 3.6.1 Component Assembly and Experimental Procedure for Heat Transfer Experiments

In preparation for heat conduction experiments, mechanical test system was first fitted with loading arms (i.e., die holders). Also, contacting surfaces of upper and lower dies were cleaned, and dies inserted into the respective die holders as shown earlier in Fig. 3.9. A 0.5 mm diameter glass-sheathed K type thermocouple was inserted into the lower die. Another type K thermocouple was inserted into the 24 mm diameter blank from the periphery of the blank at mid-thickness to the centre of the blank by machining a hole slightly larger than the thermocouple outer diameter. The tips of both thermocouples were coated with 120-2 silicone-oil based thermal joint compound made by Wakefield Solutions to allow for better contact and accurate measurements of temperatures of the die and blank during the experiments.

For the final step prior to heat transfer experiments, both thermocouples were connected to a NI 9213 data acquisition system (DAQ) made by National Instruments. The DAQ with a programmable LabView software were used to acquire the temperature data and transfer them to a PC for later plotting. The data acquisition rate used for recording the temperature data was 6.67 Hz and chosen as the maximum rate possible for the data acquisition system. All temperature measurements were taken under transient temperature conditions. Meanwhile, the target load was controlled, and load-time history was recorded by built-in load cell mounted on the actuator and integrated with the test control and data

acquisition unit on the mechanical test system. The data acquisition rate for recording the load data was 500 Hz.

In term of experimental procedure for performing heat conduction experiments, the AA7075 blank with the inserted thermocouple was first heated in a separate Nabertherm LT15/11 environmental chamber to 450°C for about 5-10 minutes. No observable oxidation of the blank was noted as the heating duration quite short. The environmental chamber was positioned near the mechanical test system for easy manual transfer of the blank (with tongs) to the press, and specifically, on to the die surface, with minimum heat loss to the surrounding by convection and radiation. Upon reaching the target temperature in the environmental chamber, the chamber door was opened for the transfer process to take place. The hot AA7075 blanks were subjected to different loads in three separate tests: 6.7 kN (Test 1), 11.1 kN (Test 2) and 15.6 kN (Test 3) as per the pre-set loading spectra on the test control system.

The applied load from the load cell, actuator displacement from built-in LVDT, and temperatures of lower die and AA7075 blank from the two thermocouples, all as a function of time, were continuously recorded during test. This data was later used in conjunction with Beck's inverse heat conduction method (details to be presented later) to predict interfacial heat flux, and surface temperatures of blank and die, and subsequently, to obtain TCR area as a function of test temperature and applied load. The 'experimental' TCR area values were later used to compare similar data predicted by the proposed mechanistic models as presented in the next chapter. It is to be noted that, TCR area is often reported in the literature as a function of contact pressure. Therefore, in the present work, the load was

converted to pressure by dividing with the nominal contact area ($A = \pi r^2 = \pi(5.0\ mm)^2 = 78.54\ mm^2$). The corresponding pressure for each test were: 85 MPa (Test 1), 141 MPa (Test 2) and 199 MPa (Test 3).

For the mechanistic approach, the above experimental die setup and its load capacity were sufficient for high temperature and large load application to analyze the nature of elastoplastic asperity flattening process on the AA7075 blank surfaces in contact with stainless steel dies. Since the asperities on the surface were not of the same height and deformed individually, depending on the applied pressure, the deformation of asperities may be elastic, elastoplastic and fully plastic. The changes in surface topography were assessed after pressing. Subsequently, a relation between asperity deformation and the transient TCR area calculation could be obtained.

### 3.6.2 Experimental TCR Area Estimation Method

The details of Beck's sequential function specification method for estimating TCR area during heat transfer experiments are provided below. This method which is commonly used by hot stamping researchers, inversely predicts the interfacial surface heat flux and die surface temperature from measured temperature within the die ($T_{d,meas}$). In brief, the optimal TCR area values were obtained in two steps:

i. A non-linear semi-infinite heat conduction problem was solved in the die (by using Beck's method). From this, one could predict interfacial heat flux ($q''$), die surface temperature ($T_{d,surf}$) (refer to Figure 3.11).

ii. Blank surface temperature ($T_{b,surf}$)) was assumed to be the same as the measured blank temperature ($T_{b,meas}$) in the middle of blank where the thermocouple is located.

Note that, due to small Biot number ($Bi=hl/k<0.1$) in which the hot AA7075 blank has high thermal conductivity (e.g. k=146.7 W/mK and h=666 W/m$^2$K at 300°C) and small volume to area ratio ($l$ =1 mm), lumped capacitance assumption is applicable to the hot AA7075 blank in the present work.

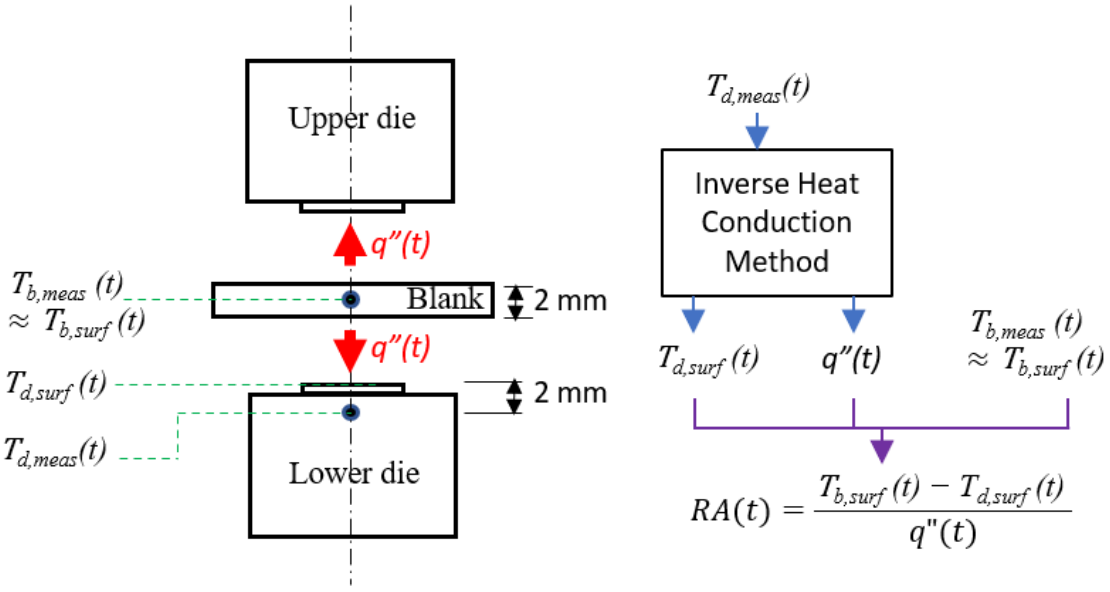


Figure 3. 11 Schematic model of TCR area estimation.

Knowing the interfacial heat flux ($q$"), surface temperatures of blank ($T_{b,surf}$) and die ($T_{d,surf}$), TCR area as a function of time ($t$) could be estimated from Newton's law of cooling as follows:

$$RA(t) = \frac{T_{b,surf}(t) - T_{d,surf}(t)}{q"(t)} \quad (3.10)$$

In Beck's method, the interfacial surface heat flux $(q"(t))$ is predicted by first minimizing the difference between the calculated $(T_{calc})$ and measured temperatures $(T_{d,meas})$ at one or several locations within the die, in an iterative manner. Note that calculated temperature $(T_{calc})$ could be obtained by a partial differential equation solver. The interfacial heat flux is expressed as:

$$q"(t) = \frac{\sum_{i=1}^{TS}\sum_{j=1}^{J}\left(T_{d,meas_j}(t+i-1) - T_{calc_j}(t+i-1)|q"(t)=\cdots 0\right)\phi_{ji}}{\sum_{i=1}^{TS}\sum_{j=1}^{J}{\phi_{ji}}^2} \quad (3.11)$$

$$\text{where sensitivity coefficient, } \phi_{ji} = \frac{\partial T_{ji}}{\partial q_{ji}} \quad (3.12)$$

where *J* and *TS* are the number of thermocouples and number of future time steps, respectively. As for TCR area estimation in this work, *J=1* and *TS=3* were chosen based on several parametric studies to find the optimum values of TCR area. The same *TS* value was used by Abdulhay et al., (2011) and Caron et al. (2013) in their work.

### 3.7 Experimental Results

Experimental program consisted of determining the response from three load input data referred to as Tests 1 – 3 earlier. Each test was carried out by using new specimen and repeating the test at least three times.

#### 3.7.1 Thermo-mechanical results

Figure 3.12 presents the experimentally obtained blank cooling and die heating curves during heat transfer experiments from Test 3. Initially, an AA7075 blank was heated from

room temperature to 450°C then immediately transferred from furnace to the die. The transfer time was about 4 sec, and blank placement on the lower die took another 3 seconds. It is clearly seen that the blank temperature gradually decreased in two stages, one involving transfer of the blank through ambient air and the other involving placement of the hot blank on cold (room temperature) die.

The actual clamping process began at a time of 7 sec after opening the furnace door to remove the blank. At this stage, the hot blank was in contact between upper and lower dies, and the blank temperature dropped rapidly. Simultaneously, the load increased to the target value and the surface asperities started to deform and stopped deforming when the target load was reached. This process took about 0.3 seconds. Note that there is a wiggle in the loading (black) curve near the peak load which is actually an overshoot due to the control system transition from displacement control to load control. Subsequently, the blank temperature dropped more gradually to room temperature. On the other hand, the temperature of the die increased only slightly during the placement phase but more abruptly during the clamping phase. Then, at a time of about 7.5 sec, the die temperature began to decrease gradually towards the room temperature at the end of the heat transfer experiment. As shown in Figure 3.12, rate of cooling of the AA7075 blank past the peak load is considerably higher compared to the die.

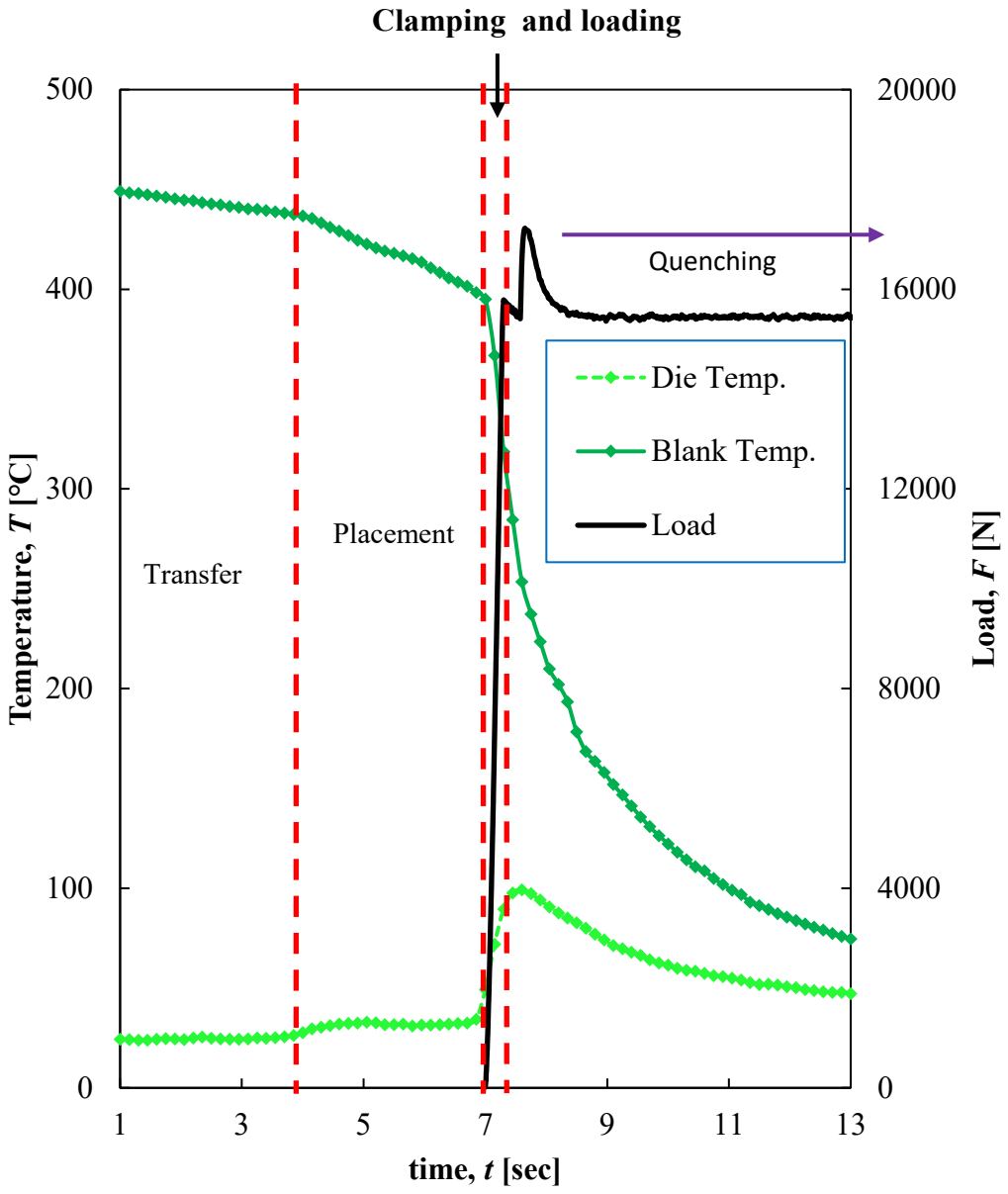


Figure 3. 12 Blank cooling and die heating temperature curves with applied load evolution during heat transfer experiment (Test 3).

#### 3.7.1.1 Effect of Contact Pressure on Cooling Rate

Based on previous studies, contact pressure and temperature greatly affect the thermal contact resistance in hot stamping process (Merklein et al., 2016). This phenomenon could only be explained by physical deformation of asperities during the clamping and loading stages.

As expected, the contact area that determines the heat flow from hot blank to cold die becomes larger as the pressure increases. Figure 3.13 presents all blank cooling and die heating curves for Tests 1-3. At the end of first 7 seconds, all blank cooling curves lie close to each other. However, the curves diverge soon after due to different cooling rates. As expected, test with the highest load, i.e., Test 3, had the highest cooling rate. The cooling rates for Tests 1, 2 and 3 were 157 °C/s, 200 °C/s and 276 °C/s, respectively. Finally, the three curves merge into each other at about 13 seconds.

#### 3.7.1.2 Effect of Contact Pressure on Heat Flux and IHTC

In order to understand the characteristics of TCR area (and IHTC) at different loads, the pattern of heat flux was analyzed first. This was due to the fact that TCR area is a function of interfacial heat flux, and the difference between blank and die surface temperatures. Figure 3.14 presents the predicted heat flux at the contact surface from Beck's method for 3 separate AA7075 sheet samples heated to 450°C and then rapidly transferred to the surface of the stainless steel plate (i.e., die) for clamping at three different clamping loads. The heat flux is presented as a function of temperature difference (of blank

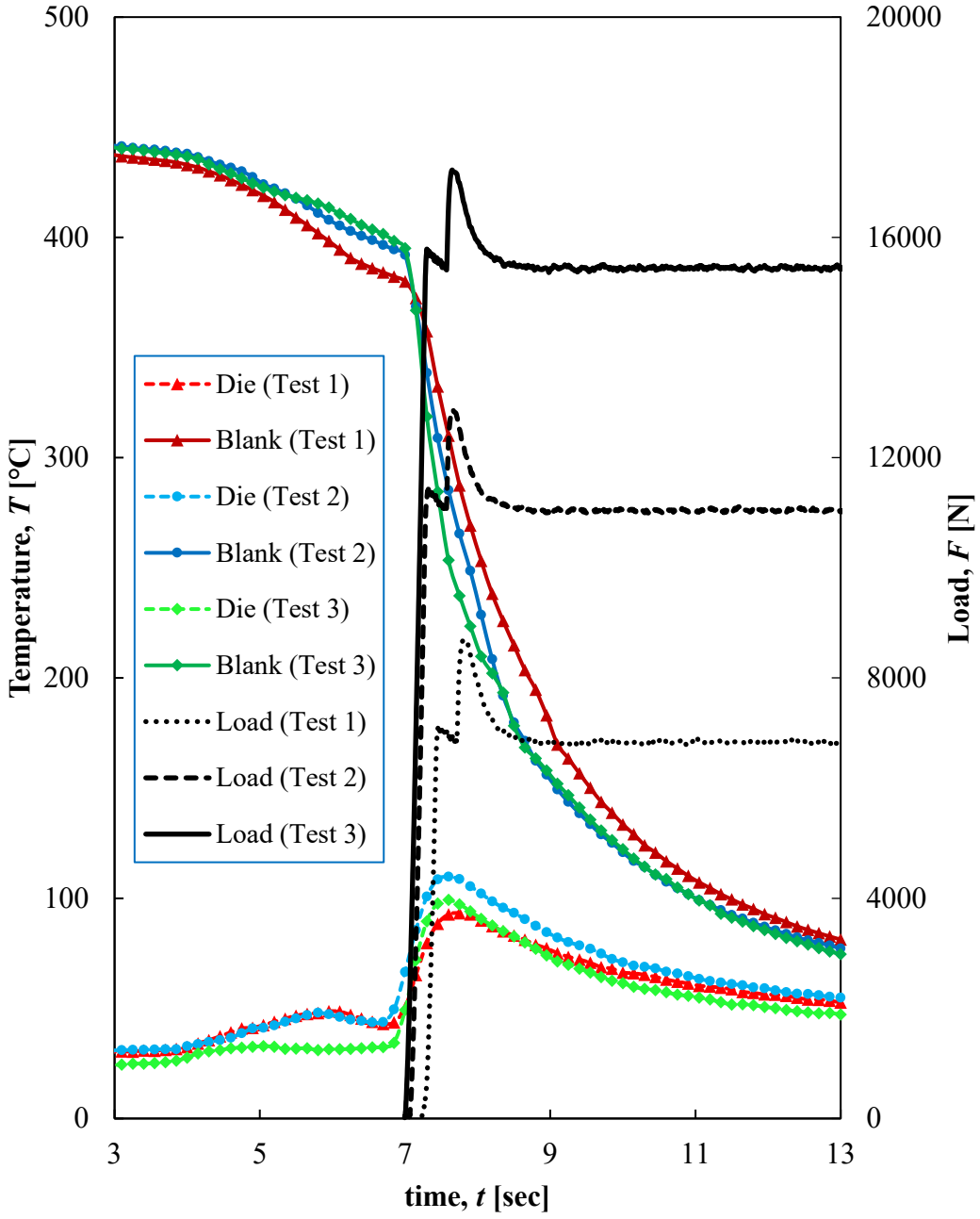


Figure 3. 13 Blank cooling and die heating curves for different loads in die quenching experiment.

and die) according to the work of Caron et al. (2013) but in contrast to the work of Chang et al. (2017) where the latter presented heat flux versus blank temperature and not the temperature difference. The reasoning behind using temperature difference is to account for both the blank and die surface temperatures as the main contributors to the calculation of the heat flux.

It is to be noted that heat transfer process from start to finish occurs from the right to the left in the curves shown in Figure 3.14. In general, we can see that there are two waves or fluctuations in heat flux during the heat transfer process. The smaller first fluctuation occurs during blank placement. There is a slight heat transfer from the hot blank to the cold die, which increases the heat flux. The drastic increase occurs when the blank clamping process takes place. As soon as the load ramps to its target, the asperities deform and real contact area evolves rapidly, and consequently the heat flux also increases abruptly. Upon reaching its target load, the asperities stop deforming, and the heat flux gradually decreases.

As shown in Figure 3.14, the peak of heat flux for Tests 1, 2 and 3 are 500 $kW/m^2$, 673 $kW/m^2$ and 703 $kW/m^2$ respectively. It is obvious that the heat flux curve for Test 1 is rather small compared to the other two tests, likely due to heat loss during placement stage. Similar trend is also apparent in TCR area curves in Fig. 3.15 where there are two characteristic waves. The first is during blank placement on the lower die and the second is from the clamping stage when much heat is transferred to the cold dies. At the same time, the contact area enlarges as the asperities deform, thus enhancing the heat flow and TCR area ramps to its lowest value. When the deformation stops, the remaining flow of heat

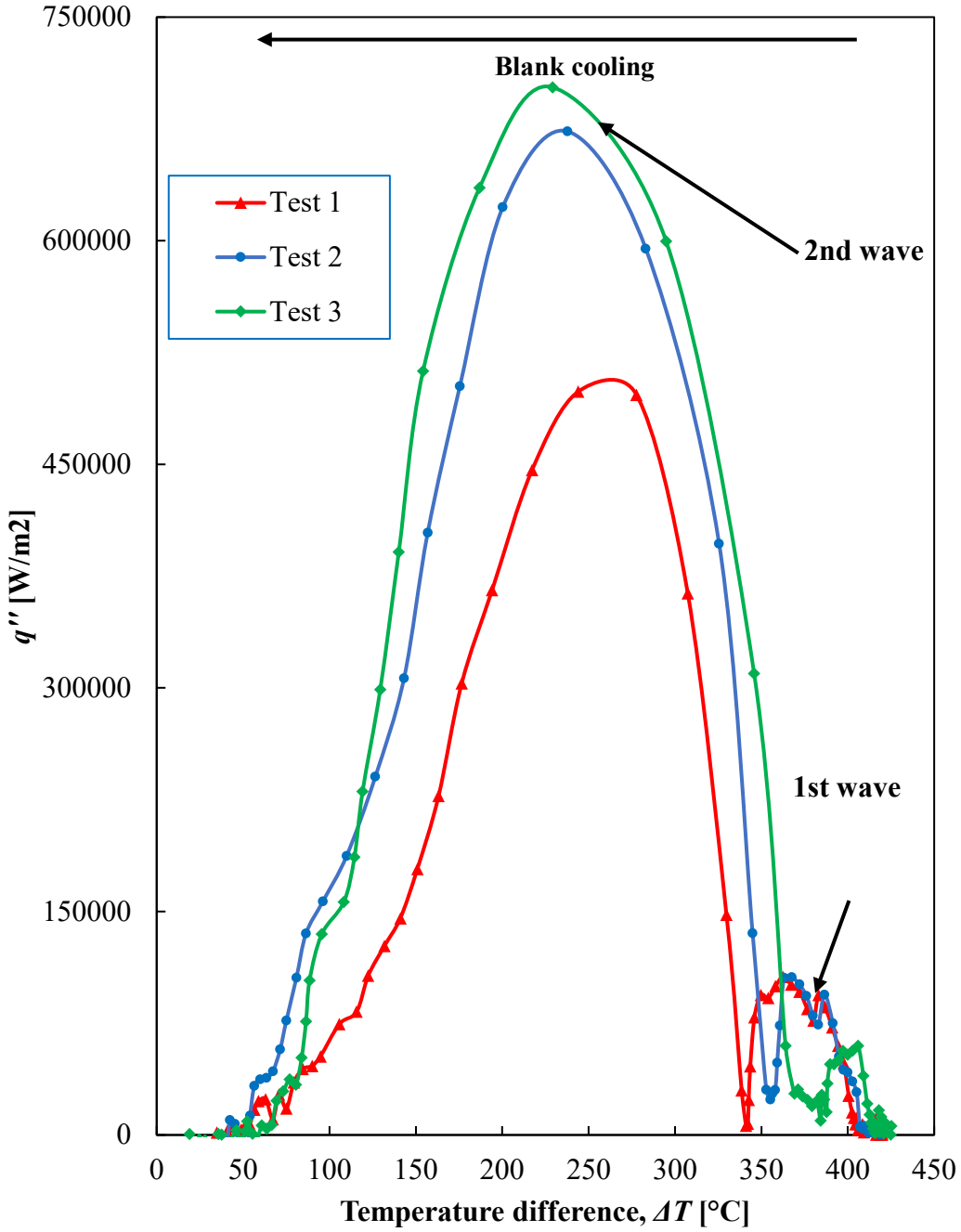


Figure 3. 14 Predicted heat fluxes for different loads in heat transfer experiment.

from the hot blank is gradually reduced leading to an increase in TCR area. The lowest TCR area values are 487 $mm^2K/W$, 322 $mm^2K/W$ and 294 $mm^2K/W$ for Tests 1, 2 and 3, respectively.

### 3.7.2 Load versus Indentation Depth Relationship

The displacement (or indentation depth) measurements for obtaining load versus indentation relationship, at the beginning of the study, were received directly from the built-in Linear Variable Differential Transducer (LVDT) with the mechanical test system. However, the values of indentation depth seemed unreasonable compared to the post-loading change in surface roughness and overall thickness reduction in the compressed region of the specimen. For example, the change of surface roughness for Test 1 was 0.00021 mm but the LVDT provided values of 0.012 mm.

This large discrepancy, after much investigation, was attributed to the lack of adequate rigidity in the load train of the mechanical test system, i.e., the elastic deflection or clearance in the members making up the load-train was rather large. Therefore, it was decided to use the post-test flattened region of the specimen at each peak load as the corresponding indentation depth or displacement. Since these measurements were microscopic and had to be post-test, it was assumed that the elastic recovery of the asperity was relatively small compared to the plastic deformation and could be disregarded.

The indentation depth for each load was then determined using the average of three repeat tests. For instance, the indentation depth for peak load in Test 1 was equal to the difference between the average initial RMS roughness value and the average RMS

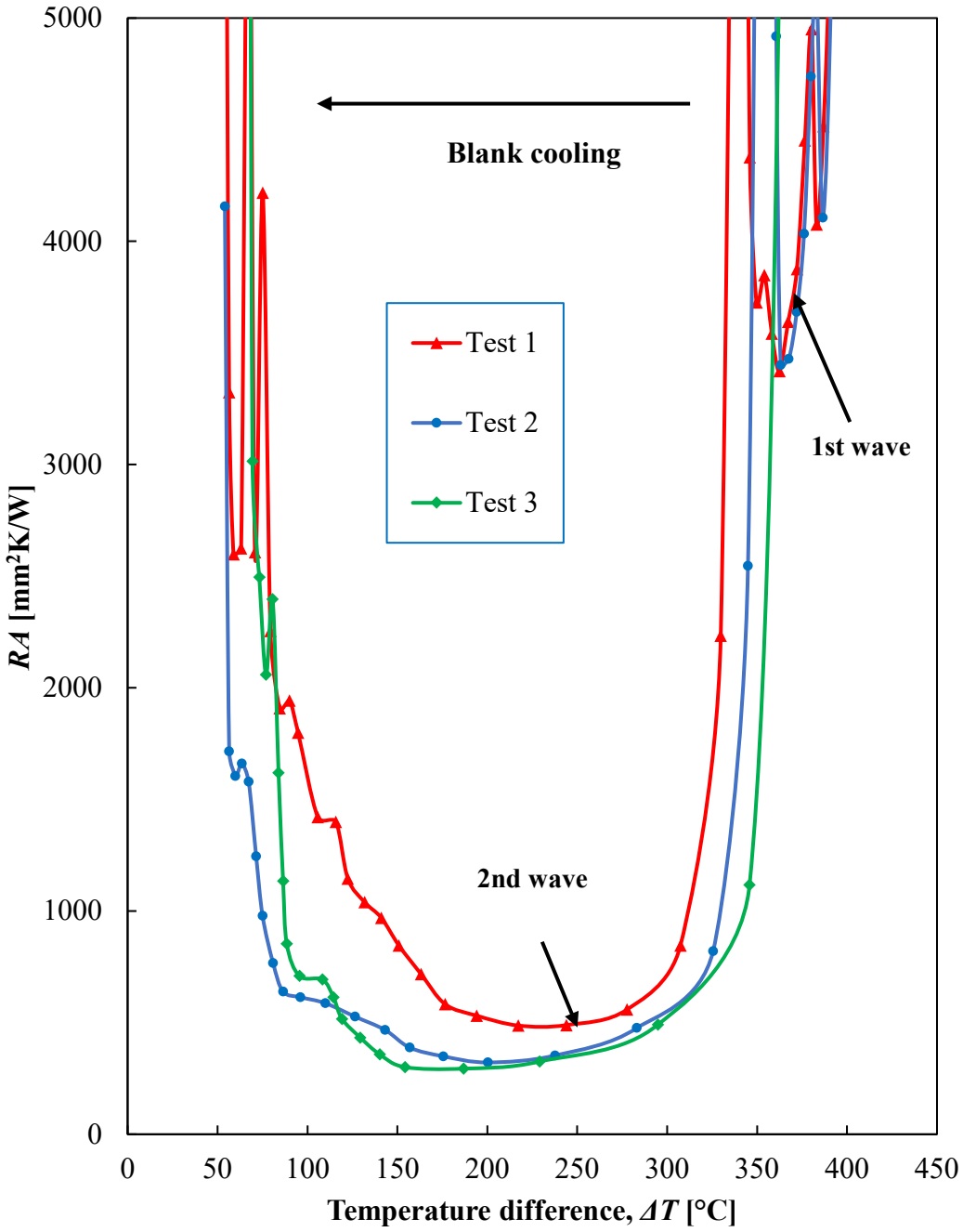


Figure 3. 15 Calculated TCR area during die quenching experiment.

roughness value for Test 1. Table 3.1 shows the RMS roughness for Tests 1, 2 and 3 from the post-test thickness measurements. The corresponding indentation depth at each load was calculated and plotted in Figure 3.16. It was found that the indentation depth increased concavely (upwards) as the contact load increased.

As the indentation depth approached the asperity height, i.e., 0.68 μm, the dz-F graph reached saturation in displacement. The first (6700 N), second (11100 N), and third (15600 N) loading tests resulted in average indentation depths of 0.21 μm, 0.30 μm, and 0.35 μm, with standard deviations of ± 1.82E-05 μm, ± 3.84E-05 μm, and ± 4.51E-05 μm respectively. This experimental indentation depth-load data is used in the next chapter to compare with the predictions from the proposed mechanistic model.

### 3.7.3 Real Contact Area versus Load Relationship

This sub-section presents an experimentally obtained real contact area corresponding to the three peak loads as applied in Tests 1-3. The real contact area was measured post-test from SEM images of the flattened asperities using ImageJ software (refer to Fig. 3.17). The yellow and dark contours refer to flattened and unflattened asperities, respectively. The real contact area from SEM is tabulated in Table 3.2. The total real contact area was calculated as the ratio of the SEM-based real contact area to the SEM image area multiplied by the nominal contact area (78.54 $mm^2$). Note that the SEM image area here is was 255 x 173 $\mu m^2$.

Table 3. 1 Determination of indentation depth after blank pressing at different loads.

| Test# | Max Load [N] | RMS Roughness [mm] | | | | Indentation depth [mm] |
|---|---|---|---|---|---|---|
| | | Meas. 1 | Meas. 2 | Meas. 3 | Average | |
| initial | 0 | 0.000573 | 0.000672 | 0.000786 | 0.000677 | 0.000000 |
| 1 | 6700 | 0.000452 | 0.000487 | 0.000461 | 0.000467 | 0.000210 |
| 2 | 11100 | 0.000407 | 0.000334 | 0.000391 | 0.000377 | 0.000300 |
| 3 | 15600 | 0.000357 | 0.000276 | 0.000351 | 0.000328 | 0.000349 |

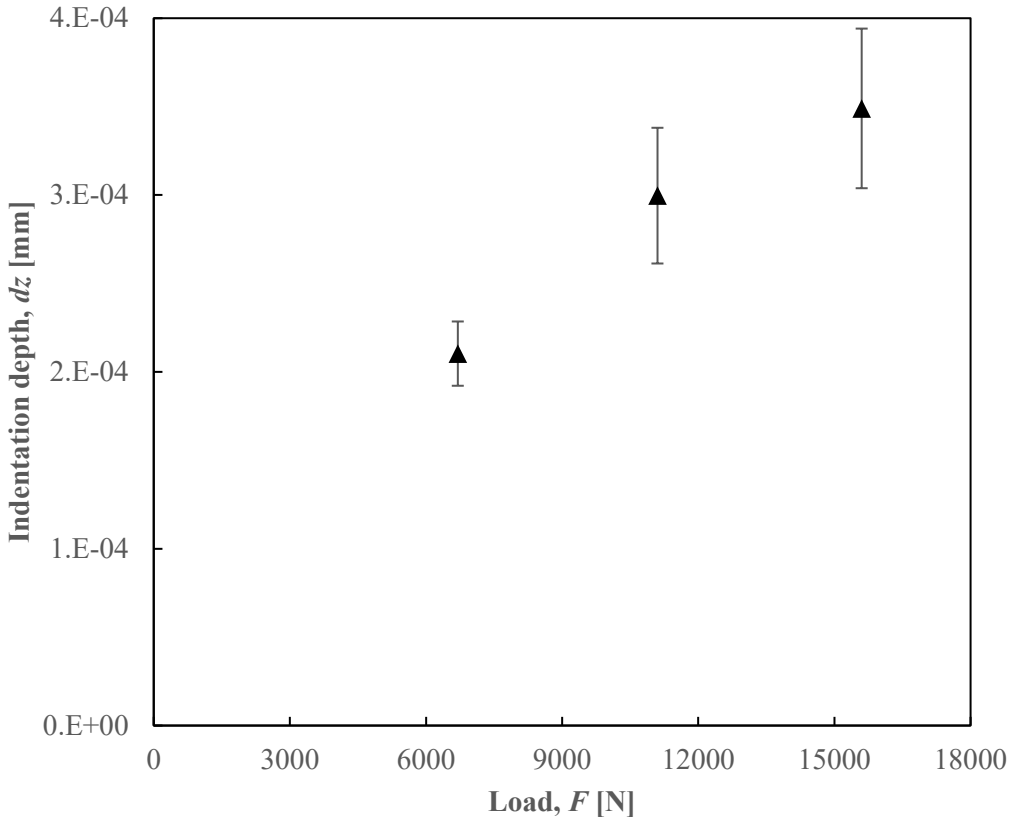


Figure 3. 16 Indentation depth as a function of load for three different tests.

Table 3. 2 Real contact area based on SEM image.

| Test# | Max Load [N] | Percentage real contact area/nominal contact area [%] | | | | Total real contact area [$mm^2$] |
|---|---|---|---|---|---|---|
| | | Meas. 1 | Meas. 2 | Meas. 3 | Average | |
| 1 | 6700 | 10.32 | 9.12 | 12.20 | 10.55 | 6.72 |
| 2 | 11100 | 16.35 | 18.58 | 22.57 | 19.17 | 12.54 |
| 3 | 15600 | 20.12 | 23.61 | 21.48 | 21.74 | 15.72 |

The corresponding real contact area at each load is calculated and plotted in Figure 3.18. The results show that the real contact area increases concavely as the contact load is increased. The first (6700 N), second (11100 N), and third (15600 N) loading tests resulted in average real contact areas of 6.72 $mm^2$, 12.54 $mm^2$, and 15.72 $mm^2$, with standard deviations of ± 1.22 $mm^2$, ± 2.48 $mm^2$, and ± 1.38 $mm^2$, respectively. This experimental real contact area-load data is used in the next chapter for comparison with the predictions from the proposed mechanistic model.

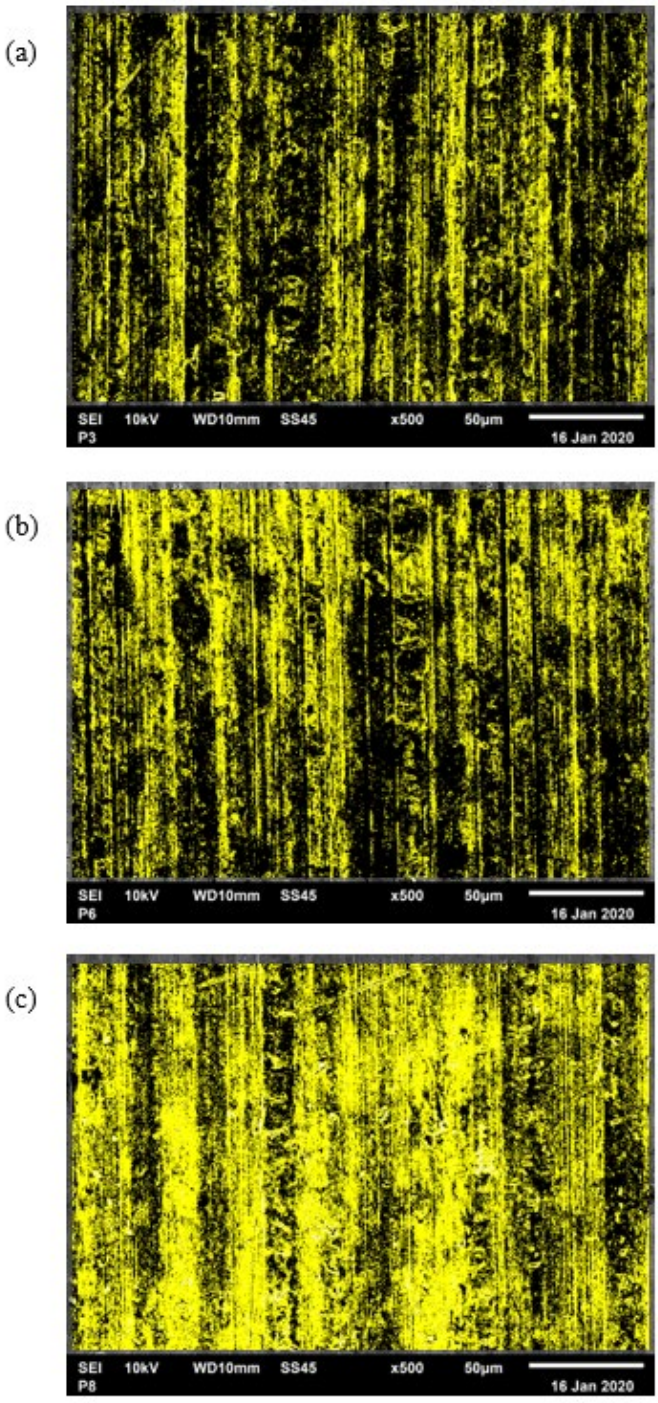


Figure 3. 17 SEM images of contacted area (yellow) and uncontacted area (dark) at three different tests; (a) 6700 N, (b) 11100 N, and (c) 15600 N.

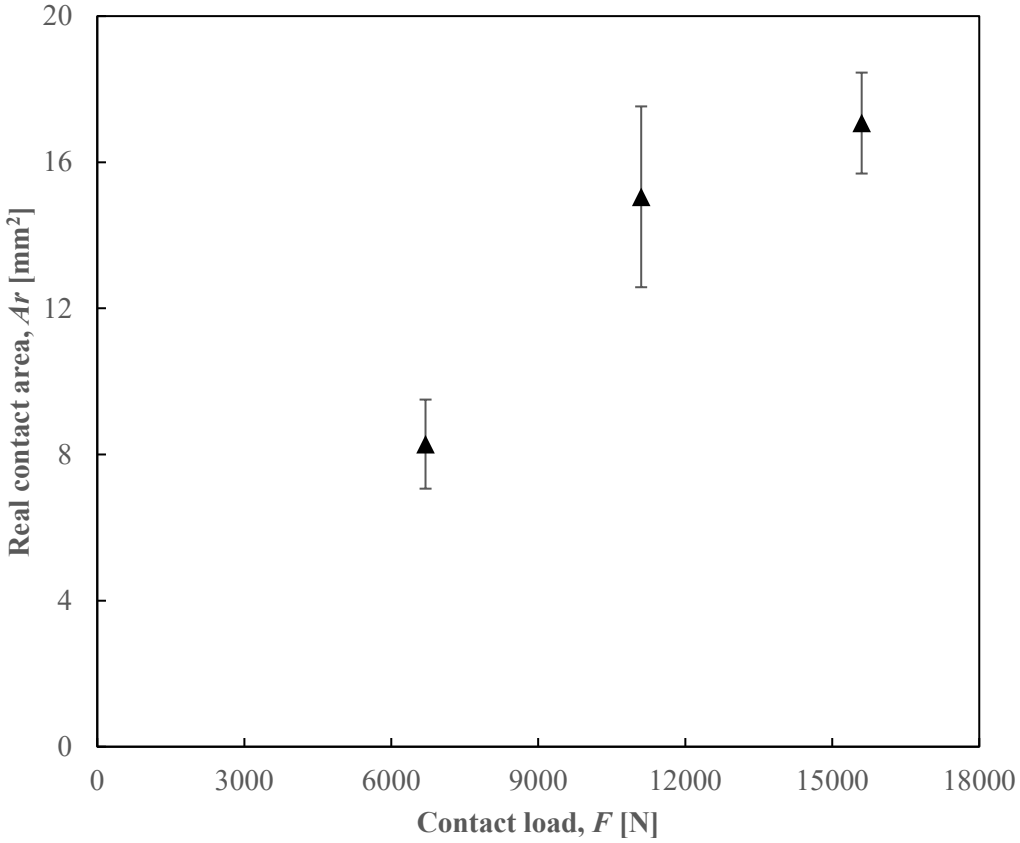


Figure 3. 18 Real contact area as a function of load for three different tests.

### 3.7.4 TCR Area versus Load Relationship

TCR area was first obtained as a function of time during the loading stage. Similarly, the force from the load cell (i.e., load) versus time data during loading of the AA7075 blank was extracted from the raw data. Finally, the TCR area was correlated to load from the above data. The process was repeated for each loading history of Tests 1-3 and results are summarized in Table 3.3.

Table 3. 3 Results from experiments and Beck's method.

| time | Td,meas [°C] | Tb,surf [°C] | Td,surf [°C] | q" [W/m2] | RA [mm$^2$K/W] | F [N] |
|---|---|---|---|---|---|---|
| Test 1 | 47.11 | 332.41 | 88.43 | 498754 | 489.17 | 7070 |
| Test 2 | 47.60 | 338.51 | 100.74 | 673348 | 353.11 | 11289 |
| Test 3 | 35.83 | 318.68 | 89.55 | 702941 | 325.96 | 15788 |

The above data also was plotted in Fig. 3.19 for comparison. It is clear that all of the data forms a single curve in which the TCR area decreases with load increment. The first,

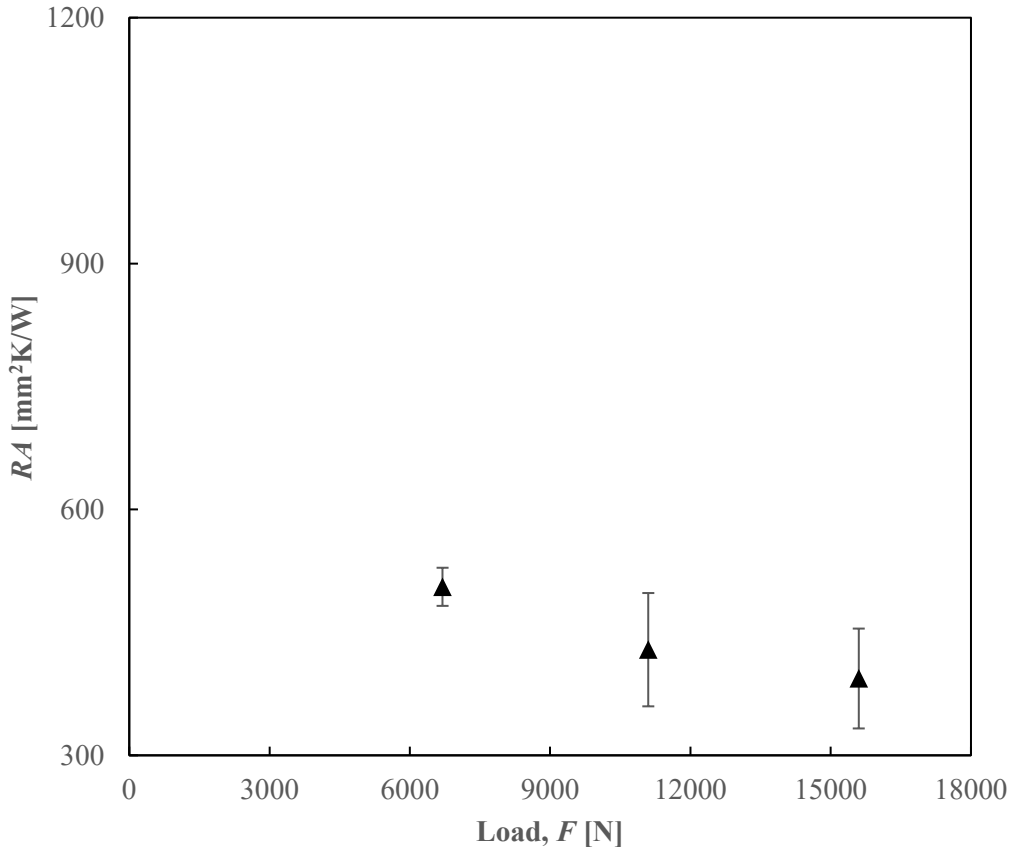


Figure 3. 19 TCR area as a function of load for three different tests.

second, and third data have average TCR area values of 489.17 $mm^2K/W$, 353.11 $mm^2K/W$, and 325.96 $mm^2K/W$, with standard deviations of ± 23.26 $mm^2K/W$, ± 69.12 $mm^2K/W$, and ± 60.92 $mm^2K/W$, respectively. This data will be used later for comparison with TCR area versus load curves from the modeling work.

### 3.7.5 Asperities Distribution from Blank Surface Profile

This sub-section provides further useful experimental data for modeling work presented in the next chapter. The number of asperities is based on real blank surface profile. Based on Figure 3.4, there are about 23 asperities above the mean line or datum (z=0 μm) per 1000 μm of horizontal distance. So, there are approximately 46 asperities per 1000 μm in total when considering peaks and valleys of both surfaces of AA7075 test specimen. For this study, only asperities above z=0.349 μm, i.e., 15 asperities per 1000 μm are considered. This is related to the range of the experimental indentation depths values achieved (refer to sub-section 3.6.2). Thus, there are 150 asperities considered for a sample length of 10 mm that make up the total nominal area being pressed. These 150 asperities represent 32.6 percent of total asperities and will be referred to later as maximum ratio of SEM real contact area to SEM image area of 0.319 (refer to Table 3.3) for Test 3 conducted at an applied pressure of 199 MPa.

According to Bowden and Tabor, a value of 0.25% is same as a fractional contact area of 0.0025 (at a pressure of 2.3 MPa) whereas the present fractional contact area value is 0.319 occurs at a pressure of 199 MPa. Since the present pressure is 82.6 times higher than the Bowder and Tabor's, if one multiplies 0.0025 by 82.6, one obtains a fractional contact area of 0.2065 which is reasonably close to 0.319 obtained in the present study. It

should also be noted that, unlike the Bowden and Tabor's work, the present work involves high temperature plastic deformation of asperities, so the flattening of asperities as well as fractional contact area would be significantly higher than the room temperature value of 0.2065.

For the modeling purposes, the asperities distribution is classified into two categories: SCF and MCF contact models, which are defined as single uniform asperity level and multi-asperity level (150 asperities) models respectively. In this study, MCF contact model has three asperity levels:

i. Level 1 (height, $0.6<h_1\leq0.67$ μm): $n_1$ asperities
ii. Level 2 (height, $0.4<h_2\leq0.6$ μm): $n_2$ asperities
iii. Level 3 (height, $0.349<h_3\leq0.4$ μm): $n_3$ asperities

where the total sum of numbers of asperities at the three levels is $n_1 + n_2 + n_3 = 150$ asperities.

### 3.8 Summary

Experimental program to characterize initial (undeformed) sheet asperities and elevated temperature asperity flattening and evolution of real contact area as well as determination of heat flux and TCR area were conducted using a well-instrumented miniature die-set mounted on a well-controlled mechanical test system and other associated equipment. This data will be utilized in Chapter 5 for comparison and validation of similar results from proposed mechanistic models presented in Chapter 4. Specifically, load versus macroscopic indentation depth data, load versus real contact area data, as well as TCR area versus applied load data will be used to compare with similar results from mechanistic models.

# Chapter 4

## Analytical Modeling of Solid to Solid Elastic and Plastic Contact and Heat Transfer Across the Contact Surface under Normal Loading

---

This chapter presents the development of analytical models of elastoplastic deformation of single and multiple cylindrical asperities on one surface contacting another rigid, flat and smooth surface under normal load. The contact and normal loading of two surfaces causes flattening of the cylindrical asperities and thus changes in the real contact area between the two surfaces resulting in changes to TCR area across the contact surface if the two bodies are at different temperatures. The contacting bodies are represented by a hot AA7075 rolled surface of a flat sheet with cylindrical peaks and valleys of rolling lines in 3D on the surface and a flat stainless steel die with a polished smooth surface at room temperature.

The cylindrical contact and deformation models developed in the present work are based on (i) elastic-plastic sphere to sphere contact model by Brake (2015) and (ii) an elastic-plastic spherical asperity to a rigid smooth flat contact model by Zhao et al. (2000). The proposed model is then utilized in conjunction with a thermal contact resistance (TCR) model of McGee et al. (1985) to predict TCR area as a function of applied normal load under isothermal and non-isothermal elastoplastic deformation and heat transfer conditions of the two contacting bodies.

Firstly, an elastoplastic asperity deformation analysis (or so called mechanical

analysis) which comprises of (i) single cylinder asperity on AA7075 sheet surface against smooth stainless steel flat, and (ii) multi-cylinder asperities at same (SCF) and different (MCF) heights on AA7075 sheet against flat stainless steel will be presented. Secondly, a thermal analysis involving heat transfer across the AA7075 and stainless steel surfaces will be presented.

Lastly, the mechanical and thermal models will be combined to obtain the normal load versus displacement response of the AA7075 surface, its real contact area evolution as a function of applied normal load, and thermal contact resistance characteristics of the two surfaces as a function of applied normal load under isothermal and non-isothermal (or transient) temperature conditions. In fact, three different mechanistic models will be presented with their assumptions and limitations after the basic formulation of the generalized mechanistic model is described. The actual results from the three models will be presented and discussed separately in the next chapter and compared with experimental data reported in the previous chapter.

### 4.1 Mechanical Analysis

The general assumptions of the asperity contact and deformation models are described as follows:

i. The theory is applied to contact between a soft, rough but nominally flat, elastic and strain hardening plastic body consisting of rolled AA7075 sheet at elevated temperature, and a rigid, smooth and flat body consisting of stainless steel plate at room temperature and under ambient conditions.

ii. Each asperity on the AA7075 sheet surface is modelled as a segment of cylindrical arc shape. For the elastic deformation regime, half contact width is calculated from Hertz (1881) frictionless cylindrical contact theory. Hertz elastic contact theory has its own well-known set of assumptions. These include; (a) homogeneous isotropic elastic deformation of contacting bodies, (b) half contact width is much smaller compared to the radius of the cylinder, and (c) the contact is frictionless. Beyond the yield point, volume conservation arising from plastic incompressibility of metallic materials is adopted to determine the half contact width.

iii. The mechanical as well as thermo-physical properties of both contacting bodies, soft AA7075 and rigid stainless steel, are temperature-dependent. The plastic properties of AA7075 sheet are expressed in terms of material hardness $H$, Meyer exponent $m$ and strain hardening exponent $n_{sh}$ where a relationship, $n_{sh} = m - 2$, relates the last two parameters (Tabor, 1948). Further, maximum normal pressure in the fully plastic regime is assumed to be equal to material hardness, $P_{max} \approx H$.

iv. The elasto-plastic load $F_{ep}$ in cylindrical contact can be obtained from elastic and plastic contact loads ($F_e$ and $F_p$ respectively), as expressed in Brake (2015).

v. Plastic contact load $F_p$ is calculated from the works of Tabor (1948) and Brake (2015).

vi. The asperity distribution and size are according to the real blank surface profile from optical profilometer trace.

vii. Initial cylindrical asperity on the AA7075 sheet surface flattens in the contact region with the stainless steel surface and the material from the flattened asperity region is

redistributed onto the two sides of the remaining cylindrical region. However, the deformed asperity retains its cylindrical shape on two sides of the flattened region after plastic deformation. The interactions between the contacting asperities are disregarded.

viii. Based on the experimental observations, in the solid-solid, two-sided contact of the AA7075 sheet with stainless steel upper and lower plates, there is negligible plastic deformation of the bulk AA7075 under normal loading. The models proposed are consistent with this observation, and consider only the symmetric half of the experimental conditions involving the surface asperity of the top surface of the AA7075 sheet and the bottom smooth surface of the upper stainless steel plate.

ix. There is no sliding of surfaces and no friction between the two surfaces. The model only considers normal contact between surfaces and normal loading of surfaces.

### 4.1.1 Single Cylinder-Flat Asperity Contact Model

The single cylindrical asperity in contact with a smooth, rigid and flat surface is based on the analytical works of Hertz (1881), Johnson (1985), Zhao et al. (2000), and Brake (2015). The proposed model takes into consideration strain hardening of the deformable material at elevated temperature. Only Brake (2015) considered strain hardening for spherical contact and none of the above models dealt with elevated temperature deformation of cylindrical asperities.

In the proposed model (see Fig. 4.1 below), AA7075 blank surface is shown as a half cylinder of diameter $2r_1$ with cylinder axis along the y direction and asperity height along the z direction. The stainless steel surface, in line contact with the asperity, shares a

contact length $L$ in the y direction. The arrows pointing downward indicate compressive normal load ($F$) applied across the two contacting surfaces. The symbols $E_1$, $E_2$, $\nu_1$, $\nu_2$, $k_1$ and $k_2$ represent elastic moduli, Poisson's ratios and thermal conductivities of the half cylinder and the flat surfaces respectively. Meyer exponent, yield strength and hardness of the half cylinder are expressed by symbols $m$, $S_y$, and $H$ respectively.

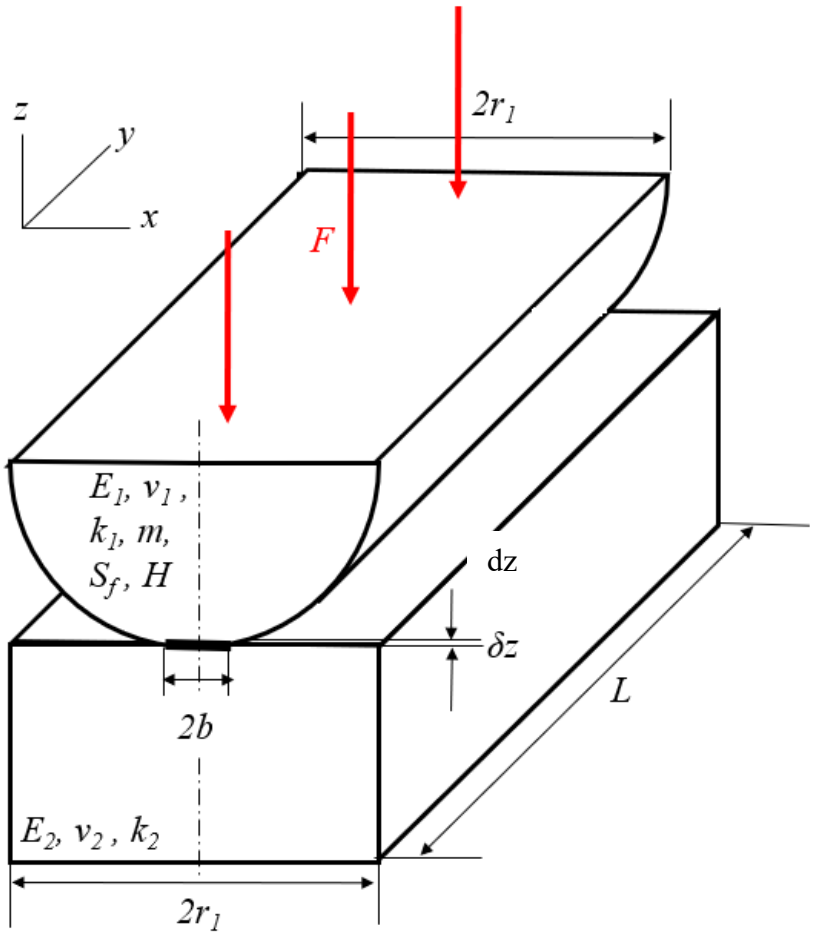


Figure 4. 1 Single cylinder-flat asperity contact model.

#### 4.1.1.1 Elastic Regime

When a small load $F_e$ is applied across deformable cylindrical asperity and rigid flat surfaces, the cylinder will first deform elastically. The elastic half contact width ($b_e$) as defined by Hertz (1881) can be expressed as:

$$b_e = \left(\frac{4F_e r}{E(T)\pi L}\right)^{1/2} \tag{4.1}$$

where *E(T)* is temperature dependent effective elastic modulus and can be written as :

$$\frac{1}{E(T)} = \frac{1-\nu_1(T)^2}{E_1(T)} + \frac{1-\nu_2(T)^2}{E_2(T)} \tag{4.2}$$

where $E_1(T)$, $E_2(T)$, $\nu_1(T)$, and $\nu_2(T)$ are temperature dependent elastic modulii and Poisson's ratios of cylindrical asperity and flat surfaces respectively. Following Hertz (1881), Johnson (1985) defined the indentation depth ($dz$) for cylindrical contact as (see earlier eqn. (2.16) in Chapter 2 on Literature Review):

$$dz = \frac{2F_e}{E(T)\pi L}\left(\ln\left(\frac{4r}{b_e}\right) - \frac{1}{2}\right) \tag{4.3}$$

#### 4.1.1.2 Yield Condition

Load can be rewritten in term of $b_e$ from Eq. 4.1 as:

$$F_e = \frac{E(T)\pi L {b_e}^2}{4r} \tag{4.4}$$

Note that, as normal load is increased, the cylindrical asperity continues to deform elastically until it reaches its yield point.

Assuming that yielding is governed by Mises yield criterion, the Mises equation in principal stress space can be expressed as:

$$J_2 = \frac{1}{2}S_{ij}S_{ij} \equiv \frac{1}{6}\left[(\sigma_x - \sigma_y)^2 + (\sigma_y - \sigma_z)^2 + (\sigma_z - \sigma_x)^2\right] = \frac{(S_y(T))^2}{3} \qquad (4.5)$$

where $J_2$ is the second invariant of deviatoric stress tensor, $S_{ij}$, and $S_y(T)$ is the temperature dependent material yield stress in uniaxial tension or compression, for isotropic materials. The maxima in principle stress components, $\sigma_x, \sigma_y,$ and $\sigma_z$ occurs at (x = z = 0) where the center of the contact area is located at the cylinder and flat surface contact plane (i.e., xz plane). The stress distributions could be expressed as a function of maximum pressure $P_{max}$, Poisson's ratio $\nu(T)$ of softer material and normalized distance ($z/b$) as follows (Shigley & Mischke, 1989)):

$$\text{Stress along x-axis, } \sigma_x = -2\nu(T)P_{max}\left[\left(1 + \left(\frac{z}{b}\right)^2\right)^{\frac{1}{2}} - \frac{z}{b}\right] \qquad (4.6)$$

$$\text{Stress along y-axis, } \sigma_y = -P_{max}\left[\left(1 + 2\left(\frac{z}{b}\right)^2\right)\left(1 + \left(\frac{z}{b}\right)^2\right)^{-\frac{1}{2}} - 2\left(\frac{z}{b}\right)\right] \qquad (4.7)$$

$$\text{Stress along z-axis, } \sigma_z = -P_{max}\left[\left(1 + \left(\frac{z}{b}\right)^2\right)^{-\frac{1}{2}}\right] \qquad (4.8)$$

where $P_{max}$ is defined as:

$$P_{max} = \frac{4}{\pi}P_m = \frac{2F}{\pi bL} \qquad (4.9a)$$

where $P_m$ is the mean pressure defined as:

$$P_m = \frac{F}{2bL} \tag{4.9b}$$

At yield, Eq. (4.9a) can be rewritten as:

$$P_{max} = \frac{2F_y}{\pi b_y L} \tag{4.10}$$

where $b_y$ and $F_y$ are half contact width and the contact load at yield, respectively. Substituting Eqs. (4.6 - 4.8) into Eq. 4.5, the expression for $J_2$ can be written in terms of $P_{max}$ as:

$$J_2 = \frac{1}{3}(P_{max})^2 f_{max}\left(\nu(T), \frac{z}{b}\right) = \frac{\left(S_y(T)\right)^2}{3} \tag{4.11}$$

where the maximum amplitude of the stress field, $f_{max}\left(\nu(T), \frac{z}{b}\right)$, in the above expression for $J_2$ , is given by:

$$f_{max}\left(\nu(T), \frac{z}{b}\right) = \max_{z\geq 0}\left(\frac{1}{2}\left[\left(2\left(\frac{z}{b}\right) - \frac{2\left(\frac{z}{b}\right)^2}{\sqrt{\left(\frac{z}{b}\right)^2+1}}\right)^2 + \left(\frac{2\left(\frac{z}{b}\right)^2+1}{\sqrt{\left(\frac{z}{b}\right)^2+1}} - 2\left(\frac{z}{b}\right) + 2\nu(T)\left(\frac{z}{b} - \sqrt{\left(\frac{z}{b}\right)^2+1}\right)\right)^2 + \left(\frac{1}{\sqrt{\left(\frac{z}{b}\right)^2+1}} + 2\nu(T)\left(\frac{z}{b} - \sqrt{\left(\frac{z}{b}\right)^2+1}\right)\right)^2\right]\right) \tag{4.12}$$

The parameter $f\left(\nu(T), \frac{z}{b}\right)$ as a function of normalized indentation depth *(z/b)* is illustrated in Fig. 4.2. The maximum *f* value (marked with a red point in the figure) for AA7075 sheet material at 380°C is 0.292 and increases slightly to 0.296 as the temperature drops to 260°C.

Both values are at a depth of $z/b$ = 0.735, which is similar to the value reported by Merwin & Johnson (1963), i.e., $(\tau_1)_{max} = 0.30P_{max}$ at z=0.78b.

Earlier Eq. 4.9(a) on substitution into Eq. 4.11 yields the following expression:

$$\left(\frac{2F_y}{\pi b_y L}\right)^2 f_{max}\left(\nu(T), \frac{z}{b}\right) = \left(S_y(T)\right)^2 \tag{4.13}$$

At yield, elastic half contact width $b_e$ (Eq. 4.1) and indentation depth $dz$ (Eq. 4.3) are replaced by symbols $b_y$ and $dz_y$ respectively to yield the following expressions:

$$b_y(T) = \left(\frac{4F_y r}{E(T)\pi L}\right)^{1/2} \tag{4.14}$$

$$dz_y(T) = \frac{2F_y}{E(T)\pi L}\left(\ln\left(\frac{4r}{b_y(T)}\right) - \frac{1}{2}\right) \tag{4.15}$$

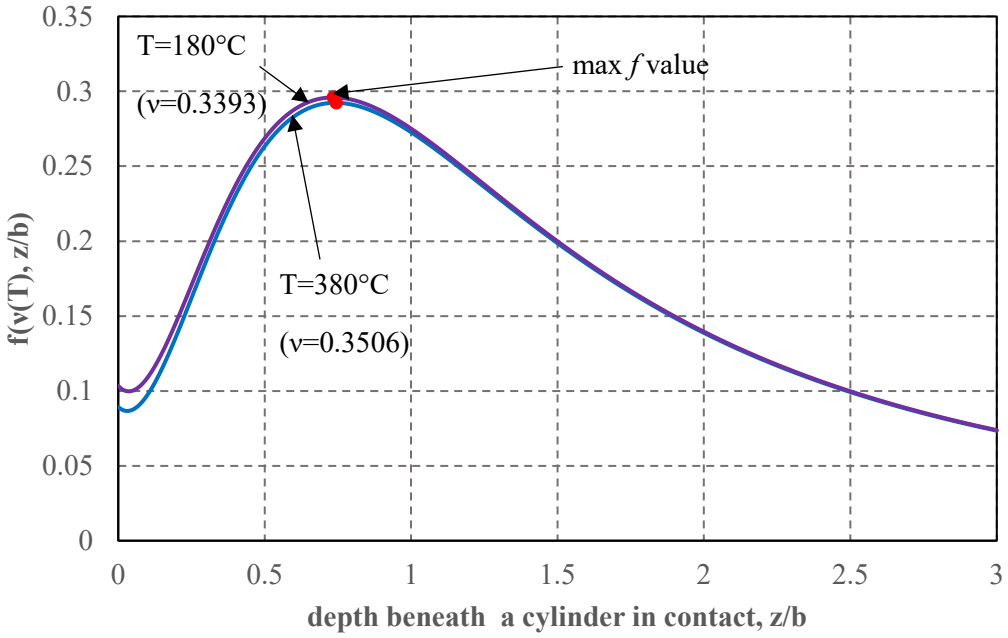


Figure 4. 2 Stress field amplitude through depth of cylinder for two temperatures, T=180°C and 380°C.

It is to be noted that the contact load at yield ($F_y$) is unknown in Eqs. (4.14) and (4.15). The following expression for $F_y$ can be obtained by substituting Eq. 4.14 into Eq. 4.13:

$$F_y = \frac{\left(S_y(T)\right)^2 \pi r L}{E(T) f_{max}\left(\nu(T), \frac{z}{b}\right)} \tag{4.16}$$

Subsequently, the indentation depth and the half contact width at yield ($dz_y$ and $b_y$) could be calculated from Eqs. (4.14) and (4.15) respectively. Note that Eqs. (4.12) and (4.16) are new equations obtained in the present work.

#### 4.1.1.3 Application of Volume Conservation to Cylindrical Segment Asperity Flattening Process

Volume conservation (i.e., plastic incompressibility) is applied in the present work to predict plastic half contact width ($b_p$) in cylindrical contact. This approach has been used by Chang et al. (1987) for spherical asperity while keeping the radius of the sphere constant. However, in the present work, instead of fixing the radius of cylindrical asperity alone, the radius of the cylindrical asperity as well as half contact width evolve simultaneously as a segment of the cylindrical asperity deforms plastically under normal load (see Figure 4.3 below for geometric details). This is a more realistic representation of asperity deformation.

The initial undeformed asperity in Figure 4.3 is shown with a green cylindrical segment of radius $r$ and height $h$. The portion of the green cylinder is shown with a solid line above the mean surface roughness value, whereas the rest of the half cylinder below the mean line is shown dashed. The truncated (or flattened) cylinders in red and blue, also shown in Figure 4.3, indicate the radii of cylinders in the yield and plastic states from

volume conservation analysis as shown below. The normal distance between the center of the cylinder and the mean line is $z$ where $z = r - h$ and $h$ is height of the initial asperity above the mean line.

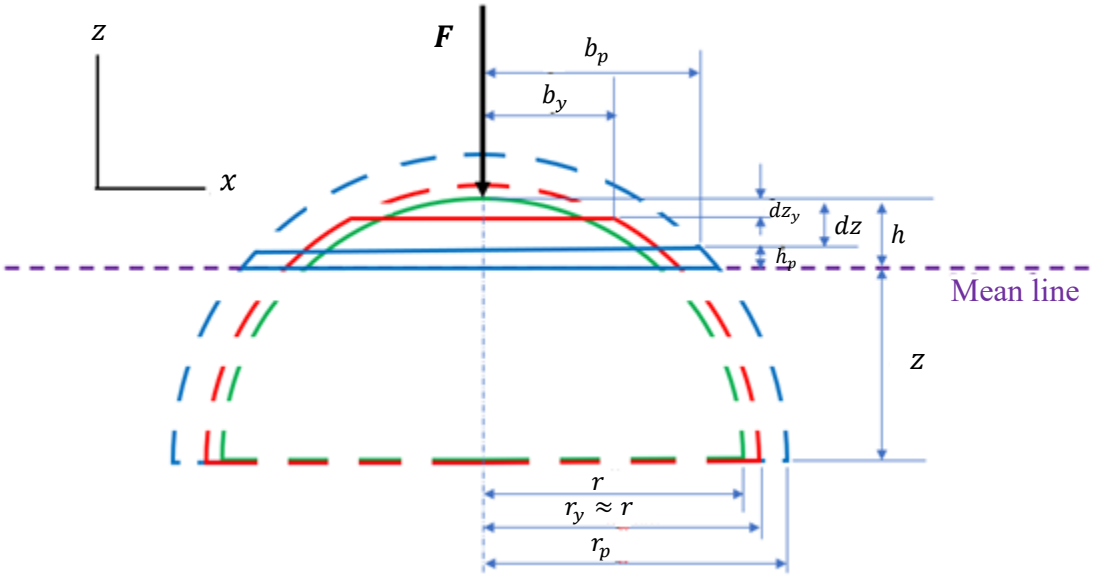


Figure 4. 3 Volume conservation applied to cylindrical asperity segment.

The initial volume of the asperity ($V_1$) can be written as:

$$V_1 = L\left(r^2 \cos^{-1}\left(\frac{z}{r}\right) - z\sqrt{r^2 - z^2}\right) \tag{4.17}$$

where $L$ is the cylinder contact length, a constant, as noted earlier (normal to the page).

This volume is conserved throughout the plastic deformation process. Since we assume that deformation occurs in plane strain, the cylindrical asperity length is also kept constant. When a contact load is applied to the asperity, it deforms elastically until the z-

displacement at yield point $dz_y$ is reached (this displacement is shown as new truncated segment in red in Fig. 4.3). Beyond this point, the asperity deforms elastoplastically (as illustrated in blue dashed curve). The shape of the deformed blue asperity may be represented by a truncated cylindrical segment of radius $r_p$ and height $h_p$. The volume of the blue asperity ($V_2$) can be written as follows:

$$V_2 = L\left({r_p}^2 \cos^{-1}\left(\frac{z}{r_p}\right) - {r_p}^2 \cos^{-1}\left(\frac{r-dz}{r_p}\right) - z\sqrt{{r_p}^2 - z^2} + (r-dz)\sqrt{{r_p}^2 - (r-dz)^2}\right) \tag{4.18}$$

From volume conservation (i.e., by equating Eqs. (4.17) and (4.18)), one can obtain $r_p$ for each indentation depth $dz_p$, and subsequently, half contact width $b_p$ from $b_p = \sqrt{{r_p}^2 - (r-dz)^2}$. Both $r_p$ and $b_p$ as a function of $dz_p$ are illustrated in Fig. 4.4(a), in which the former changes slowly while the latter evolves rapidly from its initial value.

To further analyze the change in asperity radius with indentation depth, Fig. 4.4(b) shows the ratio of the current asperity radius to the initial radius. This ratio is within the range 1 - 1.06 which indicates that $\frac{r_{fp}}{r_p} \approx 1$. This assumption will be utilized in the next sub-section.

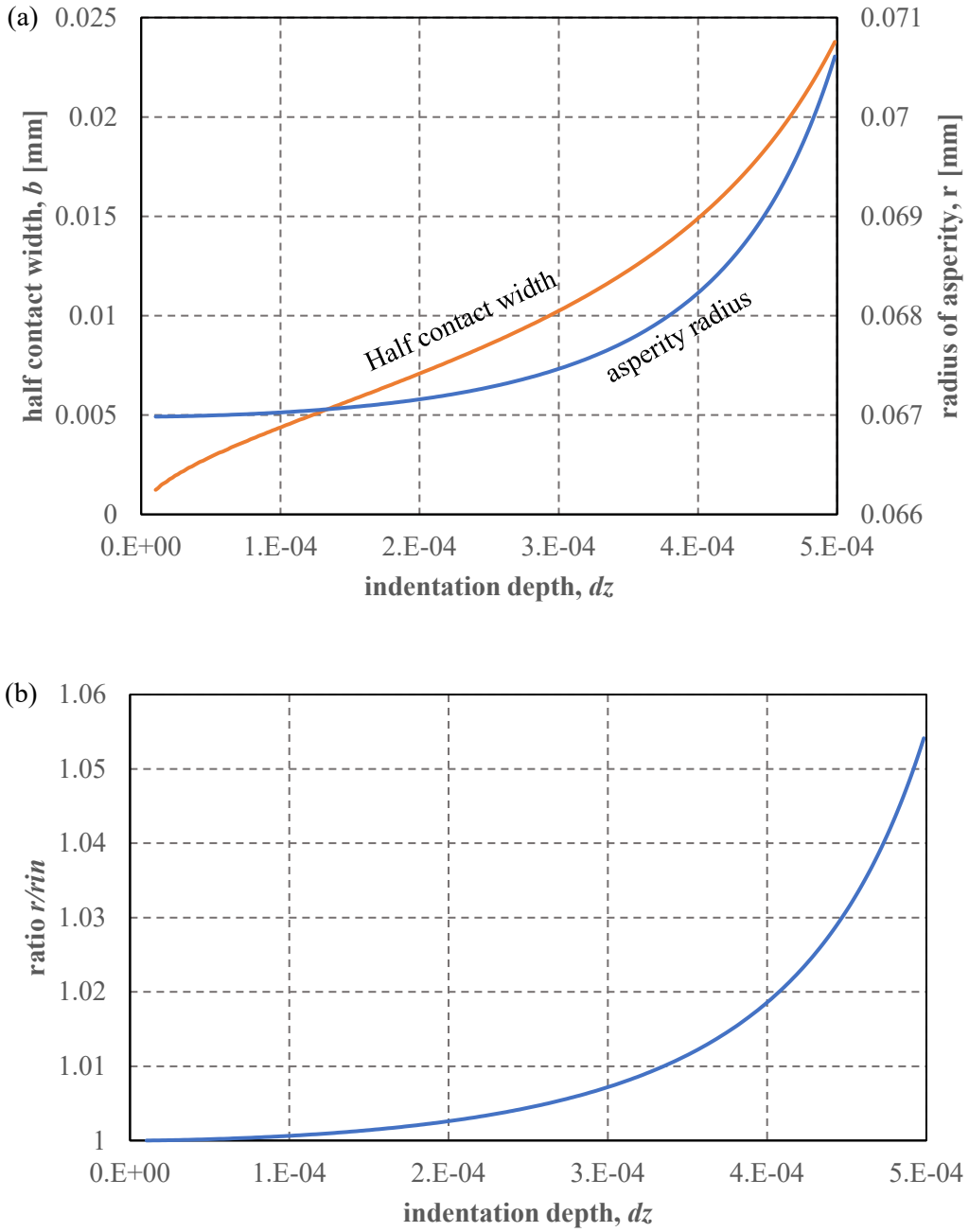


Figure 4. 4 (a) Evolution of half contact width and asperity radius with increment of indentation depth, and (b) ratio of asperity radius to initial radius with increment of indentation depth, for average initial radius r = 0.06698 mm.

#### 4.1.1.4 Elastoplastic and Plastic Regimes

##### 4.1.1.4.1 Single Cylinder-Flat Model for Cylindrical Contact based on Brake's Reformulation: Elastoplastic Regime

Elastoplastic deformation of the cylindrical asperity initiates at the onset of yielding and the plastic component increases continuously until the asperity reaches the fully developed plastic state. According to Brake (2015), the general elastoplastic behaviour of two bodies in contact can be written as:

$$F_{ep} = sech\big(2\varphi(dz)\big)F_e + \Big(1 - sech\big(2\varphi(dz)\big)\Big)F_p \tag{4.19}$$

where $F_p$ is the plastic contact load, and can be calculated based on the work of Tabor (1948, 1951). However, the tangent hyperbolic function (as depicted in Fig. 4.5) was chosen due to its smoother transition from fully elastic to fully plastic, as compared to secant hyperbolic function. Thus, a new expression for contact load during elastoplastic deformation is:

$$F_{ep} = \Big(1 - tanh\big(\varphi(dz)\big)\Big)F_e + tanh\big(\varphi(dz)\big)F_p \tag{4.20}$$

Brake defined the parameter $\varphi(dz)$ in the form $\varphi(dz) = \frac{dz - dz_y}{dz_p - dz_y}\xi$ where $\xi$ was considered equal to *m*-2. However, this expression was not well defined in Brake (2015). It was restricted to $m > 2$, and therefore, cannot be applied to elastic-perfectly plastic material. Thus, it is modified to the following form in the present work:

$$\varphi(dz) = \frac{dz - dz_y(T)}{dz_p(T) - dz_y(T)}\pi \tag{4.21}$$

Eqn. (4.21) gives values of $\varphi$ starting from $\varphi(dz_y) = 0$ at the start of asperity deformation to $\varphi(dz_{fp}) = \pi$ when the asperity is in the fully plastic state. According to Tabor (1948), the mean pressure, $P_m$ is given by:

$$P_m = \beta \left(\frac{b_p}{r_p}\right)^{m(T)-2} \tag{4.22}$$

where $\beta$ is an unknown constant while $m$ is Meyer hardness exponent. From Eq. 4.22, the elastoplastic curve is assumed to follow a power law function (Tabor, 1951). Note that, this is the case where the material is in fully annealed condition.

Since the AA7075 sheet is heated to solutionizing temperature prior to its transfer to the die for asperity flattening experiments, the assumption of fully annealed state of aluminium sheet is reasonable for the present modelling work.

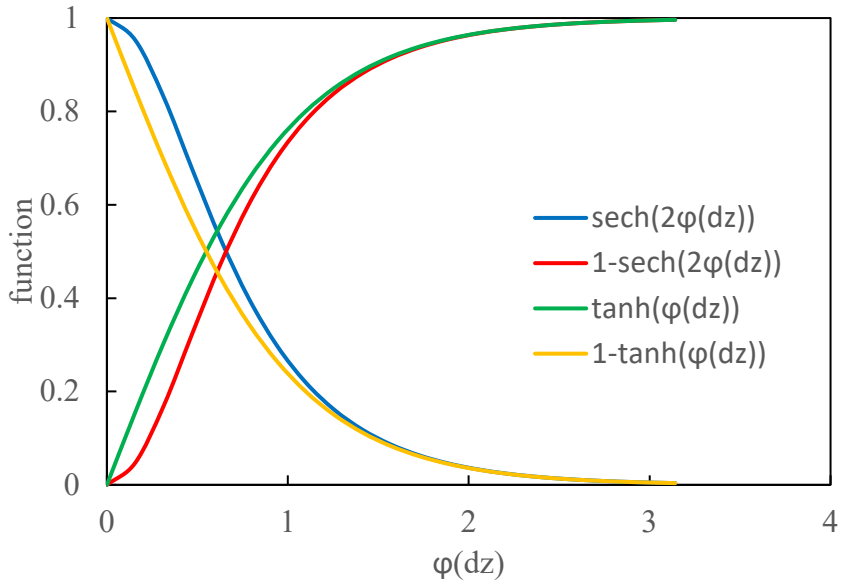


Figure 4. 5 Evolution of parameters sech (φ(dz)), 1-sech (φ(dz)), tanh (φ(dz)), and 1-tanh (φ(dz)) as a function of φ(dz).

In the following, Brake's equations dealing with spherical asperity have been revised for cylindrical asperity. According to Tabor (1948), the contact pressure for a fully developed plastic flow is equal to the material hardness, therefore Eq. (4.22) can be written as:

$$P_m|_{r=r_{fp}} = \beta \left(\frac{b_{fp}(T)}{r_{fp}}\right)^{m(T)-2} = H(T) \tag{4.23}$$

where $b_{fp}$ and $r_{fp}$ are half contact width and asperity radius at fully plastic state. Rearranging Eqn. (4.23), constant $\beta$ can be written as:

$$\beta = H(T)\left(\frac{r_{fp}}{b_{fp}(T)}\right)^{m(T)-2} \tag{4.24}$$

On substituting Eq. (4.24) into Eq. (4.22), one obtains:

$$P_m = H\left(\frac{r_{fp}}{b_{fp}(T)}\right)^{m(T)-2}\left(\frac{b_p}{r_p}\right)^{m(T)-2} = H\left(\frac{r_{fp}}{r_p}\right)^{m(T)-2}\left(\frac{b_p}{b_{fp}(T)}\right)^{m(T)-2} \tag{4.25}$$

Since $\frac{r_{fp}}{r_p} \approx 1$, Eq. 4.25 could be simplified to:

$$P_m = H(T)\left(\frac{b_p}{b_{fp}(T)}\right)^{m(T)-2} \tag{4.26}$$

On substituting Eq. 4.9b into Eq. 4.26, one obtains:

$$F_p = 2b_pLH(T)\left(\frac{b_p}{b_{fp}(T)}\right)^{m(T)-2} = 2LH(T)\frac{{b_p}^{m(T)-1}}{{b_{fp}(T)}^{m(T)-2}} \tag{4.27}$$

Finally, on substituting expressions for $F_e$ and $F_p$ from Eqs. (4.4) and (4.27) into earlier Eq. (4.20), the expression for elastoplastic load $F_{ep}$ could be obtained as:

$$F_{ep} = \left(1 - tanh\left(\frac{dz - dz_y(T)}{dz_p(T) - dz_y(T)}\pi\right)\right)\frac{E\pi L{b_e}^2}{4r} + tanh\left(\frac{dz - dz_y(T)}{dz_p(T) - dz_y(T)}\pi\right)2LH(T)\frac{{b_p}^{m(T)-1}}{b_{fp}(T)^{m(T)-2}} \tag{4.28}$$

#### 4.1.1.4.2 Single Cylinder-Flat Model for Cylindrical Contact based on Brake's Reformulation: Fully Plastic Half Contact Width ($b_{fp}$)

To determine fully plastic half contact width $b_{fp}$, one needs to create a correlation between $F_{ep}$ and $F_e$. According to Brake (2015), after yielding, the projected elastic contact load is greater than elastoplastic load, $F_{ep} \leq F_e$. Thus, for cylindrical contact, from Eq. (4.28) and Eq. (4.4), one can write:

$$\left(1 - tanh\big(\varphi(dz)\big)\right)\frac{E\pi L{b_e}^2}{4r} + tanh\big(\varphi(dz)\big)2LH(T)\frac{{b_p}^{m(T)-1}}{b_{fp}(T)^{m(T)-2}} \leq \frac{E\pi L{b_e}^2}{4r} \tag{4.29}$$

Rearrangement of Eqn. (4.29) yields,

$$tanh\big(\varphi(dz)\big)2LH(T)\frac{{b_p}^{m(T)-1}}{b_{fp}(T)^{m(T)-2}} \leq tanh\big(\varphi(dz)\big)\frac{E\pi L{b_e}^2}{4r} \tag{4.30}$$

The term $tanh\big(\varphi(dz)\big)$ from both sides of Eq. 4.30 could be cancelled, yielding:

$$2LH(T)\frac{{b_p}^{m(T)-1}}{b_{fp}(T)^{m(T)-2}} \leq \frac{E\pi L{b_e}^2}{4r} \tag{4.31}$$

Rearranging Eqn. (4.31), fully plastic half contact width $b_{fp}$ could be expressed as:

$$b_{fp}(T) \geq \left(8rH(T)\frac{{b_p}^{m(T)-1}}{E\pi{b_e}^2}\right)^{1/(m(T)-2)} \tag{4.32}$$

It is to be noted that the contact length *L* has been eliminated in Eq. (4.32). Also, due to the presence of inequality in Eq. (4.32), there are multiple possibilities for $b_{fp}$ as $b_p$ and $b_e$

vary with indentation depth. However, only one unique value of $b_{fp}$ is required in the calculation. In order to deal with this problem, the inequality of Eq. 4.32 is replaced by an equality, i.e., $b_{fp}(T) = \left(8rH(T)\frac{{b_p}^{m(T)-1}}{E\pi {b_e}^2}\right)^{1/(m(T)-2)}$, as implemented by Brake for the case of spherical asperity contact formulation.

Figure 4.6 demonstrates four different possibilities for $b_{fp}$ as indentation depth increases in the form of four blue curves with each one at a specific temperature of 260°C, 300°C, 340°C and 380°C. The uppermost curve refers to the lowest temperature of 260°C for a critical $b_{fp}$ value of 0.078 mm (shown with red symbol) corresponding to $dz_{fp}$ of 0.00029 mm. This $dz_{fp}$ value appears correct if one compares with initial asperity height h of 0.00067 mm. The lowest curve refers to T=380°C in which $b_{fp}$ is 1.92e-18 mm while corresponding $dz_{fp}$ is 0.00031 mm. The $b_{fp}$ value is clearly unrealistic as $b_y$ for this temperature is a much larger value of 0.00039 mm. On the other hand, the lowest $b_{fp}$ value for 260°C is 0.078 mm and this value is unrealistically larger than cylindrical segment radius, i.e. r=0.0677 mm. It should be noted that $b_{fp}$ should be far smaller than cylindrical segment radius. Since $dz_{fp}$ is acceptable, this reformulation model will utilize this value in volume conservation and $b_{fp}$ could be determined. In addition, since the average temperatures of hot blank and cold die temperature is of interest for TCR area calculation, and it is below 300°C from the experimental data in Chapter 3, one may use this model.

From this analysis, it appears that Brake's model (2015) is not applicable at higher temperatures such as 380°C and above as it leads to unrealistic values of characteristic half

width. It should be also noted that Brake (2015) does not present any justification for choice of equality in Eq. (4.31).

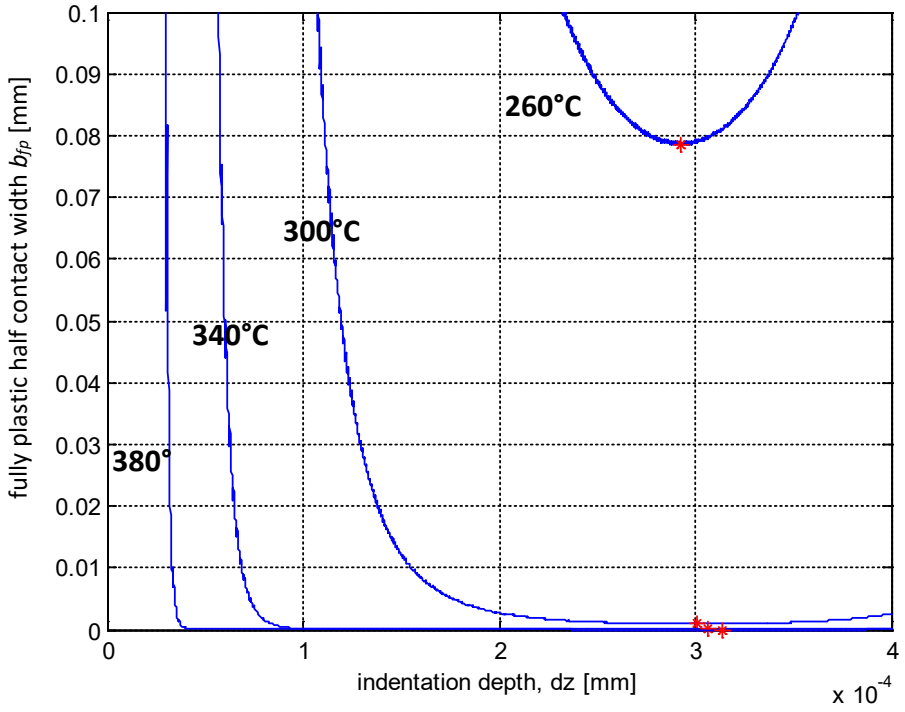


Figure 4. 6 Fully plastic half contact width $b_{fp}$ versus indentation depth curves at four different temperatures from 260°C to 380°C. The lowest value is chosen as characteristic $b_{fp}$ (shown with red asterisk symbol on each of the curves).

#### 4.1.1.4.3 Present Single Cylinder-Flat Model for Cylindrical Contact based on Reformulation of ZMC Model: Elastoplastic Regime

This sub-section deals with reformulation of asperity flattening model of Zhao et al. (2000) often mentioned in the literature as ZMC model. The model was proposed for single spherical asperity contact. It has been modified in the present work for cylindrical contact

and details of reformulation are presented below. ZMC model assumes that contact load at fully plastic state ($F_{fp}$) is 400 times the load at yield $F_y$ (or $F_{fp}/F_y = 400$) based on the experimental and finite element modeling work on spherical indentation (Johnson, 1985). If one assumes that this relationship also works for cylindrical contact, then the relationship between $dz_{fp}$ and $dz_y$ could be determined. The methodology to obtain the relationship between $dz_{fp}$ and $dz_y$ is described below:

By replacing $F_e$ and $b_e$ in the earlier Eq. (4.4) with $F_y$ and $b_{e,y}$, one obtains:

$$F_y = \frac{E(T){b_{e,y}}^2 \pi L}{4r} \tag{4.33}$$

As earlier in Brake's formulation, fully plastic load is lower than projected elastic load. Therefore,

$$F_{fp} \leq \frac{E(T){b_{e,fp}}^2 \pi L}{4r} \tag{4.34}$$

Eqn. (4.34) can be written as,

$$\frac{\frac{E(T){b_{e,fp}}^2 \pi L}{4r}}{\frac{E(T){b_{e,y}}^2 \pi L}{4r}} \geq \frac{F_{fp}}{F_y} = 400 \tag{4.35}$$

On simplification, Eqn. (4.35) yields,

$$\frac{{b_{e,fp}}^2}{{b_{e,y}}^2} \geq 400 \tag{4.36}$$

Now, using the following correlation between elastic half contact width $b_e$ and asperity radius $r$ and indentation depth $dz$ (from curve fit to a combination of Hertz and Johnson's equations (Eqns. 4.1 and 4.3), as shown in Fig. 4.7 below):

$$b_e = 0.8199r^{0.461}dz^{0.539} \tag{4.37}$$

into Eq. (4.36) yields,

$$\frac{0.8199r^{0.461}dz_{fp}(T)^{0.539}}{0.8199r^{0.461}dz_y(T)^{0.539}} \geq \sqrt{400} \tag{4.38}$$

From Eq. (4.38), the following relationship between $dz_{fp}$ and $dz_y$ is obtained:

$$dz_{fp}(T) = 245dz_y(T) \tag{4.39}$$

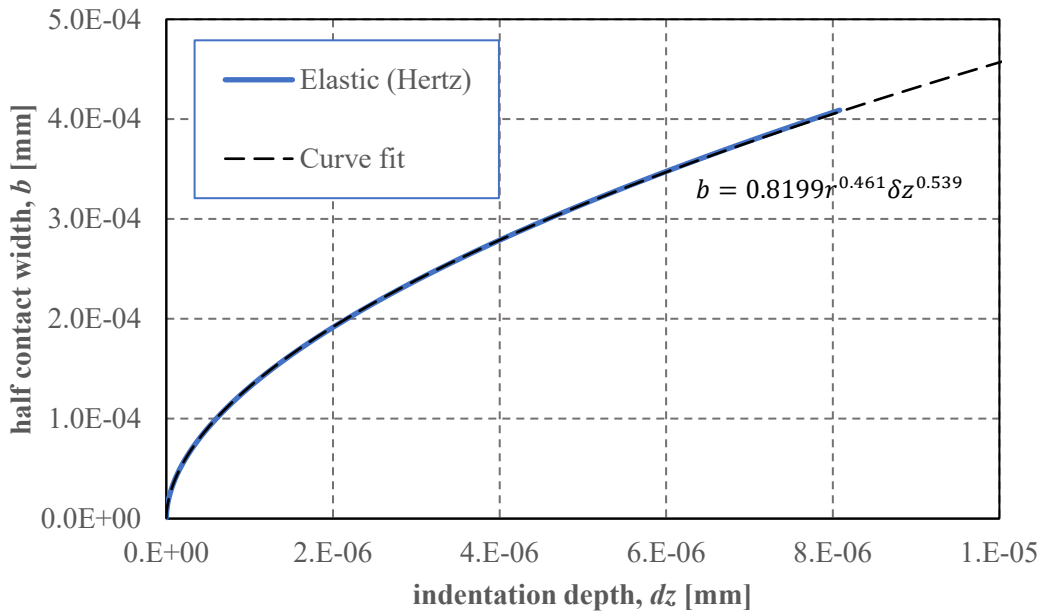


Figure 4. 7 Relationship between half contact width and indentation depth of an elastic cylinder-rigid flat (r = 0.06698 mm).

### 4.1.2 Models Involving Multiple Cylindrical Asperities in AA7075 in Contact with Flat Stainless Steel Surface (SCF and MCF Models)

In this sub-section, the basic Single Cylinder-Flat (SCF) model is incorporated in the framework of multiple asperities on aluminium sheet surface of same radii ($r$) and heights ($h$) above the mean level. Subsequently, a new Multi Cylinder-Flat (MCF) model is developed in which the multiple asperities are arranged in different discrete number densities ($n$) at different levels. This new model is more relevant to the rolled surface topography of AA7075 sheet.

Earlier experimental AA7075 blank surface profile data from Chapter 3 is utilized as geometric input in the SCF and MCF models. As observed in sub-section 3.3, there are approximately 15 asperities peaks per 1000 μm length of blank surface profile. Note that only asperities greater than 0.349 μm height from the mean line are considered, as asperities deformed between 0.349 to 0.677 μm in height. These asperities could be modelled as parallel cylindrical segment asperities with an average radius of 66.98 μm. This observation implies that the total number of asperities, $n_T$ = 150, can be represented for the total of 10000 μm (or 10 mm) length of the pressed area.

#### 4.1.2.1 SCF Model Formulation

First, for simplicity, all asperities are considered to have the same height and radius. The asperities deform simultaneously, i.e., experience elastic, yield, and plastic deformation at the same time. Three parallel cylindrical segment asperities of identical size and level are shown in Fig. 4.8, arranged along a 0.2 mm length of flat rough surface and in contact with

a rigid flat smooth surface. The terms 2c, dz, and Fi correspond to the segment diameter of cylindrical asperity, the depth of indentation, and the load applied to each asperity individually. Take note that the asperities in the figure are arranged in a way that the vertical scale is tenfold that of the horizontal scale.

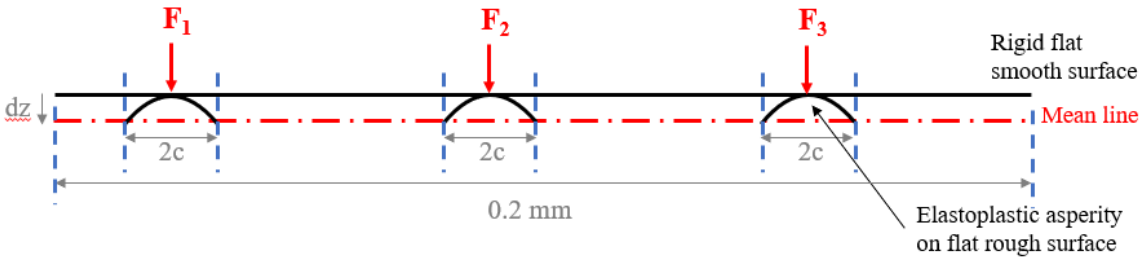


Figure 4. 8 Multi-cylindrical asperities in contact with flat smooth surface (SCF model) with uniform asperity heights.

#### 4.1.2.1.1 Determination of Total Contact Load (SCF model)

Based on spring analogy, total contact load ($F$) is the sum of individual single asperity loads. Thus, the total contact load during elastic deformation ($dz \leq dz_y$), from Eqn. (4.4):

$$F = n_T * \left(\frac{E(T)\pi L {b_e}^2}{4r}\right) \tag{4.40}$$

Total contact load during elastoplastic deformation ($dz_y < dz < dz_{fp}$) ), from eqn. (4.28):

$$F = n_T * \left(\frac{E(T)\pi L {b_e}^2}{4r}\left(1 - \tanh\left(\frac{dz - dz_y(T)}{dz_{fp}(T) - dz_y(T)}\pi\right)\right) + 2LH(T)\frac{{b_p}^{m(T)-1}}{b_{fp}(T)^{m(T)-2}}\tanh\left(\frac{dz - dz_y(T)}{dz_{fp}(T) - dz_y(T)}\pi\right)\right) \tag{4.41}$$

Total contact load during plastic deformation ($dz \geq dz_{fp}$) ), from Eqn. (4.27):

$$F = n_T * \left(2LH(T)\frac{{b_p}^{m(T)-1}}{b_{fp}(T)^{m(T)-2}}\right) \tag{4.42}$$

Note that elastic and plastic half contact widths *($b_e$* and *$b_p$)* are obtained from expressions presented earlier in Eq. 4.1, and the volume conservation assumption respectively.

#### 4.1.2.1.2 Determination of Total Contact Area (SCF model)

Based on spring analogy, the total contact area ($A_r$) is the total of all contact areas of single asperities. Total contact area during elastic deformation ($dz \leq dz_y$):

$$A_r = n_T * 2L * (b_e) \tag{4.43}$$

Total contact area during elastoplastic deformation ($dz_y < dz < dz_{fp}$):

$$A_r = n_T * 2L * \left(b_e + \left(b_p - b_e\right)\tanh\left(\frac{dz - dz_y(T)}{dz_{fp}(T) - dz_y(T)}\pi\right)\right) \tag{4.44}$$

Total contact area during plastic deformation ($dz \geq dz_{fp}$):

$$A_r = n_T * 2L * \left(b_p\right) \tag{4.45}$$

### 4.1.2.2 MCF Model Formulation: Configuration of Asperities Distribution at Different Levels

This sub-section considers a configuration of three asperities of three different heights, referred to as three asperity levels, and arranged in a random manner transverse to the rolling lines on a rolled aluminium sheet surface. The asperities will deform in a sequential manner: Level 1, Level 2 and Level 3 asperities.

As mentioned previously, there are 15 parallel cylindrical asperities per 1000 μm of blank surface profile. For this configuration, the asperities are arranged in different asperity numbers at different levels. Thus, for 10000 μm of pressed area, the 150 asperities are distributed as follows:

iv. Level 1 (height, $0.6<h_1\leq0.67$ μm): $n_1$ asperities

v. Level 2 (height, $0.4<h_2\leq0.6$ μm): $n_2$ asperities

vi. Level 3 (height, $0.349<h_3\leq0.4$ μm): $n_3$ asperities

in which $n_1 + n_2 + n_3 = 150$ asperities.

#### 4.1.2.2.1 Determination of Total Contact Load (MCF model)

In contrast to the SCF model, there are multiple asperities at different levels, thus, the total contact load ($F$) is the summation of individual single asperity loads at the first level, then upon reaching the next level, $F$ is the summation of single asperity loads at first and the next level, and so on. Total contact load during elastic deformation ($dz \leq dz_y$):

$$F = \sum_{i=1}^{l} n_i * \left(\frac{E(T)\pi L {b_e}^2}{4r}\right)_i \tag{4.46}$$

Total contact load during elastoplastic deformation ($dz_y < dz < dz_{fp}$):

$$F = \sum_{i=1}^{l} n_i * \left(\frac{E(T)\pi L {b_e}^2}{4r}\left(1 - \tanh\left(\frac{dz-dz_y(T)}{dz_{fp}(T)-dz_y(T)}\pi\right)\right) + 2LH(T)\frac{{b_p}^{m(T)-1}}{{b_{fp}(T)}^{m(T)-2}}\tanh\left(\frac{dz-dz_y(T)}{dz_{fp}(T)-dz_y(T)}\pi\right)\right)_i \tag{4.47}$$

Total contact load during plastic deformation ($dz \geq dz_{fp}$):

$$F = \sum_{i=1}^{l} n_i * \left( 2LH(T) \frac{{b_p}^{m(T)-1}}{{b_{fp}(T)}^{m(T)-2}} \right)_i \tag{4.48}$$

where $n_i$ and $i$ represent number of asperities at a specific level, and the number of asperities levels, respectively. Note that elastic and plastic half contact widths *($b_e$* and *$b_p$)* are obtained from expressions presented earlier in Eq. 4.1, and combination of Eq. 4.1 and the volume conservation assumption respectively.

#### 4.1.2.2.2 Determination of Total Contact Area (MCF model)

Based on spring analogy, the total contact area ($A_r$) is the total single contact area of an asperity. Total contact area during elastic deformation ($dz \leq dz_y$):

$$A_r = 2L * \sum_{i=1}^{l} n_i * (b_e)_i \tag{4.49}$$

Total contact area during elastoplastic deformation ($dz_y < dz < dz_{fp}$):

$$A_r = 2L * \sum_{i=1}^{l} n_i * \left( b_e + (b_p - b_e) \tanh\left( \frac{dz - dz_y(T)}{dz_{fp}(T) - dz_y(T)} \pi \right) \right)_i \tag{4.50}$$

Total contact area during plastic deformation ($dz \geq dz_{fp}$):

$$A_r = 2L * \sum_{i=1}^{l} n_i * \left( b_p \right)_i \tag{4.51}$$

#### 4.1.2.2.3 Determination of Thermal Contact Resistance for Asperity Contact Model (SCF and MCF models)

Fig. 4.1 at the beginning of this chapter presented the single cylinder-flat contact region. The physical configuration in the figure was utilized to obtain the expression for solid-solid

TCR (expressed by symbol $R_c$) for single asperity contact (earlier Eq. 2.57 is repeated here) as follows:

$$R_c = \frac{1}{\pi L k_C(T)} ln\left(\frac{4r}{b}\right) - \frac{1}{2Lk_C(T)} + \frac{1}{\pi L k_F(T)} ln\left(\frac{2r}{\pi b}\right) \tag{4.52}$$

This equation is taken from the work of McGee where $k_C$ and $k_F$ are the thermal conductivities of the cylinder and flat surfaces as a function of temperature, respectively. To account for multi-cylindrical asperities on the AA7075 sheet surface contacting the flat rigid stainless steel die surface, the total TCR is considered as a sum of contact resistances of each asperity in contact. Equation 4.52 is thus reformulated as:

$$R_c = n_T * \left[\sum_{i=1}^{l} \frac{n_i}{\left(\frac{1}{\pi L k_C(T)} ln\left(\frac{4r}{b}\right) - \frac{1}{2Lk_C(T)} + \frac{1}{\pi L k_F(T)} ln\left(\frac{2r}{\pi b}\right)\right)_i}\right]^{-1} \tag{4.53}$$

where total number of asperities and half contact width ($b$) could be determined according to the mode of deformation; elastic, elastoplastic or plastic. Half contact width during elastic deformation ($dz \leq dz_y$) is given by:

$$b = b_e \tag{4.54}$$

Half contact width during elastoplastic deformation ($dz_y < dz < dz_{fp}$):

$$b = b_e + \left(b_p - b_e\right) \tanh\left(\frac{dz - dz_y(T)}{dz_{fp}(T) - dz_y(T)} \pi\right) \tag{4.55}$$

Half contact width during plastic deformation ($dz \geq dz_{fp}$):

$$b = b_p \tag{4.56}$$

## 4.2 Summary

In this chapter, the various modeling approaches have been explained in detail. There are two main asperity flattening models: Brake (2015) and ZMC (2000). Both models have been reformulated in the present work for the case of single and multiple cylindrical rolled asperities at elevated temperature in contact with a smooth and flat surface at room temperature. From these analyses, expressions for total contact area, total contact load and total TCR area are obtained. The effect of different asperity heights and radii distributions are presented as explicit equations.

### 4.2.1 Summary of the Formulas for All Models

The total TCR (or *R* value) is a combination of thermal resistances through solid-to-solid contact ($R_c$), air gaps thermal resistance ($R_{air}$), and radiation thermal resistance ($R_r$) as follows:

$$R = \left(\frac{1}{R_c} + \frac{1}{R_{air}} + \frac{1}{R_r}\right)^{-1} \tag{4.57}$$

in which the three resistances are determined from the following expressions:

$$R_c = n_T * \left[\sum_{i=1}^{l} \frac{n_i}{\left(\frac{1}{\pi L k_C(T)} ln\left(\frac{4r}{b}\right) - \frac{1}{2Lk_C(T)} + \frac{1}{\pi L k_F(T)} ln\left(\frac{2r}{\pi b}\right)\right)_i}\right]^{-1} \tag{4.58}$$

$$R_{air} = \left[\sum_{i=1}^{l} n_i \left(\frac{2L\Delta T_o \int_b^r \frac{dx}{\frac{2r}{k_S(T)} + \frac{\delta(x)+\alpha\beta\lambda}{k_{air}(T)} + \frac{\delta(x)}{k_C(T)}}}{\Delta T_c}\right)_i\right]^{-1} \tag{4.59}$$

$$R_r = \left[\sum_{i=1}^{l} n_i \left(\frac{8\sigma r L {T_m}^3}{\left[\frac{1-\varepsilon_F}{\varepsilon_F}+\frac{\pi+2-4F_{fc}}{\pi-2{F_{fc}}^2}+\frac{2(1-\varepsilon_C)}{\pi\varepsilon_C}\right]}\right)_i\right]^{-1} \quad (4.60)$$

where $r$, $L$, $k_C(T)$, $k_F(T)$, $k_s(T)$, $k_{air}(T)$ and $n_i$ are cylindrical asperity radius and length, temperature-dependent thermal conductivities of cylinder and flat in contact, effective thermal conductivity, thermal conductivity of air gaps, and number of asperities at a specific level, respectively. Additionally, $\Delta T_c$, $\Delta T_o$, $T_m$, $\varepsilon_F$, $\varepsilon_C$ and $F_{fc}$ are temperature difference at contact, temperature difference between cylinder and flat from thermocouple reading, average temperature of flat and cylinder, emissivity of flat and cylinder, and shape factor between flat and cylinder, respectively. For convenience, the Eq. 4.57 could also be multiplied by nominal area ($A$) to relate to IHTC:

$$RA = A\left(\frac{1}{R_c} + \frac{1}{R_{air}} + \frac{1}{R_r}\right)^{-1} \quad (4.61)$$

To establish the relationship with thermal contact resistance, total real contact area ($A_r$) and total contact load ($F$) have to be determined for elastic and elastoplastic ranges. The total real contact area is the product of two times half contact width ($b$) and the length of asperity length $L$. Within the elastic range, all models follow the Hertzian expressions:

$$A_r = 2L * \sum_{i=1}^{l} n_i * \left(\sqrt{\frac{4F_e r}{E(T)\pi L}}\right)_i \quad (4.62)$$

$$F = \sum_{i=1}^{l} n_i * \left(\frac{E(T)\pi L {b_e}^2}{4r}\right)_i \quad (4.63)$$

where *E(T)* is temperature dependent effective elastic modulus. Beyond the elastic region, both models share the same equations to determine real contact area and contact load at the elastoplastic region. The only difference between modified Brake and modified Brake-ZMC models is the approach to obtain the indentation depth ($dz_{fp}(T)$) and half contact width ($b_{fp}(T)$) at fully plastic state as mentioned previously in this chapter (see Eqns. 4.32 and 4.39).

For elastoplastic range, the expressions for $A_r$ and $F$ are given by:

$$A_r = 2L * \sum_{i=1}^{l} n_i * \left( b_e + \left( b_p - b_e \right) \tanh\left( \frac{dz - dz_y(T)}{dz_{fp}(T) - dz_y(T)} \pi \right) \right)_i \tag{4.64}$$

$$F = \sum_{i=1}^{l} n_i * \left( \frac{E(T)\pi L {b_e}^2}{4r} \left( 1 - \tanh\left( \frac{dz - dz_y(T)}{dz_{fp}(T) - dz_y(T)} \pi \right) \right) + 2LH(T) \frac{{b_p}^{m(T)-1}}{{b_{fp}(T)}^{m(T)-2}} \tanh\left( \frac{dz - dz_y(T)}{dz_{fp}(T) - dz_y(T)} \pi \right) \right)_i \tag{4.65}$$

where $dz_y(T)$, $dz_{fp}(T)$, $b_y(T)$, and $b_{fp}(T)$ are temperature-dependent indentation depth and half contact width at yield and at fully plastic state respectively. In addition, both material hardness *H(T)* and Meyer's hardness coefficient *m(T)* are also temperature-dependent.

Finally, during plastic deformation, all models follow the expressions:

$$A_r = 2L * \sum_{i=1}^{l} n_i * \left( b_p \right)_i \tag{4.66}$$

$$F = \sum_{i=1}^{l} n_i * \left( 2LH(T) \frac{{b_p}^{m(T)-1}}{{b_{fp}(T)}^{m(T)-2}} \right)_i \tag{4.67}$$

# Chapter 5

## Results and Discussion

This chapter presents results from two different mechanistic models presented in Chapter 4 and their comparison with the experimental results. The first model 'modified Brake' is a reformulation of Brake (2015) model for elastoplastic sphere-to-sphere contact with strain hardening effect at room temperature. The reformulated model considers elastoplastic cylinder-to-flat contact with strain hardening effect and volume conservation at elevated temperature. The second model 'modified Brake-ZMC' improves the first model based on single elastoplastic sphere-flat contact model of Zhao et al. (2000) applied at room temperature. The improved model adopts experimental fully plastic half contact width and indentation depth to an elastoplastic cylinder-to-flat contact at elevated temperature of the AA7075 surface.

For each model, results from single uniform asperities (termed 'SCF') and three asperities (termed 'MCF') level distributions as described in Chapter 4 are presented. In addition, the analysis considers (i) a series of discrete isothermal (termed 'Iso') and (ii) transient (termed 'Trans') temperature conditions of the contacting bodies. The Iso case is evaluated at different constant temperatures of AA7075 sheet (130°C to 280°C) considering average blank and die temperatures in the analysis. The transient temperature condition is closer to the hot stamping temperature conditions as the hot AA7075 blank cools continuously in contact with the cold die during clamping and forming steps. This

condition was analyzed by utilizing average (blank and die) temperatures of the thermocouples embedded in the blank and die.

For model behavioural comparisons and validation with experiments, the predictions from the models are compared with experimental data in terms of; (i) load applied to the AA7075 blank by the stainless steel plate to cause primarily asperity deformation versus displacement of the blank (in other words, indentation load versus depth arising from AA7075 asperity pressing), (ii) real contact area versus load curves, and (iii) thermal contact resistance per unit area versus load curves. The experimental data presented earlier in Chapter 3 were rearranged to make them compatible with the model results for validation purposes.

### 5.1 Sensitivity Analysis of Asperity Geometric Parameters

In this sub-section, four analyses comprising of sensitivities of surface parameters as well as air gaps and radiation resistances in the contact region between the two surfaces are conducted for TCR area prediction from SCF and MCF contact models. The parameters include the effect of isothermal/transient temperature conditions; asperities radii and contribution of elastic/plastic part; number distribution of asperities; and air gaps/radiation resistances. For both modified Brake and Brake-ZMC models, isothermal case is considered once for comparison with transient case while the rest of the analyses utilize transient average temperature from the thermocouple data.

### 5.1.1 Analysis 1: Effect of isothermal and transient temperature conditions in modeling

For this first analysis, the transient model is compared to isothermal one for its significance. As mentioned previously, hot stamping process occurs under non-isothermal conditions, and this introduces additional complexity to the analysis. In this sub-section, SCF contact models at six different constant temperatures, 130°C, 160°C, 190°C, 220°C, 250°C and 280°C, are compared with a transient case for the two models.

As for the calculation, the input parameters consisting of material and thermal properties of AA7075 and stainless steel at different temperatures are presented in Table 5.1. The elastic modulus ($E$), yield strength ($S_y$), hardness ($H$) and Meyer hardness coefficient ($m$) of both materials in contact exhibit a decreasing trend with the increment of temperature. However, Poisson's ratio ($v$) and thermal conductivity ($k$) show an opposite trend. Note that the inputs are the same for both Brake and Brake-ZMC models and valid for any asperity radius. In this analysis, the geometry of asperities is fixed, i.e., average radius, $r$ = 0.06698 mm and length, $L$=7.854 mm and the number of asperities is 150.

In Table 5.2, both models share the same elastic properties values for output parameters, i.e., half contact width and indentation depth at yield. However, the uniqueness of modified Brake and modified Brake-ZMC models come to light at different plastic properties values, i.e., half contact width and indentation depth at fully plastic state. For the former model, both half contact width and indentation depth at fully plastic increase with an increase in temperature, while for the latter an opposite pattern exists (Figure 5.1).

Table 5. 1 Input parameters for isothermal modeling.

| Model | Temp. [°C] | Input parameters | | | | | |
|---|---|---|---|---|---|---|---|
| | | Elastic properties | | | | | |
| | | $E_1$ [MPa] | $E_2$ [MPa] | $\nu_1$ | $\nu_2$ | E [MPa] | Sy [MPa] |
| All | 130 | 66782 | 190599 | 0.337 | 0.257 | 55020 | 145.79 |
| | 160 | 65609 | 188766 | 0.338 | 0.262 | 54255 | 138.84 |
| | 190 | 64437 | 186776 | 0.340 | 0.269 | 53489 | 132.17 |
| | 220 | 63265 | 184630 | 0.341 | 0.277 | 52723 | 125.76 |
| | 250 | 62092 | 182326 | 0.343 | 0.286 | 51958 | 119.63 |
| | 280 | 60920 | 179866 | 0.345 | 0.298 | 51193 | 113.76 |

| Model | Temp. [°C] | Input parameters | | | |
|---|---|---|---|---|---|
| | | Plastic properties | | Thermal properties | |
| | | H [MPa] | m | $k_1$ [W/mK] | $k_2$ [W/mK] |
| All | 130 | 1000.71 | 2.22 | 132.00 | 16.13 |
| | 160 | 888.45 | 2.20 | 134.81 | 16.78 |
| | 190 | 752.48 | 2.17 | 137.53 | 17.40 |
| | 220 | 608.42 | 2.14 | 140.16 | 18.02 |
| | 250 | 473.24 | 2.11 | 142.70 | 18.62 |
| | 280 | 357.90 | 2.08 | 145.14 | 19.21 |

Theoretically, as the temperature increases, the blank material stiffness and strength should be reduced. Thus, the material would flow easily in the fully plastic region, which would lead to lower values of half contact width and indentation depth at fully plastic state. This response would apply to the modified Brake-ZMC model.

Various comparisons between steady (isothermal) and transient state models for both models are presented in Figs. 5.2 – 5.4. Figures 5.2 (a) and (b) show the curvatures of indentation depth as a function of contact load for modified Brake and modified Brake-

Table 5. 2 Output parameters for isothermal modeling (r = 0.06698 mm).

| Model | Temp. [°C] | Output parameters | | | |
|---|---|---|---|---|---|
| | | Elastic properties | | Plastic properties | |
| | | $b_y$ [mm] | $\delta z_y$ [mm] | $b_{fp}$ [mm] | $\delta z_{fp}$ [mm] |
| Modified Brake | 130 | 6.52E-04 | 1.75E-05 | 8.84E-03 | 2.59E-04 |
| | 160 | 6.30E-04 | 1.64E-05 | 8.97E-03 | 2.63E-04 |
| | 190 | 6.09E-04 | 1.55E-05 | 9.20E-03 | 2.70E-04 |
| | 220 | 5.88E-04 | 1.45E-05 | 9.50E-03 | 2.79E-04 |
| | 250 | 5.68E-04 | 1.36E-05 | 9.78E-03 | 2.87E-04 |
| | 280 | 5.49E-04 | 1.28E-05 | 1.02E-02 | 2.99E-04 |
| Modified Brake-ZMC | 130 | 6.52E-04 | 1.75E-05 | 2.36E-02 | 4.30E-03 |
| | 160 | 6.30E-04 | 1.64E-05 | 2.29E-02 | 4.03E-03 |
| | 190 | 6.09E-04 | 1.55E-05 | 2.22E-02 | 3.79E-03 |
| | 220 | 5.88E-04 | 1.45E-05 | 2.15E-02 | 3.56E-03 |
| | 250 | 5.68E-04 | 1.36E-05 | 2.09E-02 | 3.34E-03 |
| | 280 | 5.49E-04 | 1.28E-05 | 2.03E-02 | 3.13E-03 |

ZMC respectively. The red arrow with the sign ‘T’ in the figures indicates the direction in which the temperature is increasing. The contact load here is calculated from Eqs. 4.63, 4.65 and 4.67. Overall, as the loads increase the indentation depth increases non-linearly and moves towards a saturation point, i.e., towards the height of asperities, z=0.677 μm (beyond the values in the figures). In the beginning, the indentation depth increases elastically as the load increases. All curves almost collapse into one curve in which the effect of temperature is not significant. This is due to very minor variation in effective elastic modulus at different temperatures (refer to Eq. 4.4).

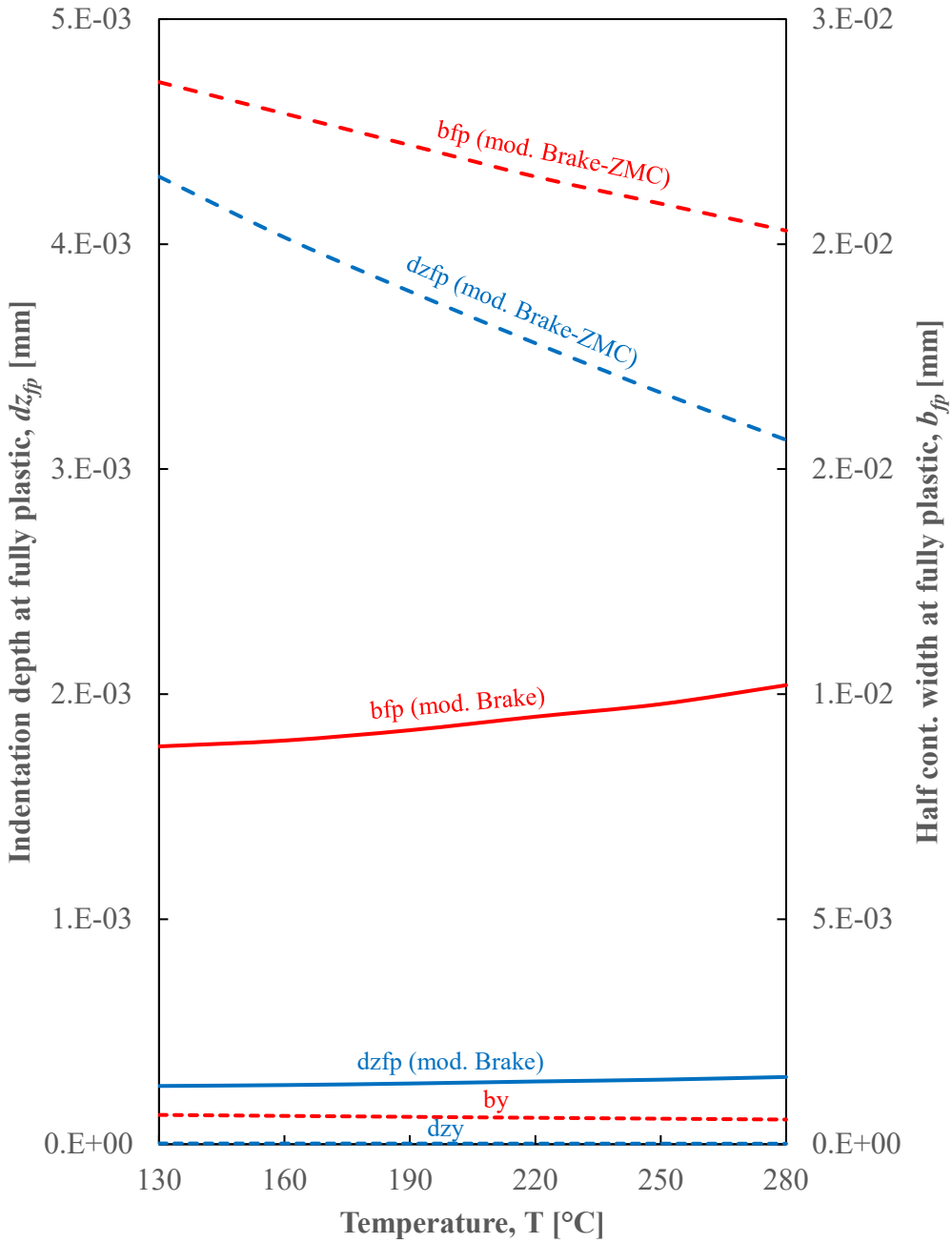


Figure 5. 1 Comparison of indentation depth and half contact width at fully plastic state as a function of temperature from modified Brake and modified Brake-ZMC models.

As the indentation depth traverses the yield point, i.e., 12.8 ~ 17.5 nm, plastic deformation initiates and respective curves start to deviate. The deviation is obvious in modified Brake model compared to modified Brake-ZMC model. This occurs mainly due to the different values of indentation depth and half contact width at fully plastic state between the two models. As stated in Table 5.2, modified Brake model has values a magnitude lower for both parameters. Thus, the indentation depth curves take shorter path to reach fully plastic state. In the other words, the elastic part diminishes while the plastic part prevails in the elastoplastic region of modified Brake model. Note that, in this analysis, modified Brake model reaches fully plastic state more readily, i.e., in the range 0.26 ~ 0.30 μm, while modified Brake-ZMC model remains in the elastoplastic region. Beyond this point, modified Brake model behaves plastically.

In comparing curves at different temperatures, the highest temperature (280°C) curve has the deepest indentation depth at a specific load. This is true as the material becomes more ductile as the temperature rises. For both models, the transient curve passes through the isothermal curves at 190°C and 220°C. However, the transient curve of modified Brake model could not match the experimental data. Only isothermal curve at 250°C matches the two experimental data points. Modified Brake-ZMC shows better prediction in which the transient and isothermal curves at 130°C and 160°C match all of the data points.

The contact area versus contact load curves for modified Brake and modified Brake-ZMC are presented in Figures 5.3 (a) and (b) respectively. The formulas to determine the contact areas were provided earlier in Eqs. 4.56, 4.58 and 4.60. Similar trend to the previous

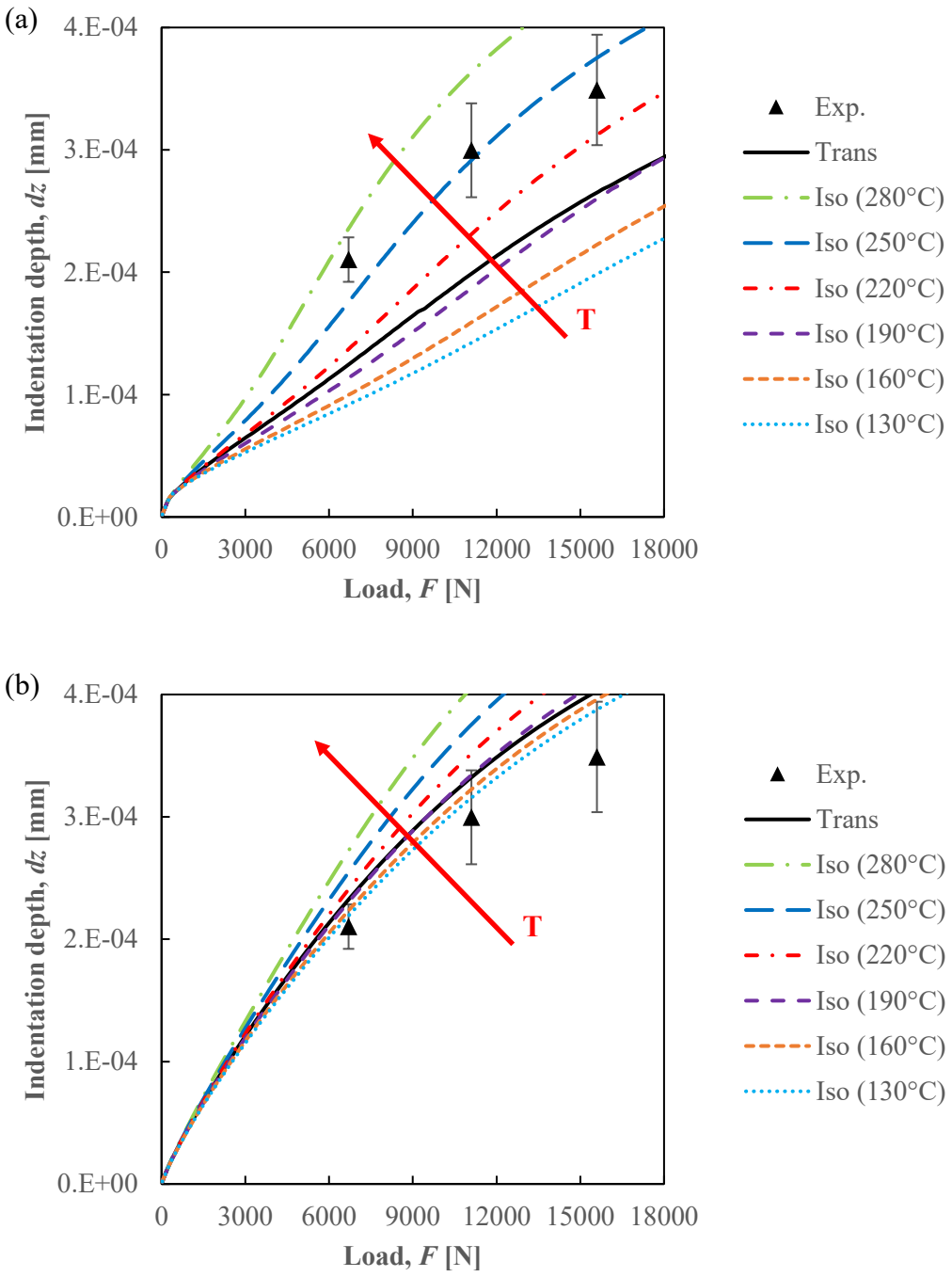


Figure 5. 2 Contact load as a function of indentation depth for SCF; (a) modified Brake, and (b) modified Brake-ZMC contact models of hot AA7075 blank indented by cold stainless steel die.

F-dz graphs, as the load is increased, the total real contact area approaches the nominal area of 78.54 $mm^2$. As expected, modified Brake model diverges earlier with a larger gap after passing through the yield point. The percentage of elastic part rapidly changes from hundred to zero per cent as plastic part grows towards fully plastic point. This is not the case for modified Brake-ZMC model in which the elastic part transitions to plastic part far more gradually.

In comparing the total real contact area at the highest and the lowest temperatures for a contact load of 6700 N (85.3 MPa), the curves at 130°C and 280°C from modified Brake model predict areas of 8 $mm^2$ and 19 $mm^2$ respectively, which correspond to 10% and 24% of nominal area. This demonstrates that even under high pressure, the real contact area is relatively small compared to the nominal contact area (Tabor, 1951). On the other hand, modified Brake-ZMC model predicts 8% (130°C) and 11% (280°C) of nominal contact area at the same loading. This phenomenon corresponds to the ductility of materials in contact as the temperature increases.

In Figure 5.3 (a), only isothermal curves at 130°C and 160°C of Modified Brake model agree well with all measured data while the other curves overpredict it. Modified Brake-ZMC model shows better prediction in which transient and isothermal curves at 160°C and 190°C pass through all experimental data points (Fig. 5.3 (b)). Note that the curve at higher temperature does not show a convex shape due to hyperbolic tangent term in the elastoplastic equation.

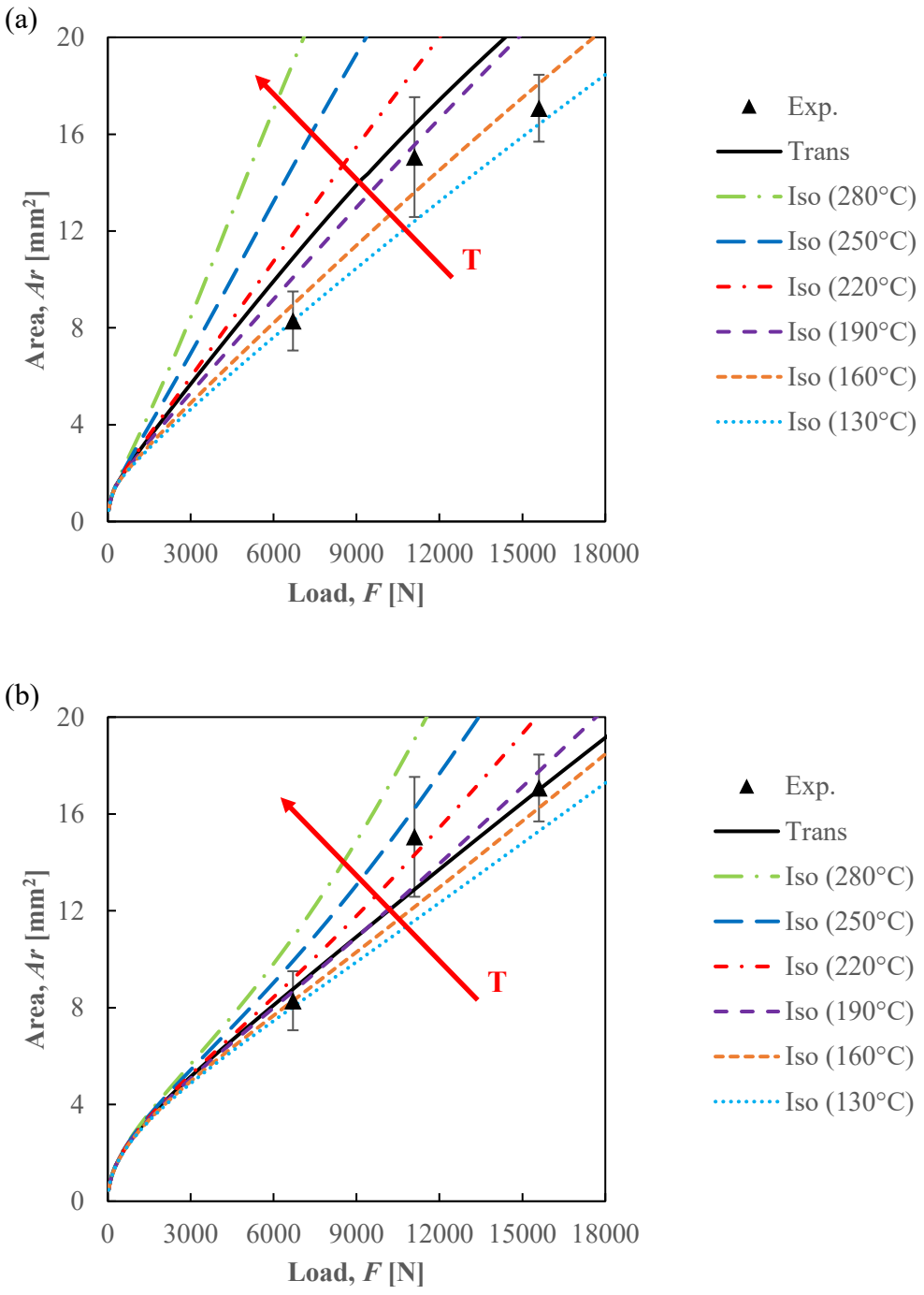


Figure 5. 3 Contact area as a function of contact load for SCF; (a) modified Brake, and (b) modified Brake-ZMC contact models of hot AA7075 blank indented by cold stainless steel die.

Figure 5.4 (a, b) presents the curves of TCR area as a function of contact load for modified Brake and modified Brake-ZMC models respectively. It is obvious that the TCR area decreases as the contact load increases. This could be explained from the previous figures in which the total real contact area increases significantly with the increment of contact load, thus, more heat could be transferred from hot AA7075 blank to cold stainless steel dies. Meanwhile, TCR area within elastic range, i.e., load up to 400 N, drops dramatically. From the previous discussion, it is reasonable to say the curves at different temperatures depart after the yield point. This occurs due to the saturation of contact area at the end of the deformation.

It is clearly seen that when the temperature rises, TCR area decreases. At 11.1 kN load, the isothermal curves at the lowest and highest temperatures of modified Brake model predict TCR area values of 470 and 227 $mm^2K/W$ respectively. As explained earlier, as the temperature increases, the contacting materials become more ductile, resulting in a rise in real contact area, and thus a corresponding drop in TCR area. Modified Brake-ZMC model shows similar pattern which predicts TCR area values of 484 and 317 $mm^2K/W$ for the lowest and highest temperatures at the same loading.

In comparison to experimental data, modified Brake model's isothermal curves at 160°C and 190°C were successfully predicted for all data points (see Fig. 5.4 (a)). The transient, and isothermal curves agree with two last data points, whereas the other curves underpredict the experimental data. Meanwhile, four curves of Modified Brake-ZMC model exhibit better agreement in which transient as well as isothermal curves at 160°C,

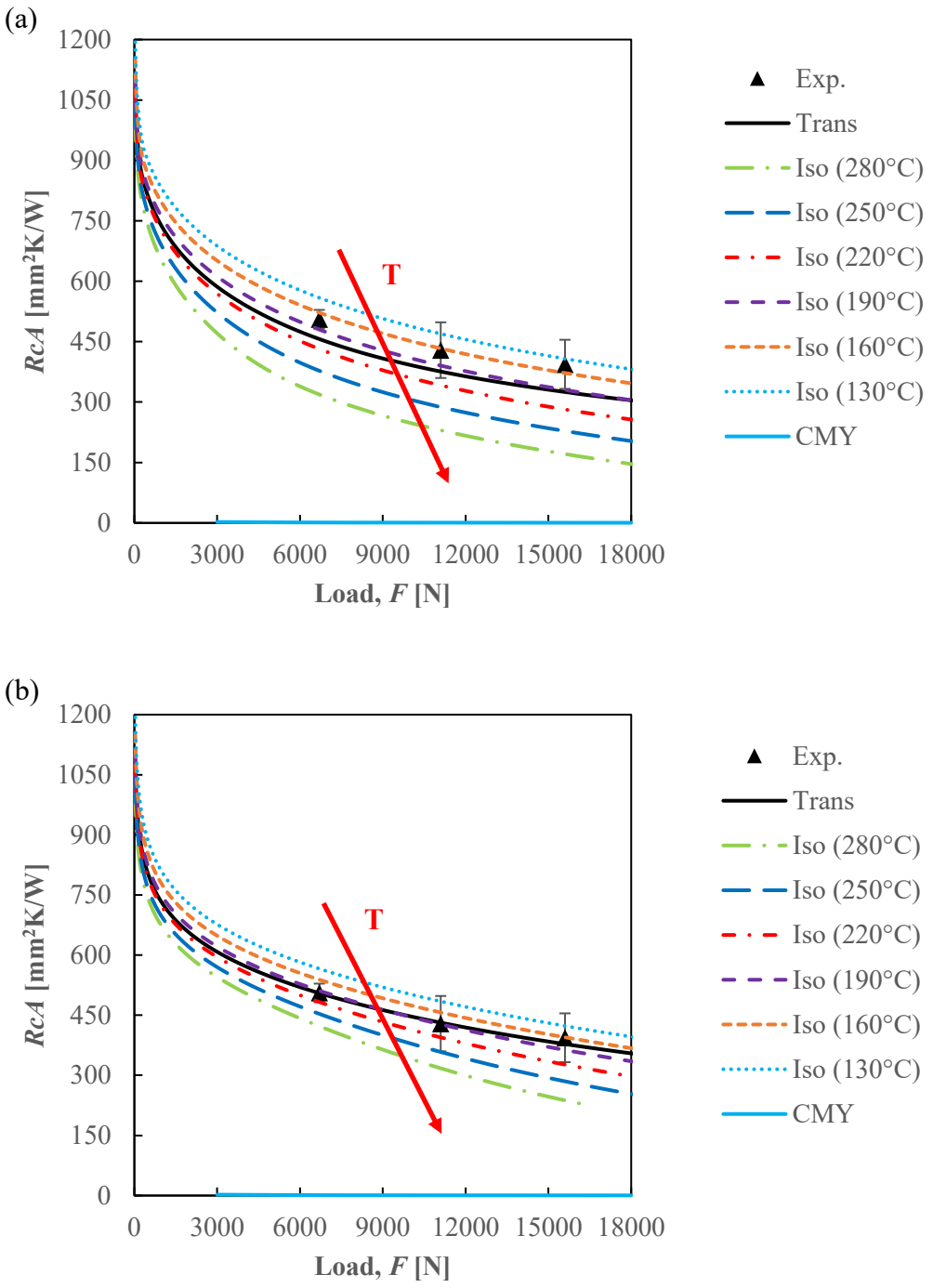


Figure 5. 4 TCR area as a function of contact load for SCF; (a) modified Brake, and (b) modified Brake-ZMC based contact models of hot AA7075 blank indented by cold stainless steel die.

190°C and 220°C match quite well at all experimental data points (Fig. 5.4 (b)).

Additionally, the present models were compared to the CMY model (see cyan solid line in Fig. 5.4 (b)), and it is obvious that the latter significantly underpredicts the experimental data (Caron et al., 2014). The underprediction of CMY model, 1 $mm^2K/W$ for a 6700 N load, is particularly severe and thus could not be utilized to predict TCR area of the HS/DQ process.

#### 5.1.1.1 Summary

From this first analysis, it can be concluded that the prediction by modified Brake model appears poor with respect to the actual experimental indentation depth-load, real contact area-load, and TCR area-load curves. Modified Brake-ZMC shows consistently good predictions, particularly for transient, and isothermal curves at 160°C. In term of accuracy, i.e., the transient curve is preferable as it predicts closer to the mean experimental data points. Thus, in subsequent analyses only transient prediction will be considered.

### 5.1.2 Analysis 2: Effect of asperity radius and contribution of elastic/plastic part

The objective of this second analysis is to examine the influence of different asperity radii on elastic/plastic contributions in both models. For simplicity, SCF contact model is adopted with asperity radius variations between 0.05 mm and 0.08 mm. Take note that the average asperity radius was fixed at r = 0.06698 mm in Analysis 1. Additionally, both pure elastic and pure plastic projections were included under the realization that the current elastoplastic models are the product of elastic and plastic parts.

Figures 5.5 – 5.7 illustrate the effect of different asperity radius and the contribution of elastic and plastic parts in modified Brake and modified Brake-ZMC models. The red arrow with the sign ‘r’ in the figures denotes the direction in which the radius of asperity increases. Result of indentation depth as a function of contact load is shown in Figure 5.5 (a, b) for the two models. The dashed line, solid line, and dashed-dotted line represent pure elastic, elastoplastic, and pure plastic curves, respectively.

Both pure elastic and pure plastic curvatures are calculated from Eqs. 4.57 and 4.61 respectively. For the pure elastic curves, it is discovered that as the asperity radius increases, the indentation depth increases. However, the pure plastic curves exhibit the opposite trend as indicated by the red arrows. Physically, an asperity with a larger radius should have less indentation depth, or in the other words, more loads would be required to deform it to the same indentation depth. This is confirmed by Hertzian elastic sphere-sphere contact model (Eq. 2.8) in which load is proportional to the asperity radius. There is a possibility that Johnson's (1985) elastic cylinder-flat contact model (Eq. 4.3) has an error, as load is demonstrated to be inversely proportional to radius. As a result of this ‘anomalous’ elastic behaviour, elastoplastic predictions are also affected.

The elastoplastic curves of modified Brake model in Fig. 5.5 (a) show a smooth transition from elastic to plastic zone. After reaching the yield point, the curves begin to deviate from pure elastic curves, and progressively transition from ‘anomalous’ elastic trend to ‘normal’ plastic trend at approximately 1000 N. As the deformation progresses into a fully plastic state, the curves converge into a pure plastic projection. As mentioned in Analysis 1, modified Brake model has lower value of fully plastic indentation depth

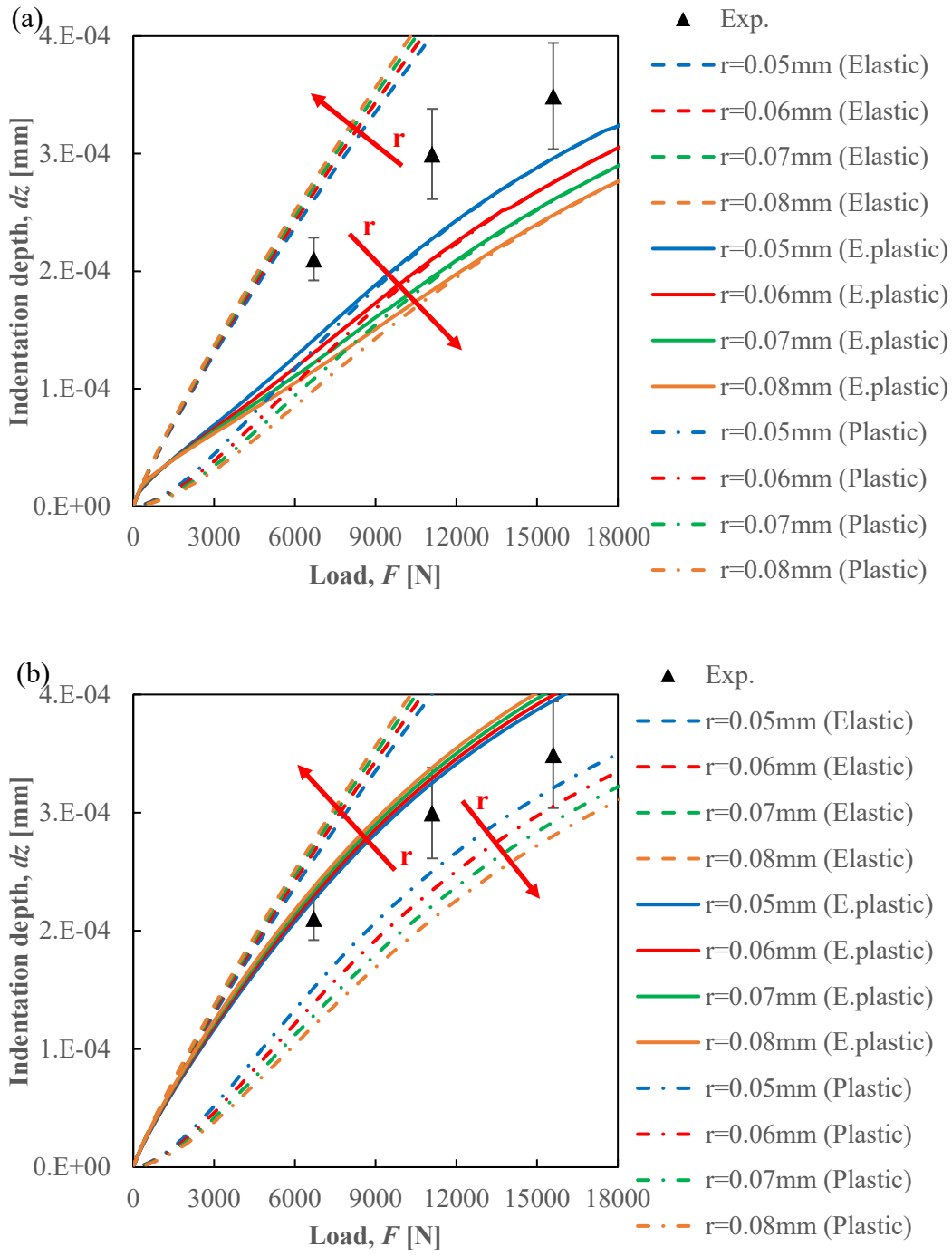


Figure 5. 5 Contact load as a function of indentation depth for SCF; (a) modified Brake, and (b) modified Brake-ZMC contact models of hot AA7075 blank indented by cold stainless steel die.

compared to modified Brake-ZMC, allowing for a considerably faster transition from elastoplastic to fully plastic zone. On the other hand, the elastoplastic curves for modified Brake-ZMC model as depicted in Figure 5.5 (b) exhibit a slower transition and retain a higher proportion of elastic part. This results in the same 'anomalous' elastic tendency for elastoplastic curves.

Many of the modified Brake curves do not agree well with the experimental data. The only curve that has closest proximity to the experimental data is the one with asperity radius, r=0.05 mm with 32.5%, 23.9% and 15.2% errors (compared to the mean experimental indentation depth) for contact loads of 5600 N, 11100 N and 15600 N respectively. Note that the standard deviations for experimental indentation depths at the above loads are ± 8.6%, ± 12.8% and ± 12.9%. On the other hand, modified Brake-ZMC model predicts especially well the curves with lower asperity radius. This suggests that the elastoplastic curves are very sensitive to the values of indentation depth and half contact width in the fully plastic state. The pure plastic projection that utilizes these values according to ZMC method also shows better prediction, in which the curve with asperity radius, r=0.05 mm, has 27.7%, 16.6% and 8.3% errors for respective loads.

The result of real contact area versus contact load are shown in Fig. 5.6. In contradiction to the 'anomalous' trend in indentation depth versus load curve in Figure 5.5, all contact area versus indentation depth curves show an increase in contact area with load as asperity radius increases. This is because a larger radius will likely result in more material flow which will lead to a larger contact patch. It is to be noted that half contact width $b$ is proportional to the contact patch radius as per Eqns. 4.1 and 4.3. In Fig. 5.6 (a),

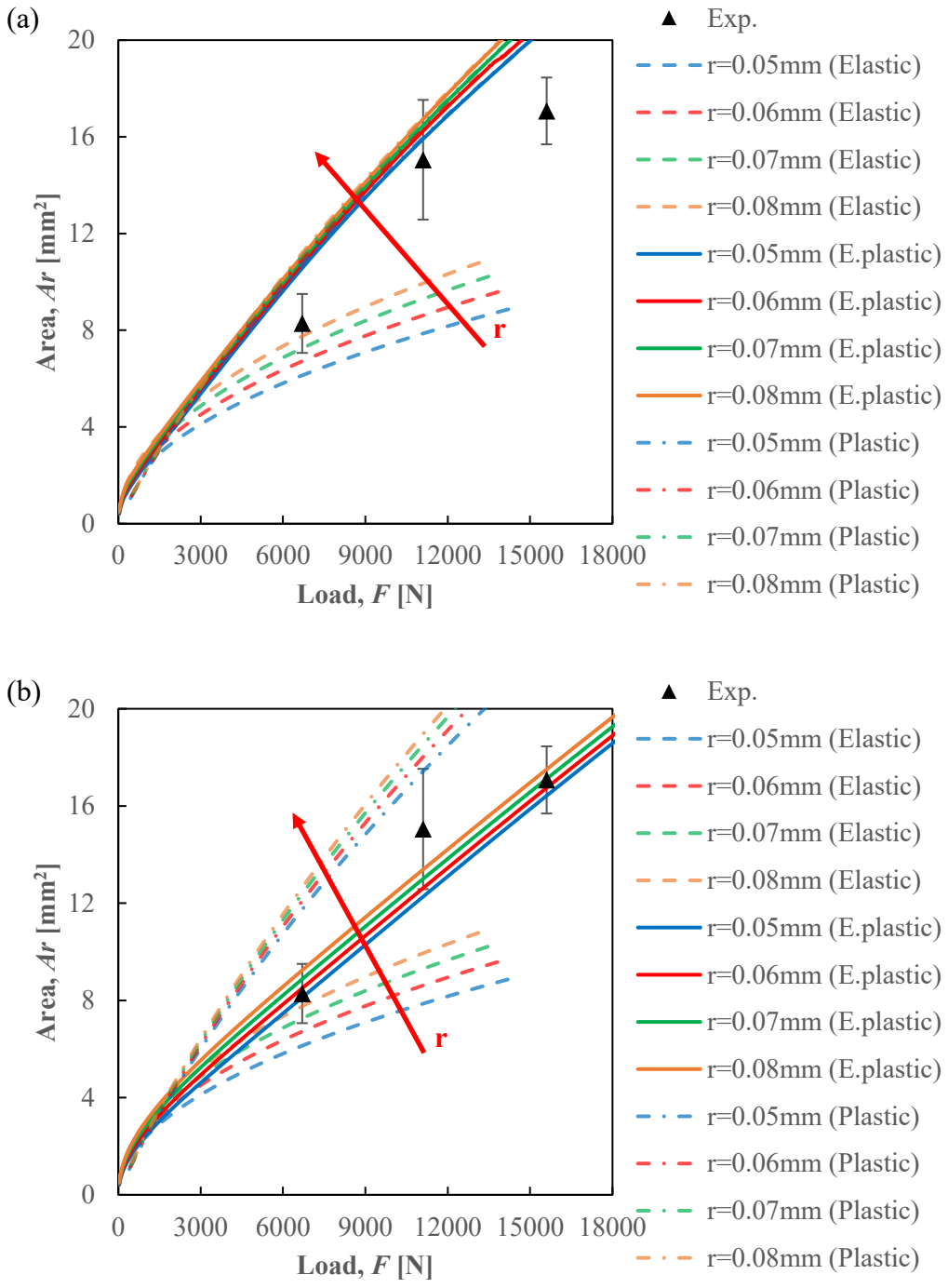


Figure 5. 6 Contact area as a function of contact load for SCF; (a) modified Brake, and (b) modified Brake-ZMC contact models of hot AA7075 blank indented by cold stainless steel die.

it is obvious that pure elastic model underpredicts the experimental data. This is to be expected as elastic deformation offer a higher stiffness, and more loads would be required to increase the contact patch radius. Meanwhile, pure plastic projection overpredicts the experimental data as there is more flow in the plastic region. It is likely that modified Brake curves overlap pure plastic projections due to shorter transition from elastic to plastic region. On the other hand, modified Brake-ZMC model shows better prediction in which its contact area curvatures match well the experimental data points (Fig. 5.6 (b)) due to a longer elastic to plastic transition.

Finally, TCR area as a function of load is presented in Figure 5.7. Similar to Analysis 1, as the load is increased the TCR area decreases drastically at first and slowly after about 5000 N. It is obvious that pure elastic model overpredicts the experimental data, which proves that smaller contact area restricts the heat flow. Thus, TCR area is expected to be higher for elastic prediction and lesser for plastic prediction. Note that there is a truncation at the end of pure elastic curvatures due to restriction of indentation depth up to 4e-4 mm. In Fig. 5.7 (a), modified Brake curvatures overlap pure plastic projections due to shorter transition from elastic to plastic. However, modified Brake has a better match with the experimental data, especially at larger radius values.

In terms of different asperity radius, TCR area is predicted to be higher for larger radius in Figure 5.6. Intuitively, this appears to be contradictory because an increased radius produces a larger contact patch and thus a lower TCR area would be expected. In fact, earlier Eq. 2.46 for sphere-flat contact indicates correctly that TCR is inversely proportion to the contact radius. It is quite likely that there is an error with McGee et al. (1985) where

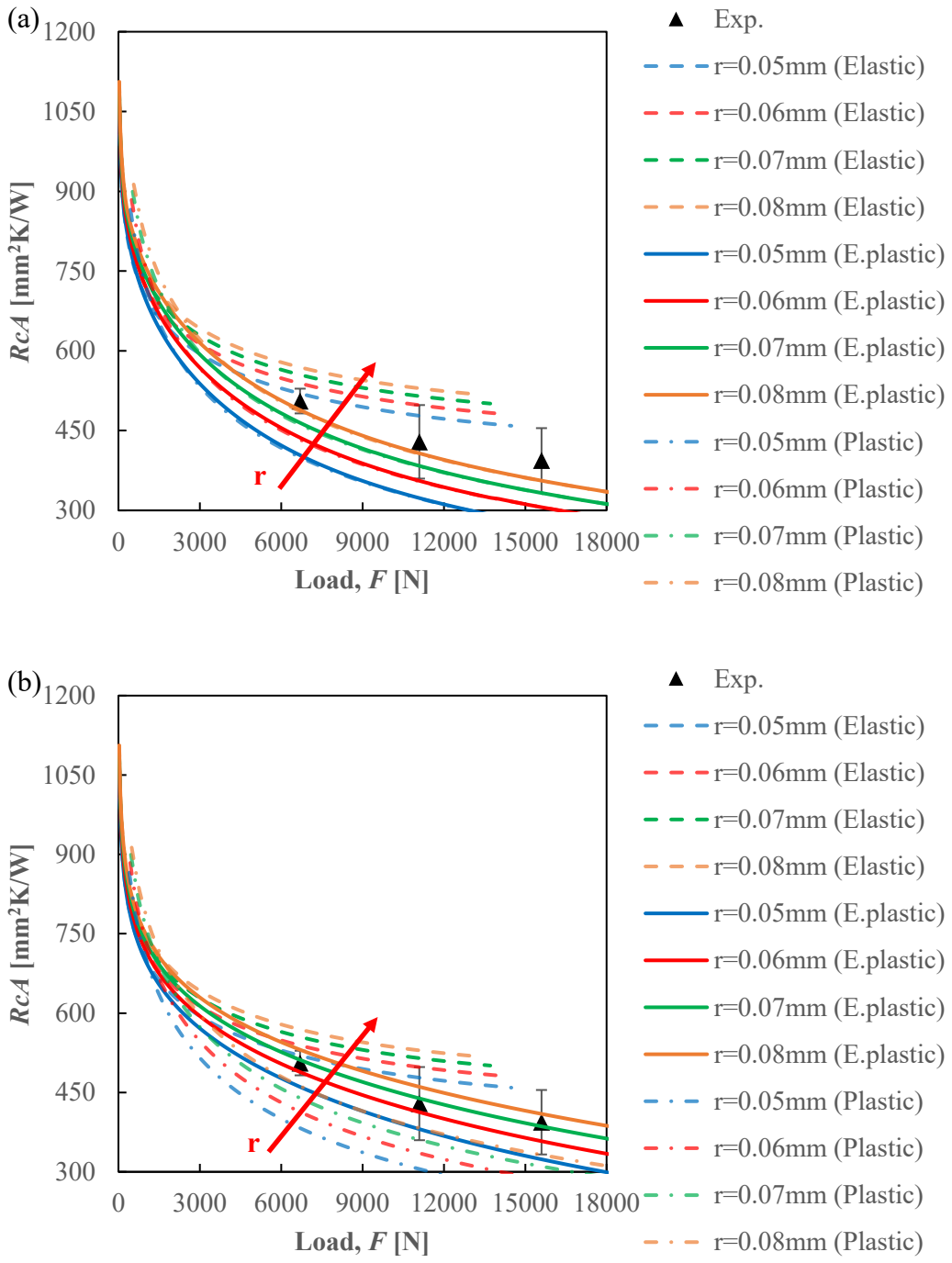


Figure 5. 7 TCR area as a function of contact load for SCF; (a) modified Brake, and (b) modified Brake-ZMC based contact models of hot AA7075 blank indented by cold stainless steel die.

TCR for cylinder-flat contact model (Eq. 4.52) indicates that TCR is proportional to the contact patch radius. This equation is likely influenced by the work of Johnson (1985) where the elastic contact model utilizes the term 'ln 4r/b'. On the other hand, modified Brake-ZMC model shows better prediction in which all curvatures match rather well the experimental data in Fig. 5.7 (b).

#### 5.1.2.1 Summary

To conclude Analysis 2, the elastoplastic curves are greatly affected by the values of half contact width and indentation depth at fully plastic state. There might be an error in Johnson (1985) elastic equation (Eq. 4.3) and McGee et al. (1985) TCR equation (Eq. 4.52), in which indentation depth and TCR area are inversely proportional to the radius respectively. This leads to unexpected trends in indentation depth versus load curves and TCR area versus load curves for different radii.

### 5.1.3 Analysis 3: Effect of order and number of asperities in the distribution

In this analysis, to more accurately account for the asperity height distributions observed on rolled sheet surface, three levels of asperities were considered. This arrangement, also referred to as MCF model earlier, is closer to the real AA7075 blank rolled surface that has asperity distribution in terms of different asperity heights. However, to simplify the analysis, pure plastic projections for both modified Brake and modified Brake-ZMC models are chosen, and the elastic effect is neglected.

The total number of asperities is fixed at 150 asperities according to the experimental profilometer trace, while all asperity radii are set to r = 0.08 mm due to their

excellent prediction in Analysis 2. More than 20 configurations of asperities distribution at different height have been analyzed but, for simplicity, only eleven configurations are presented, which are:

i. 20, 50 and 80 asperities at first, second and third levels, respectively

ii. 20, 80 and 50 asperities at first, second and third level, respectively

iii. 50, 20 and 80 asperities at first, second and third level, respectively

iv. 50, 80 and 20 asperities at first, second and third levels, respectively

v. 80, 20 and 50 asperities at first, second and third level, respectively

vi. 80, 35 and 35 asperities at first, second and third level, respectively

vii. 80, 50 and 20 asperities at first and second level, respectively

viii. 100, 0 and 50 asperities at first, second and third level, respectively

ix. 100, 25 and 25 asperities at first, second and third level, respectively

x. 100, 50 and 0 asperities at first and second level, respectively, and

xi. 150, 0 and 0 asperities at first, second and third level, respectively.

The result of different asperities configurations for both models are shown in Fig. 5.8-5.10. Different patterns of indentation depth curves could be observed in Fig. 5.8, in which the purple curve for uniform asperity (or SCF contact model) is included as a reference. Note that, since there is no elastic contribution here, the asperities deform plastically from the beginning. It is obvious that all curvatures start differently according to the number of asperities at first level. The curves with lower number of asperities at first

level tend to move upward, i.e., to higher indentation depths. This is true as lesser load is required to deform a smaller number of asperities. According to Johnson (1985) and Tabor (1951), the total contact load is the sum of the loads endured by the first level of single asperities. As deformation continues to the second level of asperities, the curves deviate differently in response to the increasing number of asperities.

Similar to the first level, curves with smaller number of asperities have deeper indentation depths. Larger gap between the curves is observed as difference in the number of asperities is larger. Finally, as deformation reaches the third asperity level the curves change its direction again. But the change is not so severe as in the first level. This is because the influence of the number of asperities diminishes at the higher asperity levels. For example, if there are only two levels of asperity distributions such as 100/0/50 and 100/50/0, the curves have only two steps where the former and the latter deviate at F=12000 N and F=4000 N respectively.

Modified Brake model shows good agreement with experimental data especially for the configuration 20/80/50 (Fig. 5.8 (a)). The other curves such as 20/50/80, 50/20/80, 80/20/50 and 100/0/50 configurations only match experimental data at 11100 N and 15600 N. On the other hand, Modified Brake-ZMC model shows better agreement especially for 80/20/50 and 100/0/50 configurations (Fig. 5.8 (b)). The other configurations 20/50/80, 50/20/80, 20/80/50, 80/35/35, 50/80/20, 80/50/20 and 100/25/25 could not match the data at 6700 N. From patterns of both models, it can be said that 80/20/50 and 100/0/50 are more

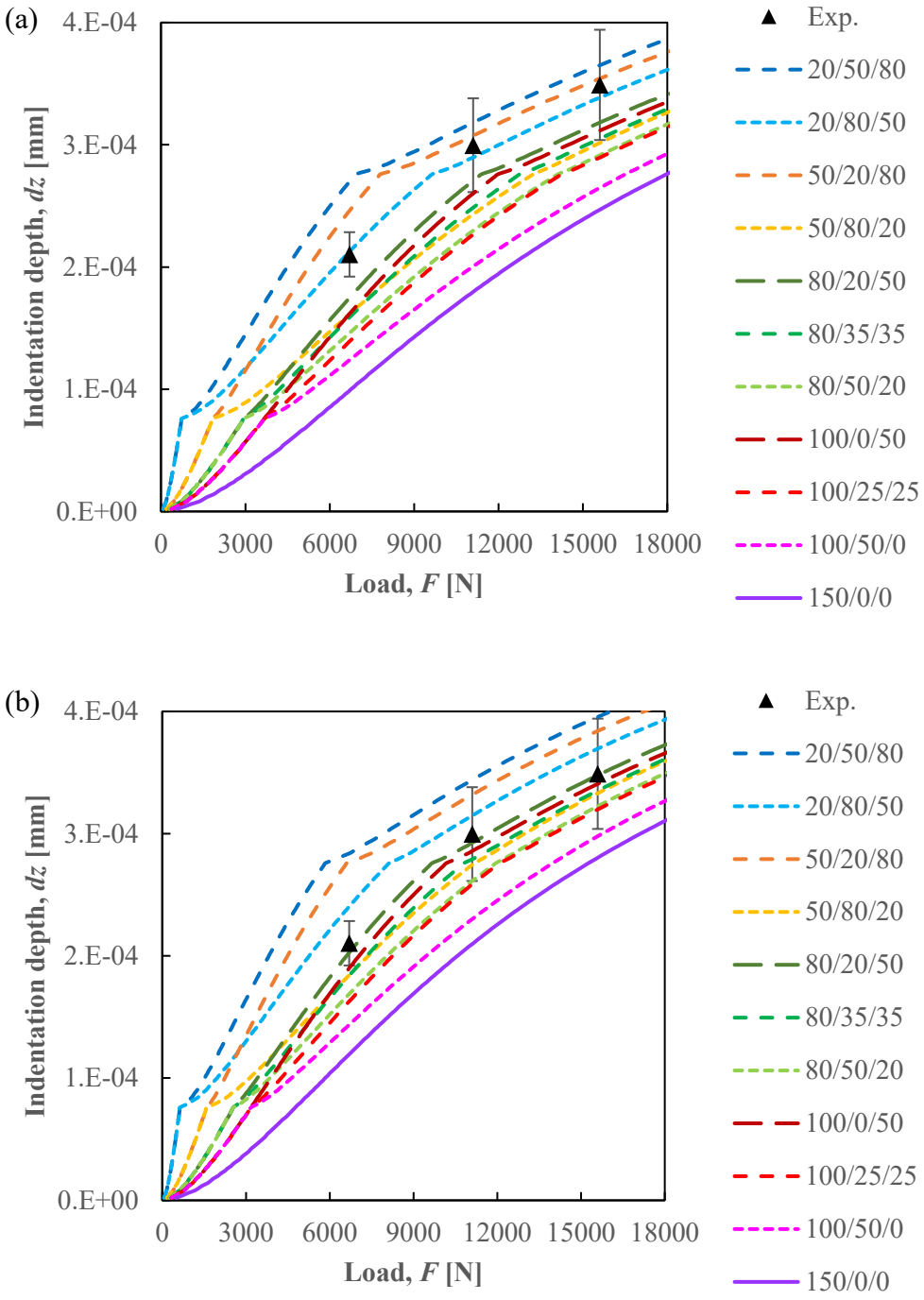


Figure 5. 8 Contact load as a function of indentation depth for MCF; (a) modified Brake, and (b) modified Brake-ZMC contact models of hot AA7075 blank indented by cold stainless steel die.

representative combinations. In addition, the results suggest that the multi-level asperity consideration (MCF model) improves upon the results of the SCF model.

Fig. 5.9 shows curves of real contact area as a function of contact load at different configurations for both modified Brake and modified Brake-ZMC models. Instead of having three significant steps like the previous indentation depth curves, the contact area curvatures increase smoothly with somewhat unrecognized steps. Modified Brake model shows better prediction at three levels compared to one level asperities distribution (Fig. 5.9 (a)). It is found that all curvatures match experimental data at F=11100 N, and, in addition, configurations 50/20/80 and 20/50/80 manage to pass through 6700 N load. However, modified Brake-ZMC did not predict as well since only configurations 20/50/80, 50/20/80 and 100/0/50 matched experimental data at F=11100 N.

Results of TCR area as a function of load for MCF contact model for both models are shown in Fig. 5.10. It is obvious that the asperity distribution greatly affects the shape of the curves. At the beginning, the curves with smaller number of asperities at first level tends to have higher TCR area. Consequently, the curves experience larger drop between the first and second levels. As shown in the Fig. 5.10 (a), configurations 20/50/80 and 50/20/80 could not match experimental data at 6700N due to this shape. Thus, one may omit the lower asperities number such as 20 and 50, at the first level.

As expected, the curves have two or three steps, depending on the number of asperity levels. The modified Brake-ZMC model exhibits a similar tendency for different configurations (Fig. 5.10 (b)). Similar to the modified Brake model, configuration 50/80/20 can be regarded more predictive as it fits all experimental data but has an ‘unsmooth’

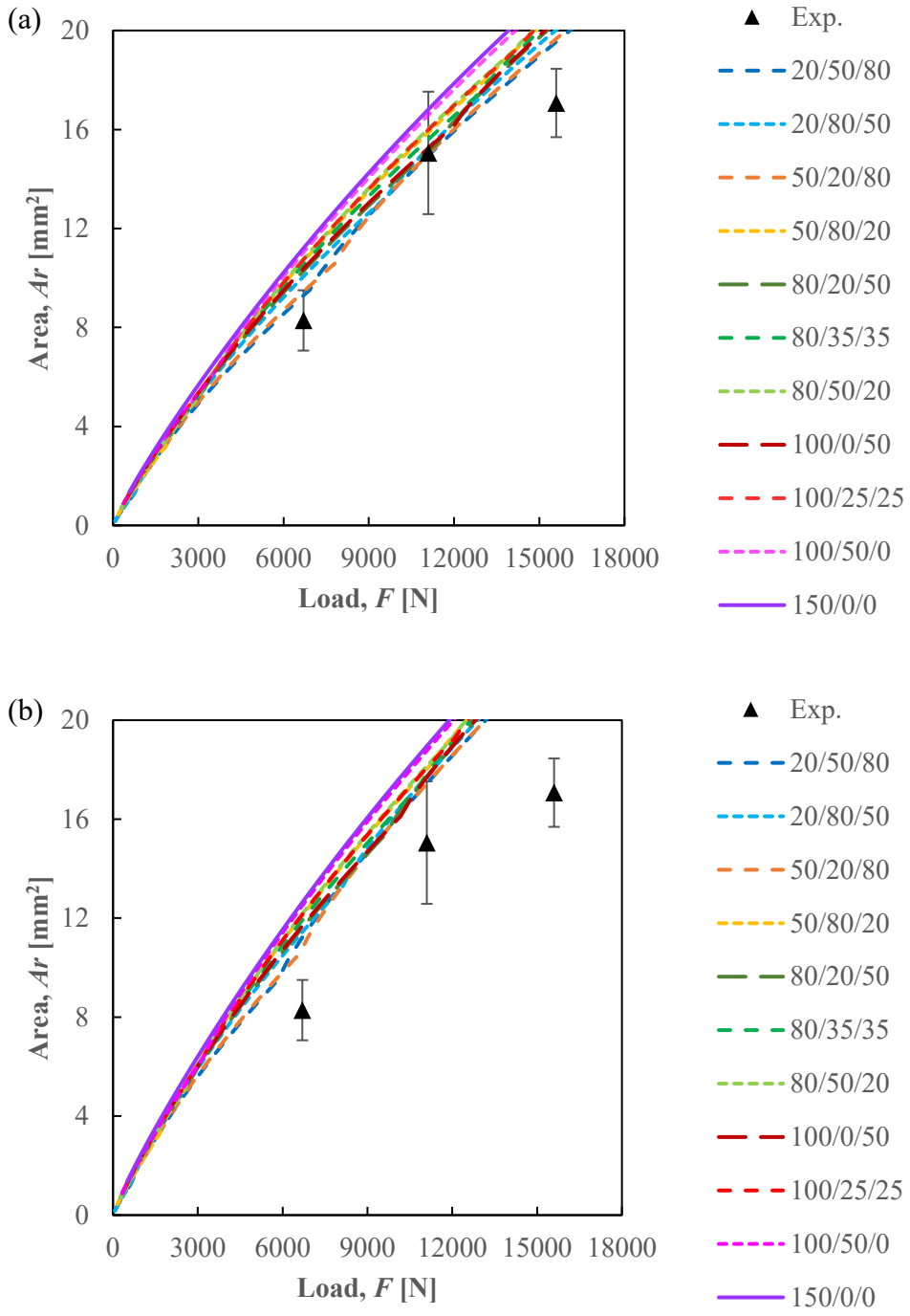


Figure 5. 9 Contact area as a function of contact load for MCF; (a) modified Brake, and (b) modified Brake-ZMC contact models of hot AA7075 blank indented by cold stainless steel die.

beginning. Both models indicate that the configurations 80/35/35, 80/50/20, and 100/25/25 provide the best prediction for multi-level asperities.

#### 5.1.3.1 Summary

In conclusion, the distribution of asperities has a significant effect on the prediction of indentation depth, contact area, and TCR area. The first level is the most dominant as it determines the shape of the curves. This effect gradually diminishes in the subsequent levels. It is recommended not to use lower number of asperities in the first level. The best configuration should have higher number at the first level and the number of asperities could be gradually decreased (or kept equal) at subsequent levels. This is contrary to the Gaussian asperities distribution in which asperities number should be the least at the first level with gradually increases at subsequent levels. Note that Gaussian distribution has been widely used by the followers of work of Greenwood & Williamson (1966).

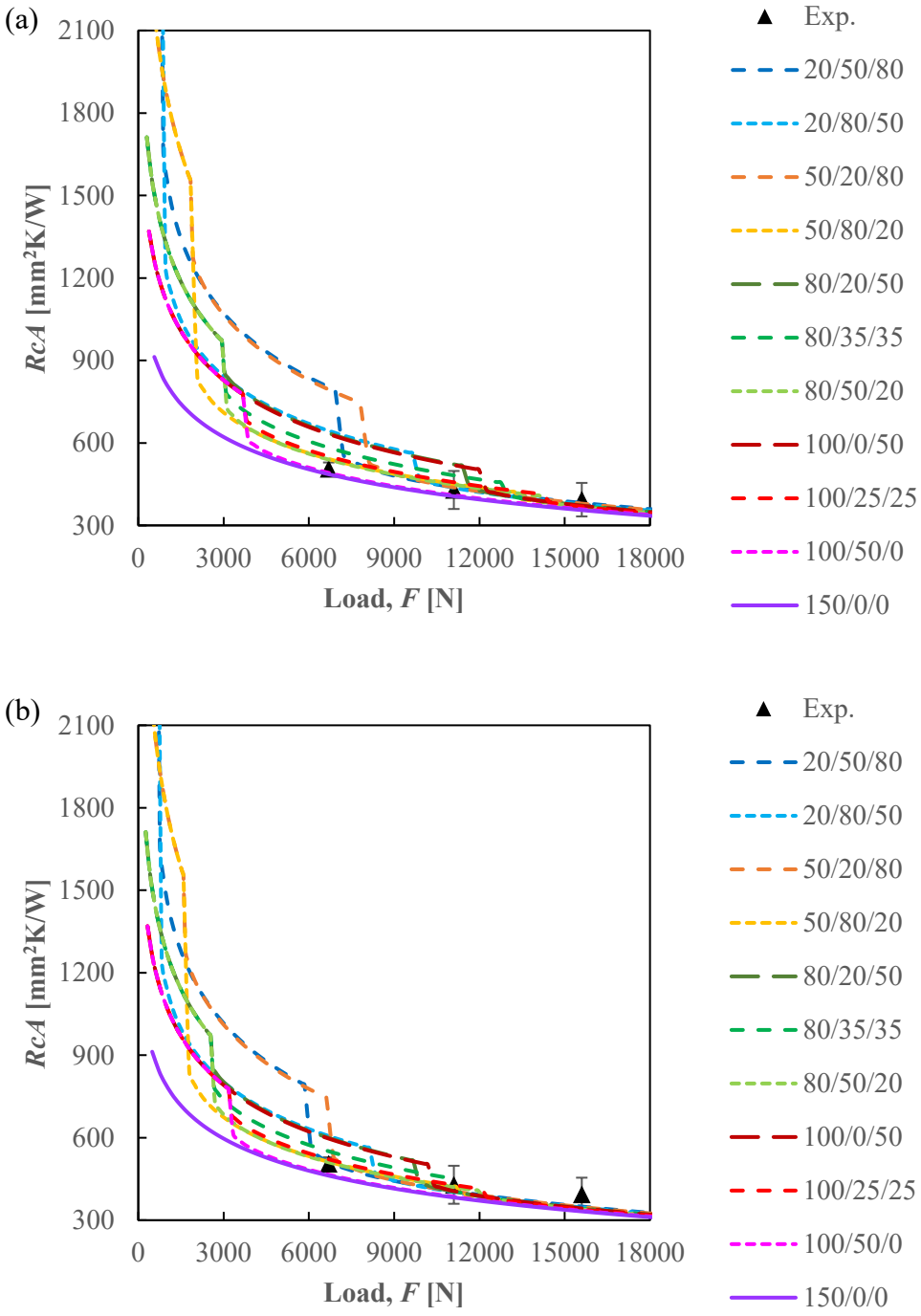


Figure 5. 10 TCR area as a function of contact load for MCF; (a) modified Brake, and (b) modified Brake-ZMC based contact models of hot AA7075 blank indented by cold stainless steel die.

### 5.2 Effect of air gaps and radiation resistances

In this sub-section, the effect of air gaps and radiation resistances are discussed for their contributions to the total TCR area value. This study was carried out to assess if these two resistance contributions should be also considered in the Analyses 1, 2, and 3. Both modified Brake and modified Brake-ZMC models are compared for three cases involving:

i. Only solid to solid or constriction resistance ($R_c$),

ii. Only Rc and air gaps resistance ($R_{air}$), and

iii. All three resistances; $R_c$, $R_{air}$ and radiation resistance ($R_r$)

SCF contact model with asperities radius of 0.08 mm is chosen for simplicity. The parallel flux-tube model (PFTM) is used because it is the most accurate model for the resistance of air gaps. This computation is carried out using Eqs. 4.58, 4.59, and 4.60, with the air and radiation-related parameters listed in Table 5.3. These equations are multiplied with nominal contact area (78.54 $mm^2$) so the unit is $mm^2K/W$ and comparable to existing literature (reciprocal IHTC).

Table 5.3 Input for calculation of resistances (r = 0.08 mm).

| Properties | Value |
|---|---|
| Thermal conductivity of air, $k_{air}$ | 1E-04+9.79E-05T-3.68E-08$T^2$ |
| Thermal accomm. coef. of cylinder-air, $\alpha_{C,air}$ | 0.96 |
| Thermal accomm. coef. of flat-air, $\alpha_{F,air}$ | 0.90 |
| Ratio of specific heats of the air, $\gamma$ | 1.4 |
| Mean free path of air, $\lambda$ | 6.85E-08 m |
| Prandtl number of air | 0.71 |
| Emissivity of flat, $\varepsilon_F$ | 0.07 |
| Emissivity of cylinder, $\varepsilon_C$ | 0.5 |
| Stefan-Boltzmann constant, $\sigma$ | 4.57E-08 $W/m^2K^4$ |

Figure 5.11 presents a comparison between the three cases of TCR area as a function of load. As the load is increased, all curves decrease non-linearly. It is also evident that that both $R_c$-$R_{air}$-$R_r$ curves and $R_c$-$R_{air}$ curves overlap each other. This implies that radiation resistance is rather large, and thus has negligible effect in the IHTC prediction. As mentioned by Bahrami et al., (2006), radiation resistance could be neglected if the temperature is less than 700 K. This is because there are discrepancies between $R_c$ curves and the other curves due to higher contribution of conduction through air gaps at lower load. After a pressing load of 6000 N, all curves merge into each other. As conclusion, since hot stamping process often deals with higher applied pressures (or applied loads), the contribution of both air gaps and radiation could be neglected.

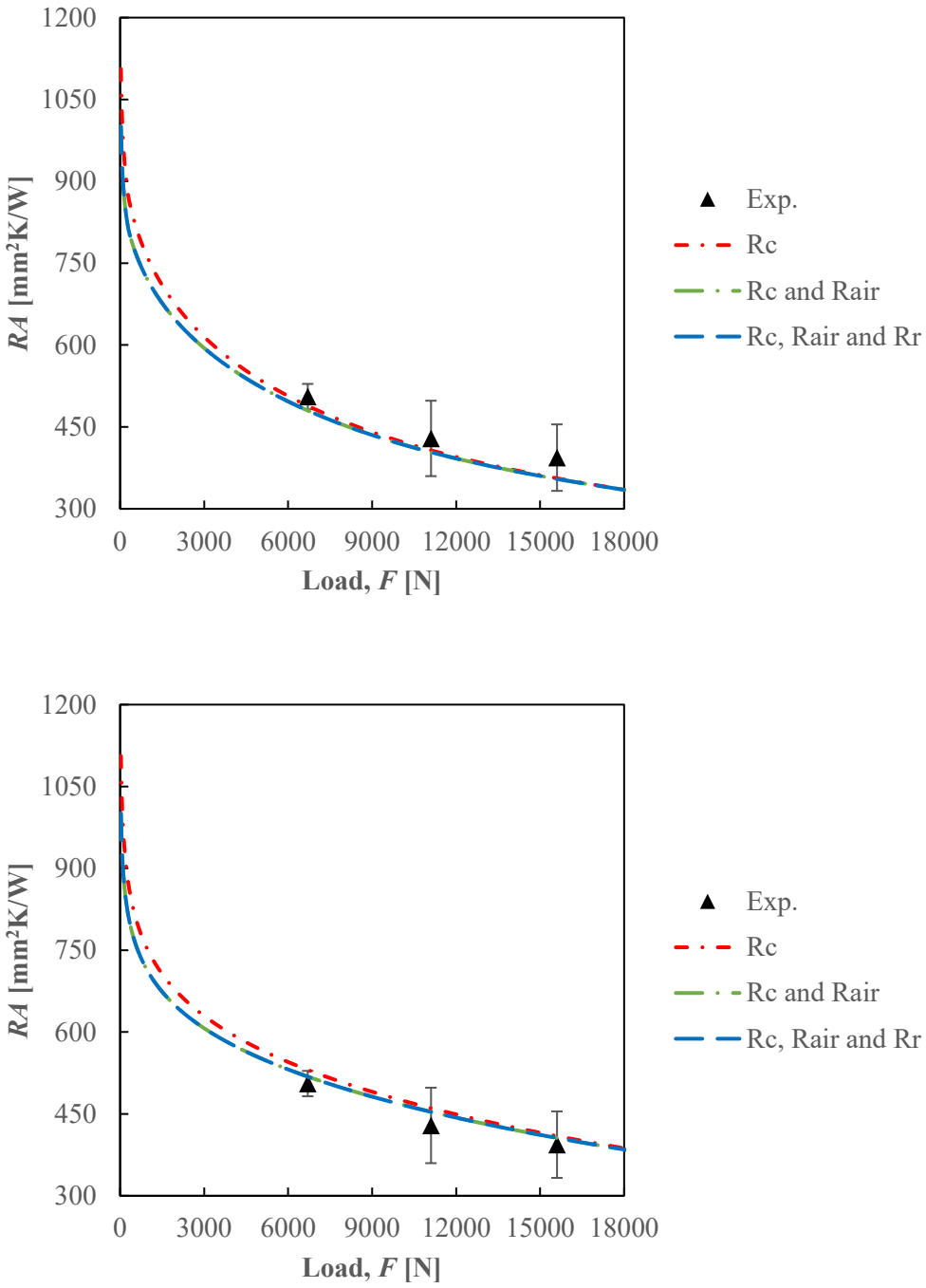


Figure 5. 11 TCR area as a function of contact load for SCF; (a) modified Brake, and (b) modified Brake-ZMC based contact models of hot AA7075 blank indented by cold stainless steel die.

### 5.3 Interaction between neighboring asperities

Finally, it is necessary to justify the assumption that there is no interaction between neighbouring asperities during the contact between the rigid flat stainless steel die and the elastoplastic flat AA7075 surfaces. In Fig. 5.12, before deformation (upper part of sketch) and after deformation (lower part of sketch) are compared, in which rigid flat smooth surface is in contact with elastoplastic flat rough surface. It should be noted that the scale of the y-axis in this graphic is ten times that of the x-axis. There are only three asperities along 0.2 mm length on the surface as per the earlier proportionality of total asperities in this study of 150 asperities per 10 mm length. The terms '2b', '2c' and 'd' correspond to contact width after deformation, segment diameter of cylindrical asperities prior to deformation, and the proximity space between asperities, respectively.

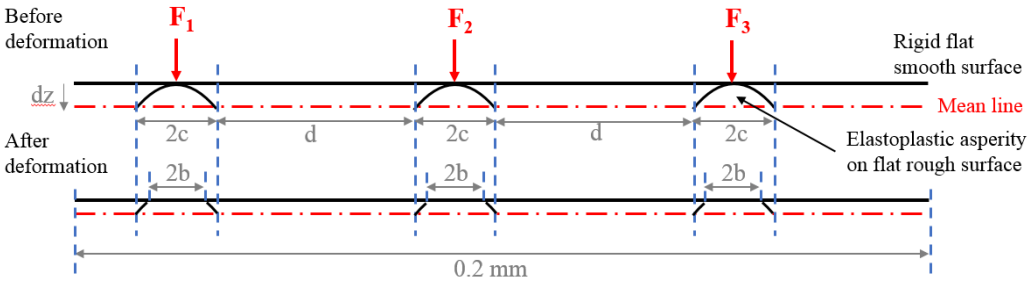


Figure 5. 12 Multi-cylindrical asperities in contact with flat smooth surface (SCF model): before (upper part of sketch) and after (lower part of sketch) deformations.

As load ($F=F_1+F_2+F_3+..+F_n$) is increased, indentation depth (dz) and contact width (2b) increase and the asperities deform through Hertzian elastic, elastoplastic, and plastic deformations. In the case of asperity radius r = 0.08 mm, the initial values for '2c' and '2d' are 0.020 mm and 0.046 mm respectively. After the maximum depth of dz =

0.0004 mm, it is found that the contact width (2b) is 0.014 mm for modified Brake-ZMC and 0.033 mm for modified Brake models. It is to be noted that the difference in contact width between these two models is related to the deformation region at dz = 0.0004 mm, which is in the elastoplastic region for the former and the plastic region for the latter. In any case, a comparison of the asperity to asperity proximity distance (d) reveals that the contact width values are indeed small to warrant any asperity interaction.

To conclude, the assumption utilized in the model development that there is no interaction between asperities during the asperity deformation is reasonable.

**5.4 Summary**

In this chapter, asperity deformation based model characteristics of two different models are presented and analyzed. Also, the model results for hot AA7075 sheet in contact with the stainless steel die are predicted and compared with the experimental results. Among the two models, modified Brake-ZMC model yields generally good prediction of the experimental data compared to the modified Brake model. This is the result of fully plastic value in the elastoplastic equations. Additionally, the number of asperity levels, the configuration of asperities distribution, and the asperity radius all significantly affect the predictions. A more comprehensive study of the above parameters should be carried out in the future.

# Chapter 6

## Conclusions

Two different cylinder-flat asperity contact models have been developed based on the works of Brake (2015) and Zhao et al. (2000) for spherical contact, in the context of heat transfer between hot AA7075 flat sheet with rolled asperities and a cold flat and smooth stainless steel die during the hot stamping process. The model results have been assessed with the laboratory-based experimental results. The conclusions for each of the three objectives as stated in Chapter 1 are presented below.

### 6.1 Development of asperity flattening model by considering a contact between an elastoplastic, flat, rough hot AA7075 surface (with multi-asperity cylinder segments) and a rigid, flat, smooth cold die stainless steel surface

Two new mechanistic models of asperity contact and flattening referred to as Modified Brake and modified Brake-ZMC models, have been developed. The modified models include many new aspects to bring them closer to their applicability to capture the heat transfer characteristics during the AA7075 hot stamping process. The modifications include incorporation of topography of the rolled sheet in the form of cylinders of different radii and height distributions, conservation of volume during the plasticity phase of asperity deformation, and incorporation of non-linear work hardening characteristics of AA7075 sheet. Both models have some similarities in the manner in which strain hardening is applied in elastoplastic equation according to Brake method. The differences are in the

values of the half contact width and the indentation depth at fully plastic region. It is found that the modified Brake model reaches the fully plastic state much earlier than the modified Brake-ZMC model. This leads to different predictions of load-indentation depth and area-load curves.

In the first analysis, the isothermal predictions over the temperature range of 130°C to 280°C are compared to the transient prediction. It is revealed that as the temperature is increased, both indentation depths and contact areas increase. Transient curve passes through isothermal curves between 220°C and 190°C for modified Brake model whereas 220°C and 160°C for modified Brake-ZMC model.

The second study reveals a smooth transition between elastic and plastic curvatures in elastoplastic curves. Full transition from elastic to plastic state is clearly seen in modified Brake prediction since its fully plastic critical point is around 2.5E-04 mm, which is within the overall deformation, i.e., 4E-04 mm. However, there is an anomalous elastic behavior in which the indentation depth increases as the asperity radius increases.

In the third analysis, it is obvious that the plastic curves from both models have multi-steps depending on the number of asperities levels. Expectedly, as the number of asperities decrease the contact area decreases, and the indentation depth increases. The first level is the most dominant that determine the shape of the curves. This effect gradually diminishes in the subsequent levels. Thus, it is not recommended to use a lower number of asperities in the first level for the modelling. A Gaussian asperities distribution proposed

by Greenwood & Williamson (1966) may not be the most appropriate approach for modeling the asperity flattening process.

Overall, modified Brake-ZMC transient elastoplastic model shows consistently good predictions with the experimental data and thus could be used in FE to predict the indentation depth and real contact area as a function of load.

**6.2 Determination of thermal contact resistance (TCR) from the surface contact models and other existing model in the literature.**

The second objective is an extension of the first objective. After the half contact width is known, it could be used for determining the TCR area. It is found that as load is increased the contact area becomes larger and more heat could be transferred across the interface from hot AA7075 sheet to the cold stainless steel die. Consequently, TCR area decreases. Temperature has a strong influence in increasing the ductility of the material. Higher temperature results in a larger contact area which subsequently results in a lower TCR area.

In a separate analysis, TCR area was found to be larger for asperities of larger radius. This is contradictory to the general understanding of asperity flattening since a larger asperity radius should lead to a larger contact area and thus more heat flow could be transferred across the interface lowering the TCR area.

In comparing the contribution of solid-solid resistance, air gaps resistance and radiation resistance, it is found that radiation resistance is too high and does not have a significant effect in the prediction of TCR area values. At lower applied loads the air gaps resistance exists but it diminishes after a load of about 6000 N. Beyond this point, all TCR

area curves merge with solid-solid resistance curve, and thus effect of air gaps and radiation resistances can be neglected in the prediction of TCR area.

In author opinion, the prediction of TCR-load by modified Brake-ZMC transient elastoplastic model is impressive compared to the experimental data, and the model could be used in FE by tool and die manufacturers. Manufacturers will no longer have to worry about embedding thermocouples in complex-shaped stamping dies, punches, or even thin blanks by employing this mechanistic method.

### 6.3 Comparison of the mechanistic model results with hot pressing experimental results on AA7075 aluminum blank with a cold planar stainless steel die

A series of hot pressing experiments at different loads have been successfully conducted and experimental results compared with the model results. Experimental TCR area data was obtained from the temperature measurements within hot AA7075 blanks and cold stainless steel die, and predicted heat flux between the contacting surfaces. This interfacial heat flux was predicted by using Beck's inverse heat conduction method.

These experiments and subsequent experimental analysis of heat flux, punch load versus indentation depth and punch loads versus contact area provided a good set of data for a broad comparison with the model results. While both of the proposed new mechanistic models of asperity flattening, modified Brake and modified Brake-ZMC, provided results and trends largely similar to the experiments, the modified Brake-ZMC model yielded better agreement with the experimental data compared to the modified Brake model.

## 6.4 Recommendations and Future Work

(i) This work was focused on planar sheet and die contact, whereas in hot stamping application, many other tool geometric features with curves are involved. Thus, it is recommended that the future mechanistic modeling work could be extended to contact between curved AA7075 sheet and stainless steel die surfaces.

(ii) In modified Brake-ZMC model, the indentation depth at fully plastic is based on experimental work on sphere-sphere contact. It would be useful to conduct further experimental work on cylinder-flat contact to determine indentation depth at fully plastic state. The present modeling study reveals that there is scope to improve Johnson (1985) elastic and McGee et al. (1985) TCR equations for cylinder-flat contact as these equations exhibit 'anomalous' behavior as discussed in the present work.

(iii) In Chapter 2, the role of lubrication in HS/DQ process has been discussed. Lubrication is commonly used to prevent scratches while forming and to enhance heat transfer from a hot AA7075 blank to a cold stainless steel die. However, since this study is primarily concerned with asperity flattening models, lubrication is disregarded. Therefore, it is recommended to include lubrication effect in the future mechanistic modeling work.

# References

Abdulhay, B., Bourouga, B., & Dessain, C. (2011). Experimental and theoretical study of thermal aspects of the hot stamping process. *Applied Thermal Engineering*, *31*(5), 674–685. https://doi.org/10.1016/j.applthermaleng.2010.11.010

Adams, G. G., & Nosonovsky, M. (2000). Contact modeling - forces. *Tribology International*, *33*(5), 431–442. https://doi.org/10.1016/S0301-679X(00)00063-3

Bahadur, V., Xu, J., Liu, Y., & Fisher, T. S. (2005). Thermal resistance of nanowire-plane interfaces. *Journal of Heat Transfer*, *127*(6), 664–668. https://doi.org/10.1115/1.1865217

Bahrami, M., Culham, J. R., Yananovich, M. M., & Schneider, G. E. (2006). Review of thermal joint resistance models for nonconforming rough surfaces. *Applied Mechanics Reviews*, *59*(1–6), 1–11. https://doi.org/10.1115/1.2110231

Bahrami, M., Yovanovich, M. M., & Culham, J. R. (2004). Thermal joint resistances of nonconforming rough surfaces with gas-filled gaps. *Journal of Thermophysics and Heat Transfer*, *18*(3), 326–332. https://doi.org/10.2514/1.5482

Barber, J. ., & Ciavarella, M. (2000). Contact mechanics. *International Journal of Solids and Structures*, *37*(1–2), 29–43. https://doi.org/10.1016/S0020-7683(99)00075-X

Beck, J. V., Blackwell, B., & St. Clair, C. R., J. (1985). *Inverse Heat Conduction: Ill Posed Problems*. Wiley Interscience, New York.

Bhushan, B. (1998). Contact mechanics of rough surfaces in tribology: Multiple asperity contact. *Tribology Letters*, *4*(1), 1–35. https://doi.org/10.1023/A:1019186601445

Blaise, A., Bourouga, B., Abdulhay, B., & Dessain, C. (2013). Thermal contact resistance estimation and metallurgical transformation identification during the hot stamping. *Applied Thermal Engineering*, *61*(2), 141–148. https://doi.org/10.1016/j.applthermaleng.2013.07.041

Bosetti, P., Bruschi, S., Stoehr, T., Lechler, J., & Merklein, M. (2010). Interlaboratory comparison for heat transfer coefficient identification in hot stamping of high strength steels. *International Journal of Material Forming*, *3*(SUPPL. 1), 817–820. https://doi.org/10.1007/s12289-010-0895-9

Brake, M. R. W. (2015). An analytical elastic plastic contact model with strain hardening and frictional effects for normal and oblique impacts. *International Journal of Solids and Structures*, *62*, 104–123. https://doi.org/10.1016/j.ijsolstr.2015.02.018

Bruschi, S., Altan, T., Banabic, D., Bariani, P. F., Brosius, A., Cao, J., Ghiotti, A., Khraisheh, M., Merklein, M., & Tekkaya, A. E. (2014). Testing and modelling of material behaviour and formability in sheet metal forming. *CIRP Annals - Manufacturing Technology*, *63*, 727–749. https://doi.org/10.1016/j.cirp.2014.05.005

Burte, P. R., Im, Y.-T., Altan, T., & Semiatin, S. L. (1990). Measurement and Analysis of Heat Transfer and Friction During Hot Forging. *Journal of Engineering for Industry*, *112*(March 1989), 332. https://doi.org/10.1115/1.2899596

Caron, E., Daun, K. J., & Wells, M. A. (2013). Experimental characterization of heat

transfer coefficients during hot forming die quenching of boron steel. *Metallurgical and Materials Transactions B: Process Metallurgy and Materials Processing Science*, *44*(2), 332–343. https://doi.org/10.1007/s11663-012-9772-x

Caron, E. J. F. R., Daun, K. J., & Wells, M. A. (2014). Experimental heat transfer coefficient measurements during hot forming die quenching of boron steel at high temperatures. *International Journal of Heat and Mass Transfer*, *71*, 396–404. https://doi.org/10.1016/j.ijheatmasstransfer.2013.12.039

Carslaw., H. S., & Jaeger, J. C. (1959). *Conduction of Heat in Solids*.

Chang, W. R., Etsion, I., & Bogy, D. B. (1987). An Elastic-Plastic Model for the Contact of Rough Surfaces. *Journal of Tribology*, *109*(2), 257–263. https://doi.org/10.1115/1.3261348

Chang, Y., Li, S., Li, X., Wang, C., Hu, P., & Zhao, K. (2016). Effect of contact pressure on IHTC and the formability of hot-formed 22MnB5 automotive parts. *Applied Thermal Engineering*, *99*, 419–428. https://doi.org/10.1016/j.applthermaleng.2016.01.053

Chang, Y., Li, X., Wang, C., Zheng, G., Ren, D., Hu, P., & Dong, H. (2017). Determination of interfacial heat transfer coefficient and analysis of influencing factors in warm forming the third-generation automotive medium-Mn steel. *International Communications in Heat and Mass Transfer*, *86*(2), 108–116. https://doi.org/10.1016/j.icheatmasstransfer.2017.05.001

Cola, B. A., Xu, J., & Fisher, T. S. (2009). Contact mechanics and thermal conductance

of carbon nanotube array interfaces. *International Journal of Heat and Mass Transfer*, *52*(15–16), 3490–3503. https://doi.org/10.1016/j.ijheatmasstransfer.2009.03.011

Cooper, M. G., Mikic, B. B., & Yovanovich, M. M. (1969). Thermal contact conductance. *International Journal of Heat and Mass Transfer*, *12*(3), 279–300. https://doi.org/10.1016/0017-9310(69)90011-8

Das, A. K., & Sadhal, S. S. (1999). Thermal constriction resistance between two solids for random distribution of contacts. *Heat and Mass Transfer*, *35*(2), 101–111. https://doi.org/10.1007/s002310050303

Eaton, P., & West, P. (2010). *Atomic force microscopy*. Oxford University Press, Oxford.

Eugene, R. (1953). Stress Distribution and Strength Condition of Two Rolling Cylinders Pressed Together. *University of Illinois Bulletin*, *50*(44). https://doi.org/http://hdl.handle.net/2142/4380

Fletcher, L. S., & Gyorog, D. A. (1971). *Heat Transfer Between Surfaces in Contact : an Analytical and Experimental Study of Thermal Contact Resistance of Metallic Interfaces*.

Geiger, M., Merklein, M., & Lechler, J. (2008). Determination of tribological conditions within hot stamping. *Production Engineering*, *2*(3), 269–276. https://doi.org/10.1007/s11740-008-0110-8

Greenwood, J. A., Putignano, C., & Ciavarella, M. (2011). A Greenwood & Williamson theory for line contact. *Wear*, *270*(3–4), 332–334.

https://doi.org/10.1016/j.wear.2010.11.002

Greenwood, J. A., & Tripp, J. H. (1970). The Contact of Two Nominally Flat Rough Surfaces. *Proceedings of the Institution of Mechanical Engineers*, *185*(1), 625–633. https://doi.org/10.1243/PIME_PROC_1970_185_069_02

Greenwood, J. A., & Williamson, J. B. P. (1966). Contact of nominally flat surfaces. *Proceedings of the Royal Society of London. Series A. Mathematical and Physical Sciences*, *295*(1442), 300–319. https://doi.org/10.1098/rspa.1966.0242

Handzel-Powierza, Z., Klimczak, T., & Polijaniuk, A. (1992). On the experimental verification of the Greenwood-Williamson model for the contact of rough surfaces. *Wear*, *154*(1), 115–124. https://doi.org/10.1016/0043-1648(92)90247-6

Harrison, N. R., & Luckey, S. G. (2014). Hot Stamping of a B-Pillar Outer from High Strength Aluminum Sheet AA7075. *SAE International Journal of Materials and Manufacturing*, *7*(3), 2014-01–0981. https://doi.org/10.4271/2014-01-0981

Hertz, H. (1881). On the contact of Elastic Solids. *Journal Fur Die Reine Und Angewandie Mathematic*, *92*, 156–171.

Horng, J. H. (1998). An Elliptic Elastic-Plastic Asperity Microcontact Model for Rough Surfaces. *Journal of Tribology*, *120*(1), 82–88. https://doi.org/10.1115/1.2834194

Hu, P., Ying, L., Li, Y., & Liao, Z. (2013). Effect of oxide scale on temperature-dependent interfacial heat transfer in hot stamping process. *Journal of Materials Processing Technology*, *213*(9), 1475–1483. https://doi.org/10.1016/j.jmatprotec.2013.03.010

Hung, T.-H., Tsai, P.-W., Chen, F.-K., Huang, T.-B., & Liu, W.-L. (2014). Measurement of Heat Transfer Coefficient of Boron Steel in Hot Stamping. *Procedia Engineering*, *81*(October), 1750–1755. https://doi.org/10.1016/j.proeng.2014.10.226

INCO. (1963). *Report No. INCO-2980*.

Jackson, R. L. (2018). A solution of rigid perfectly plastic cylindrical indentation in plane strain and comparison to elastic-plastic finite element predictions with hardening. *Journal of Applied Mechanics, Transactions ASME*, *85*(2). https://doi.org/10.1115/1.4038495

Ji, K., Liu, X., El Fakir, O., Liu, J., Zhang, Q., & Wang, L. (2016). Determination of the Interfacial Heat Transfer Coefficient in the Hot Stamping of AA7075. *Manufacturing Review*, *3*, 16. https://doi.org/https://doi.org/10.1051/mfreview/2016017

Johnson, K. L. (1982). One Hundred Years of Hertz Contact. *Proceedings of the Institution of Mechanical Engineers*, *196*(1), 363–378. https://doi.org/10.1243/PIME_PROC_1982_196_039_02

Johnson, K. L. (1985). *Contact mechanics*. Cambridge University Press, Cambridge.

Keci, A., Harrison, N. R., & Luckey, S. G. (2014). Experimental evaluation of the quench rate of AA7075. *SAE Technical Papers*, *1*. https://doi.org/10.4271/2014-01-0984

Kogut, L., & Etsion, I. (2003). A finite element based elastic-plastic model for the contact of rough surfaces. *Tribology Transactions*, *46*(3), 383–390. https://doi.org/10.1080/10402000308982641

Lankarani, H. M., & Nikravesh, P. E. (1994). Continuous contact force models for impact analysis in multibody systems. *Nonlinear Dynamics*, *5*(2), 193–207. https://doi.org/10.1007/BF00045676

Laraqi, N., & Bairi, A. (2002). Theory of thermal resistance between solids with randomly sized and located contacts. *International Journal of Heat and Mass Transfer*, *45*(20), 4175–4180. https://doi.org/10.1016/S0017-9310(02)00127-8

Liu, X., Fakir, O. El, Meng, L., Sun, X., Li, X., & Wang, L. (2017). Effects of lubricant on the IHTC during the hot stamping of AA6082 aluminium alloy: experimental and modelling studies. *Journal of Materials Processing Technology*, *2010*. https://doi.org/10.1016/j.jmatprotec.2017.12.013

Liu, X., Ji, K., Fakir, O. El, Fang, H., Gharbi, M. M., & Wang, L. L. (2017). Determination of the interfacial heat transfer coefficient for a hot aluminium stamping process. *Journal of Materials Processing Technology*, *247*(March), 158–170. https://doi.org/10.1016/j.jmatprotec.2017.04.005

Liu, Y., Zhu, B., Wang, Y., Li, S., & Zhang, Y. (2020). Fast solution heat treatment of high strength aluminum alloy sheets in radiant heating furnace during hot stamping. *International Journal of Lightweight Materials and Manufacture*, *3*(1), 20–25. https://doi.org/10.1016/j.ijlmm.2019.11.004

Lu, B., Wang, L., Geng, Z., & Huang, Y. (2017). Determination of interfacial heat transfer coefficient for TC11 titanium alloy hot forging. *Heat and Mass Transfer*, *53*(10), 3049–3058. https://doi.org/10.1007/s00231-017-2032-5

Madhusudana, C. V. (2014). Thermal Contact Conductance. In *International Journal of Heat and Mass Transfer* (Vol. 12, Issue 3). Springer International Publishing. https://doi.org/10.1007/978-3-319-01276-6

Malkin, S., & Guo, C. (2007). Thermal Analysis of Grinding. *CIRP Annals - Manufacturing Technology*, *56*(2), 760–782. https://doi.org/10.1016/j.cirp.2007.10.005

McCool, J. I. (1986). Comparison of models for the contact of rough surfaces. *Wear*, *107*(1), 37–60. https://doi.org/10.1016/0043-1648(86)90045-1

McGee, G. R. (1982). *An Analytical and Experimental study of the Heat Transfer Characteristics of Cylinder-Flat Contacts*.

McGee, G. R., Schankula, M. H., & Yovanovich, M. M. (1985). Thermal resistance of cylinder-flat contacts: Theoretical analysis and experimental verification of a line-contact model. *Nuclear Engineering and Design*, *86*(3), 369–381. https://doi.org/10.1016/0029-5493(85)90302-4

McWaid, T., & Marschall, E. (1992). Thermal contact resistance across pressed metal contacts in a vacuum environment. *International Journal of Heat and Mass Transfer*, *35*(11), 2911–2920. https://doi.org/10.1016/0017-9310(92)90311-F

Merklein, M., Lechler, J., & Stoehr, T. (2009). Investigations on the thermal behavior of ultra high strength boron manganese steels within hot stamping. *International Journal of Material Forming*, *2*(SUPPL. 1), 259–262. https://doi.org/10.1007/s12289-009-0505-x

Merklein, M., Wieland, M., Lechner, M., Bruschi, S., & Ghiotti, A. (2016). Hot stamping of boron steel sheets with tailored properties: A review. *Journal of Materials Processing Technology*, *228*, 11–24. https://doi.org/10.1016/j.jmatprotec.2015.09.023

Merwin, J. E., & Johnson, K. L. (1963). An Analysis of Plastic Deformation in Rolling Contact. *Proceedings of the Institution of Mechanical Engineers*, *177*(1), 676–690. https://doi.org/10.1243/PIME_PROC_1963_177_052_02

Mikic, B. B., & Rohsenow, W. M. (1966). Thermal contact resistance. *Technical Report DSR 74542-41*, *September*. https://doi.org/10.1007/BF01487469 M4 - Citavi

Mitchell, I. (2004). *Residual Stress Reduction During Quenching of Wrought 7075 Aluminum Alloy*.

Müser, M. H., Dapp, W. B., Bugnicourt, R., Sainsot, P., Lesaffre, N., Lubrecht, T. A., Persson, B. N. J., Harris, K., Bennett, A., Schulze, K., Rohde, S., Ifju, P., Sawyer, W. G., Angelini, T., Ashtari Esfahani, H., Kadkhodaei, M., Akbarzadeh, S., Wu, J. J., Vorlaufer, G., … Greenwood, J. A. (2017). Meeting the Contact-Mechanics Challenge. *Tribology Letters*, *65*(4). https://doi.org/10.1007/s11249-017-0900-2

Nayak, P. R. (1973). Random process model of rough surfaces in plastic contact. *Wear*, *26*(3), 305–333. https://doi.org/10.1016/0043-1648(73)90185-3

Negus, K. J., Yovanovich, M., Thompson, J. C., Kim, S. J., & Cho, J. Y. (1988). Constriction resistance of circular contacts on coated surfaces - Effect of boundary conditions. *Journal of Thermophysics and Heat Transfer*, *2*(2), 158–164.

https://doi.org/10.2514/3.80

Olsen, E. L., Garimella, S. V, & Madhusudana, C. V. (2002). Modeling of constriction resistance in coated joints. *J. Thermophys. Heat Transfer*, *16*(2), 207–216. https://doi.org/10.2514/2.6686

Omer, K., Butcher, C., & Worswick, M. (2020). Characterization of heat transfer coefficient for non-isothermal elevated temperature forming of metal alloys. *International Journal of Material Forming*, *13*(2), 177–201. https://doi.org/10.1007/s12289-019-01478-3

Pereira, C. M., Ramalho, A. L., & Ambrósio, J. A. (2011). A critical overview of internal and external cylinder contact force models. *Nonlinear Dynamics*, *63*(4), 681–697. https://doi.org/10.1007/s11071-010-9830-3

Plouraboué, F., & Boehm, M. (1999). Multi-scale roughness transfer in cold metal rolling. *Tribology International*, *32*(1), 45–57. https://doi.org/10.1016/S0301-679X(99)00013-4

Poon, C. Y., & Bhushan, B. (1995). Comparison of surface roughness measurements by stylus profiler, AFM and non-contact optical profiler. *Wear*, *190*(1), 76–88. https://doi.org/10.1016/0043-1648(95)06697-7

Rohsenow, W. M., Hartnett, J. P., & Cho, Y. I. (1998). *Handbook of Heat Transfer*.

Sharp, S. (2009). *Competitive Intelligence Advantage: How to Minimize Risk, Avoid Surprises, and Grow Your Business in a Changing World (Google eBook)*. *4*, 290. http://books.google.com/books?id=bOIEkNaw67gC&pgis=1

Shigley, J. E., & Mischke, C. R. (1989). *Mechanical Engineering Design* (5th ed.). McGraw-Hill Inc., New York.

Tabor, D. (1948). A simple theory of static and dynamic hardness. *Proceedings of the Royal Society of London. Series A. Mathematical and Physical Sciences*, *192*(1029), 247–274. https://doi.org/10.1098/rspa.1948.0008

Tabor, D. (1951). *The hardness of metals*. Oxford University Press, Oxford.

Tabor, D. (1970). The hardness of solids. *Reviews of Physics in Technology*, *1*(3), 145–179. https://doi.org/10.1088/0034-6683/1/3/I01

Tondini, F., Bosetti, P., & Bruschi, S. (2011). Heat transfer in hot stamping of high-strength steel sheets. *Proceedings of the Institution of Mechanical Engineers, Part B: Journal of Engineering Manufacture*, *225*(10), 1813–1824. https://doi.org/10.1177/0954405411413987

Totten, G. E., & MacKenzie, D. S. (2003). *Handbook of Aluminum: Physical Metallurgy and Processes* (1st ed.). Marcel Dekker Inc.

Vakis, A. I., Yastrebov, V. A., Scheibert, J., Nicola, L., Dini, D., Minfray, C., Almqvist, A., Paggi, M., Lee, S., Limbert, G., Molinari, J. F., Anciaux, G., Aghababaei, R., Echeverri Restrepo, S., Papangelo, A., Cammarata, A., Nicolini, P., Putignano, C., Carbone, G., … Ciavarella, M. (2018). Modeling and simulation in tribology across scales: An overview. *Tribology International*, *125*(November 2017), 169–199. https://doi.org/10.1016/j.triboint.2018.02.005

Veziroglu, T. N., & Chandra, S. (1969). *Thermal conductance of two-dimensional*

*constrictions*. American Institute of Aeronautics and Astronautics. https://doi.org/10.2514/6.1968-761

Wang, M., Zhang, C., Xiao, H., & Li, B. (2016). Inverse evaluation of equivalent contact heat transfer coefficient in hot stamping of boron steel. *International Journal of Advanced Manufacturing Technology*, *87*(9–12), 2925–2932. https://doi.org/10.1007/s00170-016-8678-1

Wendelstorf, R., Spitzer, K. H., & Wendelstorf, J. (2008). Effect of oxide layers on spray water cooling heat transfer at high surface temperatures. *International Journal of Heat and Mass Transfer*, *51*(19–20), 4892–4901. https://doi.org/10.1016/j.ijheatmasstransfer.2008.01.033

Wilson, W. R. D. (1978). Friction and lubrication in bulk metal-forming processes. *Journal of Applied Metalworking*, *1*(1), 7–19. https://doi.org/10.1007/BF02833955

Wilson, W. R. D., Schmid, S. R., & Liu, J. (2004). Advanced simulations for hot forging: Heat transfer model for use with the finite element method. *Journal of Materials Processing Technology*, *155–156*(1–3), 1912–1917. https://doi.org/10.1016/j.jmatprotec.2004.04.399

Ying, L., Gao, T., Dai, M., & Hu, P. (2017). Investigation of interfacial heat transfer mechanism for 7075-T6 aluminum alloy in HFQ hot forming process. *Applied Thermal Engineering*, *118*, 266–282. https://doi.org/10.1016/j.applthermaleng.2017.02.107

Yovanovich, M., & Kitscha, W. (1973). Modeling the effect of air and oil upon the

thermal resistance of a sphere-flat contact. *8th Thermophysics Conference*, 293–319. https://doi.org/10.2514/6.1973-746

Yovanovich, M. M. (1981). New Contact and Gap Conductance Correlations for Conforming Rough Surfaces. In *AIAA 16th Thermophysics Conference*.

Yovanovich, M. M. (2005). Four decades of research on thermal contact, gap, and joint resistance in microelectronics. *IEEE Transactions on Components and Packaging Technologies*, *28*(2), 182–206. https://doi.org/10.1109/TCAPT.2005.848483

Yovanovich, M. M., & Coutanceau, J. (1969). Sur la détermination de la résistance thermique transversale d'un cylindre de révolution homogène isotrope avec des conditions aux limites mixtes. *CR Acad Sci Paris*, *268*, B821–B823.

Yu, C., Saha, S., Zhou, J., Shi, L., Cassell, A. M., Cruden, B. A., Ngo, Q., & Li, J. (2006). Thermal contact resistance and thermal conductivity of a carbon nanofiber. *Journal of Heat Transfer*, *128*(3), 234–239. https://doi.org/10.1115/1.2150833

Zhang, Z., Gao, P., Liu, C., & Li, X. (2015). Experimental and Simulation Study for Heat Transfer Coefficient in Hot Stamping of High-Strength Boron Steel. *Metallurgical and Materials Transactions B*, *46*(6), 2419–2422. https://doi.org/10.1007/s11663-015-0452-5

Zhao, K., Wang, B., Chang, Y., Tang, X., & Yan, J. (2015). Comparison of the methods for calculating the interfacial heat transfer coefficient in hot stamping. *Applied Thermal Engineering*, *79*(3), 17–26. https://doi.org/10.1016/j.applthermaleng.2015.01.018

Zhao, Y., Maietta, D. M., & Chang, L. (2000). An Asperity Microcontact Model Incorporating the Transition From Elastic Deformation to Fully Plastic Flow. *Journal of Tribology*, *122*(1), 86–93. https://doi.org/10.1115/1.555332

Zhao, Y., Marietta, D. M., & Chang, L. (2000). Closure to "discussion of 'an asperity microcontact model incorporating the transition from elastic deformation to fully plastic flow' " [ASME J. Tribol., 122, No. 2, p. 479 (2000)]. *Journal of Tribology*, *122*(2), 479–480. https://doi.org/10.1115/1.555389

# Appendix

---

For reference, the Matlab codes for the modified Brake-ZMC model are attached. The isothermal SCF contact model is discussed first, followed by the transient SCF and MCF contact models.

## Appendix A Isothermal SCF contact model

```
%%%    Model 2 Brake-ZMC Based Model (Isothermal)
%%%    Program for Single Cylindrical-Flat (SCF) Contact
%%%    Written By Farid Sharif
%%%    AA7075 (Mat. 1)-stainless steel (Mat. 2)
%%%    Parameter unit in mm (indentation, radius)
%%%    N (force), MPa (pressure, elastic modulus,
%%%    hardness), mW/mm/C (thermal conductivity)

%%% geometry %%%

r1=0.066983;                                    % Radius of Mat. 1 (asperities)
r2=Inf;                                         % Radius of Mat. 2 (flat surf.)
r=(1/r1+1/r2)^(-1);                             % Effective radius

L=7.854;                                        % Asperities length
h=0.000677;                                     % Asperities height

n=150;                                          % Number of asperities at a level
nT=n;                                           % Total number of asperities

An=pi*5^2;                                      % Nominal area

%%% Temperature selection

prompt = 'What is the temperature?';
T = 273+input(prompt);

%%% Mat. properties

E1=-39.082*T+82532;                                 % Elastic modulus Mat. 1
v1=0.00000003893*T^2+0.000013505*T+0.325165;        % Poisson ratio Mat. 1
H1=1213.40308218/(1+exp(-8.90055301684+0.0199861311784*T))^(1/1.85251658719);
% Hardness Mat. 1
Sy=265.25435-0.3569*T+0.00015*T^2;                  % Yield stress Mat. 1
```

```
m=2+(0.263572764932/(1+exp(-
8.6673247181+0.0183794508365*T))^(1/1.46043208275));
% Meyer hardness exp. Mat. 1
k1=(-0.00000005145*T^2+0.0001368*T+0.085224)*1000;
% Thermal conductivity Mat. 1

E2=200007.807625+11.7798100641*T-0.0871655802289*T^2;% Elastic modulus Mat. 1
v2=0.330966115702-0.000517355371901*T+0.000000826446280992*T^2;
% Poisson ratio Mat. 1
H2=Inf;                                     % Hardness Mat. 2
k2=6.31+0.0272*T-0.000007*T^2;              % Thermal conductivity Mat. 2
E=((1-v1^2)/E1+(1-v2^2)/E2)^(-1);           % Effective elastic modulus
H=(1/H1+1/H2)^(-1);                         % Effective hardness

%%% Load, half contact width, indentation depth at yield

Fy=Sy^2*pi*r*L/E/MaxStressCoefficient(v1)
by=sqrt(4*Fy*r/E/pi/L)
dzy=2*Fy/E/pi/L*(log(4*r/by)-0.5)

%%% Indentation depth and half contact width at fully plastic

dzp=245.*dzy;
bp=HalfContWidthPlasticB(r,dzp,h);

%% Main program: Calculation of contact load (F), contact area (A), and TCR
area (RcAn)

i=0;
dz=2e-6:2e-6:0.0005;

for i=1:length(dz)
if(dz(i)<=dzy)

F(:,i)=n*ForceElasticB(r,dz(i),E,L);
A(:,i)=n*2*L*HalfContWidthElasticB(r,dz(i));
RcAn(:,i)=An*nT*(n/TCRElasticB(r,dz(i),k1,k2,L))^-1;

elseif(dzy<=dz(i))&&(dz(i)<=dzp)

F(:,i)=n*ForceElastoplasticBrake(Fy,dzp,dzy,dz(i),L,by,H,bp,r,h,E,m);
A(:,i)=n*2*L*HalfContWidthEpBrake2(r,dzp,dzy,dz(i),h);
RcAn(:,i)=An*nT*(n/TCREpBrake2(r,dz(i),dzy,dzp,k1,k2,L,h))^-1;

else

F(:,i)=n*ForcePlasticBrake(dz(i),L,H,bp,r,h,m);
A(:,i)=n*2*L*HalfContWidthPlasticB(r,dz(i),h);
RcAn(:,i)=An*nT*(n/TCRPlasticB(r,dz(i),k1,k2,L,h))^-1;

end
end
```

## Appendix B Transient SCF contact model

```
%%%    Model 2 Brake-ZMC Based Model (Transient)
%%%    Program for Single Cylindrical-Flat (SCF) Contact
%%%    Written By Farid Sharif
%%%    AA7075 (Mat. 1)-stainless steel (Mat. 2)
%%%    Parameter unit in mm (indentation, radius)
%%%    N (force), MPa (pressure, elastic modulus,
%%%    hardness), mW/mm/C (thermal conductivity)

%%% geometry %%%

r1=0.066983;                                    % Radius of Mat. 1 (asperities)
r2=Inf;                                         % Radius of Mat. 2 (flat surf.)
r=(1/r1+1/r2)^(-1);                             % Effective radius

L=7.854;                                        % Asperities length
h=0.000677;                                     % Asperities height

n=150;                                          % Number of asperities at a level
nT=n;                                           % Total number of asperities

An=pi*5^2;                                      % Nominal area

dz=2e-6:2e-6:0.0005;

%%% Mean temperature at each indentation depth

for i=1:length(dz)
Tm=483.216511477-24039.6707619*dz-147912047.137*dz.^2;

%%% Mat. properties as a function of temperature

E1=-39.082*Tm+82532;                                % Elastic modulus Mat. 1
v1=0.00000003893*Tm.^2+0.000013505*Tm+0.325165;     % Poisson ratio Mat. 1
H1=1213.40308218./(1+exp(-
8.90055301684+0.0199861311784*Tm)).^(1/1.85251658719);                  %
Hardness Mat. 1
Sy=265.25435-0.3569*Tm+0.00015*Tm.^2;               % Yield stress Mat. 1
m=2+(0.263572764932./(1+exp(-
8.6673247181+0.0183794508365*Tm)).^(1/1.46043208275));
% Meyer hardness exp. Mat. 1
k1=(-0.00000005145*Tm.^2+0.0001368*Tm+0.085224)*1000;
% Thermal conductivity Mat. 1

E2=200007.807625+11.7798100641*Tm-0.0871655802289*Tm.^2;
% Elastic modulus Mat. 2
v2=0.330966115702-0.000517355371901*Tm+0.000000826446280992*Tm.^2;
% Poisson ratio Mat. 2
H2=Inf;                                         % Hardness Mat. 2
```

```
k2=6.31+0.0272*Tm-0.000007*Tm.^2;              % Thermal conductivity Mat. 2
E=((1-v1.^2)./E1+(1-v2.^2)./E2).^(-1);         % Effective elastic modulus
H=(1./H1+1./H2).^(-1);                         % Effective hardness
end

%%% Load, half contact width, indentation depth at yield

Fy=Sy.^2*pi*r*L./E./MaxStressCoefficient(v1);
by=sqrt(4*Fy.*r./E./pi/L);
dzy=2*Fy./E./pi/L.*(log(4*r./by)-0.5);

%%% Indentation depth and half contact width at fully plastic

dzp=245*dzy;
bp=HalfContWidthPlasticB(r,dzp,h);

%% Main program: Calculation of contact load (F), contact area (A), and TCR
area (RcAn)

for ii=1:length(dz)
if dz(ii)<=dzy(ii)

F(ii)=n*ForceElasticB(r,dz(ii),E(ii),L);
A(ii)=n*2*L*HalfContWidthElasticB(r,dz(ii));
RcAn(ii)=An*nT*(n/TCRElasticB(r,dz(ii),k1(ii),k2(ii),L))^-1;

elseif(dzy(ii)<=dz(ii))&&(dz(ii)<=dzp(ii))

F(ii)=n*ForceElastoplasticBrake(Fy(ii),dzp(ii),dzy(ii),dz(ii),L,by(ii),H(ii),b
p(ii),r,h,E(ii),m(ii));
A(ii)=n*2*L*HalfContWidthEpBrake2(r,dzp(ii),dzy(ii),dz(ii),h);
RcAn(ii)=An*nT*(n/TCREpBrake2(r,dz(ii),dzy(ii),dzp(ii),k1(ii),k2(ii),L,h))^-1;

else

F(ii)=n*ForcePlasticBrake(dz(ii),L,H(ii),bp(ii),r,h,m(ii));
A(ii)=n*2*L*HalfContWidthPlasticB(r,dz(ii),h);
RcAn(ii)=An*nT*(n/TCRPlasticB(r,dz(ii),k1(ii),k2(ii),L,h))^-1;

end
end
```

## Appendix C Transient MCF contact model

```
%%%    Model 2 Brake-ZMC Based Model (Transient)
%%%    Program for Multi Cylindrical-Flat (MCF) Contact
%%%    Written By Farid Sharif
%%%    AA7075 (Mat. 1)-stainless steel (Mat. 2)
%%%    Parameter unit in mm (indentation, radius)
%%%    N (force), MPa (pressure, elastic modulus,
%%%    hardness), mW/mm/C (thermal conductivity)

%%% geometry %%%

r1A=0.08;                                       % Radius of Mat. 1 (level 1)
r1B=0.08;                                       % Radius of Mat. 1 (level 2)
r1C=0.08;                                       % Radius of Mat. 1 (level 3)
r2=Inf;                                         % Radius of Mat. 2 (flat surf.)

rA=(1/r1A+1/r2)^(-1);                           % Effective radius (level 1)
rB=(1/r1B+1/r2)^(-1);                           % Effective radius (level 2)
rC=(1/r1C+1/r2)^(-1);                           % Effective radius (level 3)

L=7.854;                                        % Asperities length
hA=0.000677;                                    % Asperities height (level 1)
hB=0.0006;                                      % Asperities height (level 2)
hC=0.0004;                                      % Asperities height (level 3)

nA=100;                                         % Number of asperities (level 1)
nB=0;                                           % Number of asperities (level 2)
nC=50;                                          % Number of asperities (level 3)
nT=nA+nB+nC;                                    % Total number of asperities

d1=hA-hB;                          % Indentation depth to reach asperity level 2
d2=hA-hC;                          % Indentation depth to reach asperity level 3

An=pi*5^2;                                      % Nominal area

dz=2e-6:2e-6:0.0005;

%%% Mean temperature at each indentation depth

for i=1:length(dz)
Tm=483.216511477-24039.6707619*dz-147912047.137*dz.^2;

%%% Mat. properties as a function of temperature

E1=-39.082*Tm+82532;                                % Elastic modulus Mat. 1
v1=0.00000003893*Tm.^2+0.000013505*Tm+0.325165;     % Poisson ratio Mat. 1
H1=1213.40308218./(1+exp(-
8.90055301684+0.0199861311784*Tm)).^(1/1.85251658719);                 %
Hardness Mat. 1
```

```
Sy=265.25435-0.3569*Tm+0.00015*Tm.^2;               % Yield stress Mat. 1
m=2+(0.263572764932./(1+exp(-
8.6673247181+0.0183794508365*Tm)).^(1/1.46043208275));
% Meyer hardness exp. Mat. 1
k1=(-0.00000005145*Tm.^2+0.0001368*Tm+0.085224)*1000;
% Thermal conductivity Mat. 1
E2=200007.807625+11.7798100641*Tm-0.0871655802289*Tm.^2;
% Elastic modulus Mat. 2
v2=0.330966115702-0.000517355371901*Tm+0.000000826446280992*Tm.^2;
% Poisson ratio Mat. 2
H2=Inf;                                         % Hardness Mat. 2
k2=6.31+0.0272*Tm-0.000007*Tm.^2;               % Thermal conductivity Mat. 2

E=((1-v1.^2)./E1+(1-v2.^2)./E2).^(-1);          % Effective elastic modulus
H=(1./H1+1./H2).^(-1);                          % Effective hardness
end

%%% Load, half contact width, indentation depth at yield (level 1)

FyA=Sy.^2*pi*rA*L./E./MaxStressCoefficient(v1);
byA=sqrt(4*FyA.*rA./E./pi/L);
dzyA=2*FyA./E./pi/L.*(log(4*rA./byA)-0.5);

%%% Load, half contact width, indentation depth at yield (level 2)

FyB=Sy.^2*pi*rB*L./E./MaxStressCoefficient(v1);
byB=sqrt(4*FyB.*rB./E./pi/L);
dzyB=2*FyB./E./pi/L.*(log(4*rB./byB)-0.5);

%%% Load, half contact width, indentation depth at yield (level 3)

FyC=Sy.^2*pi*rC*L./E./MaxStressCoefficient(v1);
byC=sqrt(4*FyC.*rC./E./pi/L);
dzyC=2*FyC./E./pi/L.*(log(4*rC./byC)-0.5);

%%% Indentation depth and half contact width at fully plastic (level 1)

dzpA=245.*dzyA
bpA=HalfContWidthPlasticB(rA,dzpA,hA)

%%% Indentation depth and half contact width at fully plastic (level 2)

dzpB=245.*dzyB
bpB=HalfContWidthPlasticB(rB,dzpB,hB)

%%% Indentation depth and half contact width at fully plastic (level 3)

dzpC=245.*dzyC
bpC=HalfContWidthPlasticB(rC,dzpC,hC)
```

```
%% Main program: Calculation of contact load (F), contact area (A), and TCR
area (RcAn)

for ii=1:length(dz)

if dz(ii)<d1

F(ii)=nA*ForcePlasticBrake(dz(ii),L,H(ii),bpA(ii),rA,hA,m(ii));
A(ii)=nA*2*L*HalfContWidthPlasticB(rA,dz(ii),hA);
RcAn(ii)=An*nT*(nA/TCRPlasticB(rA,dz(ii),k1(ii),k2(ii),L,hA))^-1;

elseif  dz(ii)>=d1 & dz(ii)<d2

F(ii)=nA*ForcePlasticBrake(dz(ii),L,H(ii),bpA(ii),rA,hA,m(ii))+nB*ForcePlastic
Brake((dz(ii)-d1),L,H(ii),bpB(ii),rB,hB,m(ii));
A(ii)=2*L*(nA*HalfContWidthPlasticB(rA,dz(ii),hA)+nB*HalfContWidthPlasticB(rB,
(dz(ii)-d1),hB));
RcAn(ii)=An*nT*(nA/TCRPlasticB(rA,dz(ii),k1(ii),k2(ii),L,hA)+nB/TCRPlasticB(rB
,(dz(ii)-d1),k1(ii),k2(ii),L,hB))^-1;

else

F(ii)=nA*ForcePlasticBrake(dz(ii),L,H(ii),bpA(ii),rA,hA,m(ii))+nB*ForcePlastic
Brake((dz(ii)-d1),L,H(ii),bpB(ii),rB,hB,m(ii))+nC*ForcePlasticBrake((dz(ii)-
d2),L,H(ii),bpC(ii),rC,hC,m(ii));
A(ii)=2*L*(nA*HalfContWidthPlasticB(rA,dz(ii),hA)+nB*HalfContWidthPlasticB(rB,
(dz(ii)-d1),hB)+nC*HalfContWidthPlasticB(rC,(dz(ii)-d2),hC));
RcAn(ii)=An*nT*(nA/TCRPlasticB(rA,dz(ii),k1(ii),k2(ii),L,hA)+nB/TCRPlasticB(rB
,(dz(ii)-d1),k1(ii),k2(ii),L,hB)+nC/TCRPlasticB(rC,(dz(ii)-
d2),k1(ii),k2(ii),L,hC))^-1;

end
end
```

```
%%% Function of maximum stress coefficient

function [fmax]=MaxStressCoefficient(v)

j=0;
u=0:0.001:1;
for j=1:length(u)

fm(j,:)=(2.*u(j)-
(2.*u(j).^2)./(u(j).^2+1).^(1/2)).^2./2+((2.*u(j).^2+1)./(u(j).^2+1).^(1/2)-
2.*u(j)+2.*v.*(u(j)-
(u(j).^2+1).^(1/2))).^2./2+(1./(u(j).^2+1).^(1/2)+2.*v.*(u(j)-
(u(j).^2+1).^(1/2))).^2./2;

end

[val,idx] = max(fm);
fmax=max(fm);

%%% Function of half contact width during elastic deformation

function [bElB]=HalfContWidthElasticB(r,dz)

b=0:1e-6:0.1;

[dzE,B]=meshgrid(dz,b);

f1E=2*dzE.*r./B.^2;
f2E=-0.5+log(4*r./B);
f3E=abs(f1E-f2E);

[g1E,g2E]=min(f3E);

bElB=B(g2E);

%%% Function of half contact width during elastoplastic deformation

function [bElp]=HalfContWidthEpBrake2(r,dzp,dzy,dz,h)

bElp=HalfContWidthElasticB(r,dz)+(tanh((dz-dzy)./(dzp-
dzy).*pi))*((HalfContWidthPlasticB(r,dz,h))-HalfContWidthElasticB(r,dz));

%%% Function of half contact width during plastic deformation

function [bPlB]=HalfContWidthPlasticB(Rinit,dz,h)

z=Rinit-h;
r=Rinit:1e-6:0.2;

[dzP,R]=meshgrid(dz,r);
```

```
f1P=R.^2.*acos(z./R)-Rinit^2*acos(z/Rinit)-z*sqrt(R.^2-z^2)+z*sqrt(Rinit^2-
z^2);
f2P=R.^2.*acos((Rinit-dzP)./R)-(Rinit-dzP).*sqrt(R.^2-(Rinit-dzP).^2);
f3P=abs(f1P-f2P);

[g1P,g2P]=min(f3P);

bPlB=sqrt((R(g2P)).^2-(Rinit-dz).^2);

%%% Function of load during elastic deformation

function [FElB]=ForceElasticB(r,dz,E,L)

FElB=(HalfContWidthElasticB(r,dz)).^2.*pi*E*L/4/r;

%%% Function of load during elastoplastic deformation

function [FElp]=ForceElastoplasticBrake(Fy,dzp,dzy,dz,L,by,H,bp,r,h,E,m)

FElp=(1-tanh((dz-dzy)./(dzp-
dzy).*pi)).*(HalfContWidthElasticB(r,dz)).^2.*pi*E*L/4/r+(tanh((dz-dzy)./(dzp-
dzy).*pi))*2*L*H/bp^(m-2).*(HalfContWidthPlasticB(r,dz,h)).^(m-1);

%%% Function of load during plastic deformation

function [FPl]=ForcePlasticBrake(dz,L,H,bp,r,h,m)

FPl=2*L*H/bp^(m-2).*(HalfContWidthPlasticB(r,dz,h)).^(m-1);

%%% Function of TCR area during elastic deformation

function [RcElB]=TCRElasticB(r,dz,k1,k2,L)

RcElB=1e3/pi/L./k2*log(2*r/pi/(HalfContWidthElasticB(r,dz)))+1e3/pi/L./k1*log(
4*r/(HalfContWidthElasticB(r,dz)))-1e3/2/L./k1;

%%% Function of TCR area during elastoplastic deformation

function [RcEpl]=TCREpBrake2(r,dz,dzy,dzp,k1,k2,L,h)

RcEpl=1e3/pi/L./k2*log(2*r/pi/(HalfContWidthEpBrake2(r,dzp,dzy,dz,h)))+1e3/pi/
L./k1*log(4*r/(HalfContWidthEpBrake2(r,dzp,dzy,dz,h)))-1e3/2/L./k1;

%%% Function of TCR area during plastic deformation

function [RcPlB]=TCRPlasticB(r,dz,k1,k2,L,h)

RcPlB=1e3/pi/L./k2*log(2*r/pi/(HalfContWidthPlasticB(r,dz,h)))+1e3/pi/L./k1*lo
g(4*r/(HalfContWidthPlasticB(r,dz,h)))-1e3/2/L./k1;
```